INFORMATION TO USERS

This manuscript has been reproduced from the microfilm master. UMI films the text directly from the original or copy submitted. Thus, some thesis and dissertation copies are in typewriter face, while others may be from any type of computer printer.

The quality of this reproduction is dependent upon the quality of the copy submitted. Broken or indistinct print, colored or poor quality illustrations and photographs, print bleedthrough, substandard margins, and improper alignment can adversely affect reproduction.

In the unlikely event that the author did not send UMI a complete manuscript and there are missing pages, these will be noted. Also, if unauthorized copyright material had to be removed, a note will indicate the deletion.

Oversize materials (e.g., maps, drawings, charts) are reproduced by sectioning the original, beginning at the upper left-hand corner and continuing from left to right in equal sections with small overlaps.

Photographs included in the original manuscript have been reproduced xerographically in this copy. Higher quality 6" x 9" black and white photographic prints are available for any photographs or illustrations appearing in this copy for an additional charge. Contact UMI directly to order.

ProQuest Information and Learning
300 North Zeeb Road, Ann Arbor, MI 48106-1346 USA
800-521-0600

SILICON MICROMACHINED WAVEGUIDE TRANSITIONS AND THREE-DIMENSIONAL LITHOGRAPHY FOR HIGH FREQUENCY PACKAGING

By

James Paul Becker

A dissertation submitted in partial fulfillment
of the requirements for the degree of
Doctor of Philosophy
(Electrical Engineering)
in The University of Michigan
2001

Doctoral Committee:

Professor Linda P.B. Katehi, Chair
Dr. Jack R. East, Research Scientist
Assistant Professor Clark T.C. Nguyen
Professor John Halloran

UMI Number: 3029293

UMI Microform 3029293

Bell & Howell Information and Learning Company
300 North Zeeb Road
P.O. Box 1346
Ann Arbor, MI 48106-1346

To my family...

ACKNOWLEDGEMENTS

I would like first and foremost to thank my advisor, Professor Linda Katehi, for her guidance, support, and for her example of hard work and professionalism. Her ability to remain cordial in the midst of all she does remains somewhat of a mystery to me. My decision to come to Michigan was based in significant measure on her record and my initial meeting with her -- I feel fortunate to have had the opportunity to work with her.

I would also like to thank Dr. Jack East for sharing his expertise in THz systems and for providing key insights into several of the problems that I encountered during my research. I have greatly profited from my interaction with him. I also thank Professor Clark Nguyen for his time in serving on my committee, his suggestions for alternate means of fabricating silicon waveguides, and for providing students with an excellent course in analog ICs for communications. I also sincerely thank Dr. John Halloran of the Materials Science Department for joining my committee on such late notice and for giving important feedback on how to improve this dissertation.

Perhaps the most enriching element of a graduate education is the interaction one has with fellow students. While I could no doubt thank each and every colleague I have met at Michigan, I wish to single out three who have made my experience here immeasurably better. Dr. Andrew Brown was kind enough to train me in many of the techniques and protocols used in the work for this dissertation. Andy is one who truly understands that,

knowledge has an interesting property – when you give it away, you don't lose it. I thank Ms. Hua Xie who has been a good friend, a great sounding board for ideas, and a wonderful ambassador for her homeland. Finally, I have enjoyed working with Mr. Yongshik Lee over the course of the last couple of years and wish to acknowledge his contribution to this work in the assembling and testing the transition of Figure 7.18.

I would also like to acknowledge the generous financial support for both the research presented in this dissertation and for my education here at Michigan. Specifically I would like to thank the Office of Naval Research (grant number N00014-98-1-0628) and the Defense Advanced Research Projects Agency (Solid-State THz Sources grant number N00014-99-1-0915).

Finally, I am most thankful for my family and for their boundless love and support.

PREFACE

This thesis presents the measured performance of an integrated waveguide based on micromachined (001) silicon, and a transition coupling the finite ground coplanar transmission line to such an integrated waveguide at W-band frequencies. Through simple modification of this novel transition structure, extension to submillimeter wave frequencies is reasonable. Such waveguides and transitions may find application in submillimeter wave systems including a novel power combining module proposed herein. As proposed, the module incorporates integrated antennas that are compatible with the current fabrication process, a process that utilizes both wet anisotropic etching as well as deep reactive ion etching of silicon.

Three-dimensional lithography, one of the remaining obstacles to fully exploiting the potential of micromachined structures, is also addressed in this thesis. The ability to simultaneously pattern features on the various facets of micromachined silicon is demonstrated and a novel high frequency electronic packaging architecture using micromachined silicon as a substrate material and electrophoretic deposition of photoresist for patterning is presented. The average loss of a finite ground coplanar transmission line transition into a 110 μm deep micromachined cavity is shown to be less than 0.08 dB in the 2-40 GHz frequency range. This multilevel transition may be employed as part of a package used to provide environmental protection for microelectromechanical switches without severely compromising their high-frequency performance.

TABLE OF CONTENTS

LIST OF FIGURES

LIST OF APPENDICES

CHAPTER 1

INTRODUCTION

1.1: Motivation

In recent years the practice of micromachining has been the focus of significant research activity and has accordingly been greatly refined. This fervor of activity stems in large part from the broad acceptance of microelectromechanical systems and their application in disparate arenas. Inertial sensors for the automotive industry, miniature optical microscopes for medical diagnosis, and tiny integrated filters for communications systems are but a few examples of the areas in which micromachining is of interest. In this dissertation silicon micromachining is explored for application in the areas of millimeter/submillimeter systems and high-frequency packaging.

1.1.1: Millimeter Wave and Submillimeter Wave Systems

The simple relationships between frequency and wavelength and between data rate and bandwidth have compelled scientists and engineers to constantly push devices and systems to higher frequencies. The fact that as the frequency of a signal increases, its corresponding wavelength decreases promises smaller systems and greater imaging resolution at these higher frequencies. Larger antenna gain for a given aperture size is also achieved as operating frequency increases. At higher frequencies, a given fractional bandwidth will result in more channels for communication or data transfer purposes.

Viewed in another manner, a greater bandwidth will allow a greater data rate. For these reasons the microwave and millimeter wave portions (30 GHz-300 GHz) of the electromagnetic spectrum are of great interest to the military and commercial communities. In fact, interest and activity have stretched into the Terahertz (THz) spectrum, loosely defined as the frequency range from 100 GHz to 10 THz [1]. The advantages accrued by operating at higher frequencies are not without cost however.

Generally speaking, the attenuation of a given microwave signal traveling through the Earth's atmosphere increases with frequency. Just as there are windows of atmospheric transparency for infrared radiation however, microwave/millimeter energy also experiences reduced absorption in various narrow frequency bands, most notably around 94 GHz and 220 GHz. On the other hand various remote sensing applications require the absorption and emission of microwave to submillimeter-wave energy for operation. For example, identification of the physical and chemical properties of star formation is possible by means of recognizing the molecular transitions of interstellar clouds [2]. So too, various point-to-point communication systems have been proposed that take advantage of increased absorption at higher millimeter-wave frequencies. Such systems would seek the advantage of increased data rates at these higher frequencies, with the combination of highly directional antennas and increased absorption making secure transmission of data possible.

Perhaps the most formidable obstacle to be overcome in the development of THz systems is the lack of compact and economical power sources at these frequencies. Microwave power generated at frequencies above 100 GHz is typically supplied by

vacuum tube-type sources such as klystrons and gyrotrons. For example, gyrotrons are capable of producing 1 kW of power at 300 GHz [3].

Extensive research has gone into the development of both two and three terminal solid-state devices to replace microwave tube sources. Such solid-state sources have the advantage of being compact, rugged, compatible with microwave integrated circuits and of relatively low cost [4]. Recently, three-terminal solid-state oscillator circuits have been demonstrated at frequencies stretching beyond 100 GHz. While promising, only rather modest power levels have been achieved with this technology. For instance, an InP-Based HEMT oscillator was reported to deliver approximately 0.2 mW at 130.7 GHz [5]. State-of-the-art two terminal GaAs tunnel injection transit-time (TUNNETT) diodes and InP Gunn diodes offer greater power than that currently reported for three terminal devices. RF powers of greater than 130 mW, 80 mW and 1 mW have been reported with InP Gunn devices at 132 GHz, 152 GHz and 315 GHz respectively. GaAs TUNNETTS have exhibited the somewhat more modest results of 100 mW at 107 GHz and 10 mW at 202 GHz [6], but are still superior to three terminal devices in this regard. To achieve more substantial power levels, clearly the output of many devices must be combined.

Waveguide-based quasi-optical power combining is a potential means to successfully produce the required sources for THz systems. In one proposed system, the outputs of many individual solid-state based planar circuits are to be coupled to low-loss hollow waveguides with further power combining achieved in free-space [7]. Conventional machining of hollow metal waveguides becomes costly at these frequencies as the dimensions of the waveguide must follow the shrinking wavelength. Silicon "micromachining" is proving a strong candidate for development of low-cost waveguides

at these frequencies, thus making such power combining systems viable. A successful silicon-based power combining module might consist of planar circuitry, integrated waveguides, and transitions between the two.

In this dissertation, development of a suitable transition from a planar transmission line to a silicon micromachined waveguide is explored. Such a structure is made possible through the combination of two bulk micromachining techniques, wet anisotropic etching and deep reactive ion etching. The design, fabrication and testing of this novel structure will be reviewed and potential power combining architectures that take advantage of this transition will be introduced.

1.1.2: Silicon-Based Packaging of Microwave Circuitry

Electrical and mechanical packaging often becomes a limiting factor in today's advanced circuitry, as the interfacing of various subsystems may introduce parasitics that severely degrade circuit performance. Issues such as cross-talk minimization, conservation of signal integrity, and proper thermal management must be successfully addressed in the development of mechanically robust packages.

Research at The University of Michigan has addressed the question of whether silicon can be used as an electronic packaging material for high-frequency circuits [8]. Measurement results have demonstrated that silicon micromachined structures may be used to reduce coupling levels between neighboring transmission lines to better than -40 dB up to 40 GHz. In this same study, a silicon micromachined Ka-Band discrete component package demonstrated superior electrical performance than its alumina counterpart. In other research at Michigan, the development of 3D silicon

micromachined W-band circuitry has been investigated [9]. One result from this work is the demonstration of a three-via intrawafer interconnect.

In the work presented in this thesis, a novel photolithographic technique is explored that holds promise for furthering the development of 3D packaging concepts in silicon. The possibilities of this technique are demonstrated through simultaneous patterning of a finite-ground coplanar waveguide transmission line on the sidewalls and bottom of a micromachined cavity. The resulting transition exhibits excellent performance up to at least 40 GHz. With the addition of the three-via transition demonstrated in [9], a novel means to package RF microelectromechanical (MEM) switches is possible. Finally, the design and simulation of a novel three-via vertical transition that could likewise be utilized in the packaging of RF-MEM switches is presented along with a potential fabrication protocol for producing such a package.

1.2: Dissertation Overview

As stated above, this thesis explores the development of a transition from a finite-ground coplanar transmission line to a silicon micromachined waveguide for application in the THz spectrum. The use of micromachining and novel photolithographic processing are also investigated to further the case for silicon-based microwave and millimeter wave circuitry.

Chapter 2 provides a brief overview of the THz spectrum, discussing the requirements of systems operating at these frequencies and the efforts underway to develop such systems. A variety of investigations to develop THz micromachined waveguides are referenced.

Chapter 3 serves as a review of the experimental techniques used in this study. The bulk micromachining practices of wet anisotropic etching and deep reactive ion etching used extensively herein are discussed. Experimental micromachining results presented in the chapter address achievable dimensional accuracy, uniformity and surface roughness. The simulation tools used in the design portion of this dissertation are reviewed as well as the testing protocol.

Chapter 4 is devoted to the problem of photolithographic patterning of micromachined surfaces. The failure of conventional wafer spinning for resist application on such structures is documented and the development of a suitable fabrication procedure utilizing electrophoretic deposition of photoresist is detailed.

Chapter 5 examines the use of electrophoretic deposition for 3D packaging of microwave circuitry through the example of a simple multilevel transmission line. A second potential solution to 3D packaging using deep reactive ion etching is also suggested.

Chapter 6 explores the properties of micromachined waveguides. Along with the standard rectangular version, two waveguides that evolve naturally from the crystal planes of anisotropically wet etched (001) silicon are considered. Both simulated and measured results of a silicon "diamond waveguide" are given.

The excitation of a hollow waveguide using a finite-ground coplanar transmission line is discussed in chapter 7. Elementary analytical analysis helps to provide a detailed look at the theory behind magnetic coupling to a rectangular waveguide. While a magnetic loop coupling transition to a micromachined cavity has been fabricated and tested, development of a similar transition to a full-fledged waveguide did not prove successful.

Reasons for this difficulty are discussed. A suitable electric field coupling structure was developed and its performance is documented in chapter 7.

Chapter 8 summarizes the accomplishments detailed in this dissertation, illustrates other potential applications of electrodeposition of photoresist, and introduces a potential power combining architecture that could evolve from the waveguides of chapter 6 and the transition structure developed in chapter 7.

CHAPTER 2

BACKGROUND

2.1: Generation, Propagation and Detection of THz Waves

The submillimeter range (beginning at 300 GHz or $\lambda = 1$mm) is perhaps the most awkward portion of the electromagnetic spectrum from a system development perspective. The difficulty arises in part from the size of the corresponding wavelength as well as the characteristics of wave propagation at these frequencies. A schematic diagram depicting the divisions of the portion of the EM spectrum surrounding the submillimeter range is given in Figure 2.1. The submillimeter region and the so-called "THz spectrum" overlap in great measure and will henceforth be referred to interchangeably.

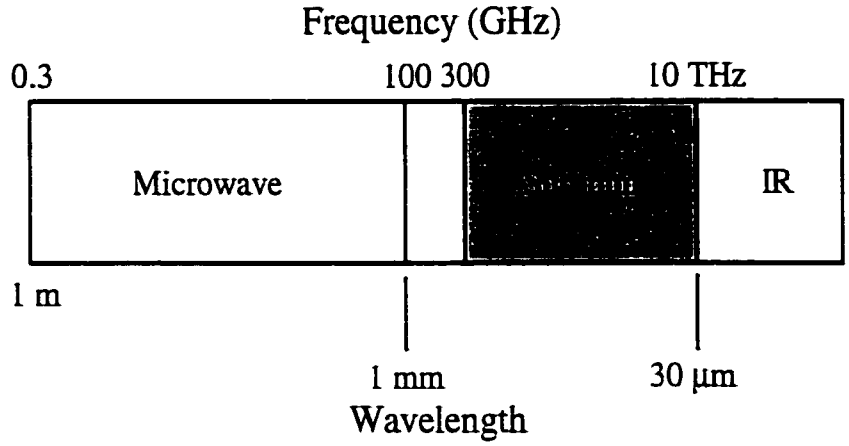

Figure 2.1: Depiction of the frequency ranges surrounding the sub-mm region.

Below the THz spectrum lays the microwave region. Wave propagation in this region is typically accomplished via a single mode with the cross-section of guiding structures such as waveguides on the order of the size of the wavelength [10], or indeed smaller than the wavelength in the case of planar lines.

At the opposite end of the submillimeter range is the optical regime (infrared and beyond). In this range, wave propagation is typically established via multimode beams of size considerably larger than the corresponding wavelength, with propagation in free space directed by lens. Of course examples do exist of single mode propagation in such structures as single-mode fibers and dielectric strips.

Sources of microwave radiation include electron tubes (e.g. klystrons and gyrotrons) for high-power generation, and solid-state oscillators (e.g. Gunn diodes and three-terminal oscillators) for lower power applications. Lasers are the sources of choice for operation in the optical regime. Detection of microwaves is often achieved through diode-based circuitry, and optical radiation measured via quantum detectors.

Thus, generation, propagation and detection of electromagnetic energy in the regions on either side of the submillimeter wave range are well characterized, but handled in quite distinct manners. *From which direction should we approach the submillimeter wave range?* We can attempt to extend the technologies of the microwave region to the higher frequencies of the submillimeter range, or we can seek to bring the well-established optical techniques down several decades in frequency.

2.2: Toward Submillimeter Wave Systems

2.2.1: Submillimeter Transmission Lines

Given the choice of available technologies, which guided wave transmission structure is best suited for extension from microwave or optical to submillimeter wave frequencies? The specifics of a given application will no doubt dictate the appropriate choice with features such as attenuation, ease of manufacture and compatibility with active circuitry key items of consideration.

In the microwave region, hollow metal waveguides are typically the lowest loss transmission line. For instance, the attenuation of a commercially available rectangular waveguide is of the order of 0.12 dB/cm or 0.024 dB/λg at 100 GHz [11]. This compares favorably with both finite ground coplanar (FGC) and micromachined finite ground coplanar (MFGC) transmission lines. For instance, the loss of a 57 Ω FGC line fabricated on high resistivity silicon was found to be 2.2 dB/cm or 0.302 dB/λg and that for a 66 Ω MFGC to be 0.8 dB/cm or 0.126 dB/λg at 94 GHz [12].

Perhaps the best performance achievable in a planar, metal conductor-based transmission line is that from a microshield line [15] in which the metal lines are supported in air by only a very thin (~ 1.5 μm) membrane rather than a thick substrate. In such a structure, dielectric loss is nearly eliminated. The loss reported in a finite ground coplanar microshield line has been as low as 0.3 dB/cm (~0.25 dB/λg) at 35 GHz [13], [14]. Assuming only conductor loss, this should translate into an attenuation at 100 GHz of approximately 0.5 dB/cm or 0.14 dB/λg. (It is interesting to note that when comparing loss performance in terms of dB/λg, the advantages of microshield over FGC and MFGC

transmission lines may in fact nearly disappear. (See p. 16 of [13] and p. 40 of [9] for further comment.)

Efforts have been made to extend microwave transmission lines to the submillimeter wave range. For example, electro-optic techniques have been used to measure the loss of several planar transmission lines up to 1 THz. The best performance reported in this investigation was exhibited by membrane supported coplanar strips (CPS). At 500 GHz the loss of the membrane-supported CPS (250 Ω) was found to be on the order of 0.05 Np/mm, which is equal to 5.2 dB/cm (0.3 dB/λg) [15].

In the optical regime, guided signal propagation in various communication systems may be accomplished with either multimode or single mode fibers. Loss is typically extremely small compared with values achieved with appropriate transmission lines in the microwave region. For example the attenuation coefficient of a single mode fiber for use at 1550 nm is typically on the order of 0.25 dB/km [16]. Following the wave propagation concept of optical waveguides, dielectric guides of various forms including image guides, H-guides and groove guides have been explored for use in the microwave region [17], some of which could be utilized at submillimeter wave frequencies. For instance, the predicted performance of a dielectric ridge guide designed for operation at 490 GHz and consisting of a grounded GaAs substrate with additional layers of AlAs and GaAs has been investigated by Katehi [18]. In this work, the predicted loss of a microstrip, the ridge guide just described, and a hollow rectangular waveguide are compared in the 400-600 GHz range. In this range the ridge guide exhibits superior loss performance when compared with microstrip but fails to achieve that of the rectangular guide. At 500 GHz for example, the microstrip is expected to exhibit an attenuation of

approximately 14.7 dB/cm (0.29 dB/λg), the ridge guide 4 dB/cm (0.19 dB/λg) and the rectangular waveguide 0.5 dB/cm (0.03 dB/λg). From the above discussion, it does appear that the rectangular waveguide may indeed offer the possibility of lowest loss performance.

2.2.2: Submillimeter Wave Sources

The development of low-cost, compact sources at THz frequencies is perhaps the most daunting obstacle to fully exploiting the submillimeter wave region. In the low frequency portion of the microwave region, solid-state circuitry (monolithic microwave integrated circuits or MMICs) is predominant and capable of providing many watts of power. For instance, an output power of 40 W at 2.2 GHz has been reported from a GaAs FET (field effect transistor) chip [19].

As mentioned in section 1.1.1, while solid-state sources have been demonstrated at frequencies greater than 100 GHz, power levels remain modest. Increased power may be achieved with solid-state sources using various power combining schemes at the device and/or circuit level as well as through spatial combining techniques [20]-[23]. Microwave tube sources such as klystrons and gyrotrons have been the workhorse for high-power applications with their ability to generate kilowatts of continuous wave power at frequencies extending beyond 100 GHz. Unfortunately such tube sources are bulky, require large supply voltages and are not readily mated with microwave integrated circuits.

Lasers are standard sources of radiation at infrared frequencies and beyond. Efforts have been made to produce lasing in the submillimeter wave range by a variety of techniques. For example, free electron lasers have demonstrated coherent radiation from

microwaves to the ultraviolet [24] and optically pumped lasers (usually through the use of a 10 μm CO_2 laser) are capable of producing significant radiation throughout the submillimeter wave range [25]. Unfortunately such laser-based sources are quite large [24] and thus are not desirable in space-based systems in which payload weight and volume are of critical concern.

2.2.3: Submillimeter Wave Detectors

Detection of submillimeter waves may be accomplished either through direct detection using a broadband bolometric receiver or using heterodyne techniques. Heterodyne receivers, such as those based on either a whisker-contacted schottky diode or a superconductor-insulator-superconductor (SIS) tunnel junction, are preferred for observation of spectral lines [26].

Due to reliability and efficiency of signal coupling, waveguide technology has long been the favored means of implementing the mixer portion of a receiver, at least to frequencies of about 600 GHz. In systems operating above 700 GHz, receivers are often constructed using a whisker-contact Schottky diode mounted in a corner-cube antenna [26]. Much effort has been directed at developing planar solutions in the submillimeter wave range. These efforts are spurred by the promise [27] that, "*it should be possible to build planar receivers with performance comparable to the best waveguide-based systems if efficient planar antennas and matching networks are developed.*" Here again it seems that waveguide-based systems provide the benchmark for performance.

2.3: Micromachined Waveguides and Circuits

"*The most successful millimeter- and submillimeter-wave components, such as oscillators, multipliers and mixers, generally use traditional metal blocks which are fabricated by standard machining techniques*" [28]. As we reach the submillimeter wave range however, fabrication of hollow waveguides becomes particularly difficult and costly as conventional machining of precision features must follow the shrinking wavelength. For instance a WR-3 waveguide (220-325 GHz) has cross-sectional dimensions of 0.034 inches by 0.017 inches (864 μm by 432 μm). *Custom Microwave* of Longmont Colorado is able to manufacture such waveguides to a tolerance of ± 0.0002 inches (5 μm) with a corner radius of 0.0015 inches (38 μm) [29]. At the time of this writing, a one-inch straight section of WR-3 fabricated to this tight tolerance costs more than $800.

Because of the difficulty and corresponding cost in manufacturing conventional rectangular waveguides, a variety of investigations have been undertaken to "micromachine" such waveguides. One of the first such investigations into developing micromachined waveguides was by McGrath et al. [11]. In this effort wet anisotropic etching of (110) silicon was utilized to effect rectangular guides. A micromachined version of the WR-10 (75-100 GHz) was fabricated and then tested using conventionally machined brass mounting blocks. The measured attenuation of 0.04 dB/λg is close to the 0.024 dB/λg they measured for a commercially available WR-10 section. They attributed the variation to "*differences in the quality of the gold plated surface.*" This technique has also been used to fabricate WR-4 waveguides that exhibit an average loss of approximately 0.8 dB/inch in the 195-255 GHz range [30]. From Figure 9a of [30], it

appears that the measured loss is roughly 0.9 dB/inch, corresponding to an attenuation of approximately 0.06 dB/λg.

Other investigations [31], [32] have produced reduced height waveguides at 75-110 GHz using a "snap together" technology based on EPON SU-8 (a negative photoresist). A rather large loss of ~ 0.5 dB/λg at 110 GHz was reported. The authors do anticipate that through modifications in the constituent pieces and their connection, attenuation in waveguides operating at 200 GHz and above should be greatly reduced. In other work [33], [34], x-ray microfabrication has been used to fabricate a 2.5 THz waveguide package though no measured results are given.

An attempt has been made to integrate a reduced-height waveguide using polyimide and an aluminum metalization on semi-insulating GaAs substrates [35]. The idea is to allow for the monolithic implementation of GaAs-based active circuitry with a waveguide technology. Unfortunately the initial measured performance of the waveguide was quite poor exhibiting an attenuation -40 dB/λg at 110 GHz.

In this dissertation, the performance of a diamond-shaped waveguide integrated in silicon is considered as well as a suitable transition from a planar transmission line to a micromachined waveguide. Such a transition allows integration of active circuitry into a fully-packaged module. The fabrication and testing techniques used to investigate these structures are described in the following chapter.

CHAPTER 3

EXPERIMENTAL TECHNIQUES

3.1: Silicon Micromachining

Silicon remains the substrate material of choice for integrated circuits (IC's). This is due in large measure to the existence of a high-quality silicon-based oxide, silicon's superior mechanical properties, good electrical properties, and a mature processing technology that allows low-cost circuit development. An additional asset of silicon, though not utilized in typical IC fabrication, is its ability to be micromachined, that is, to be sculpted on a very fine scale. While a variety of silicon micromachining techniques are available, the bulk micromachining techniques of wet anisotropic etching and deep reactive ion etching are used in the work presented in this thesis and will thus be reviewed below.

3.1.1: Wet Anisotropic Etching

Generally speaking, an etching process may be termed either isotropic or anisotropic depending on the resulting form of the etched void. An isotropic etch is one that is uniform in all directions. On the other hand, an anisotropic profile exhibits strong directional dependence. In Figure 2.1 both isotropic and anisotropic profiles of etched $(\bar{0}0\bar{1})$ silicon are illustrated.

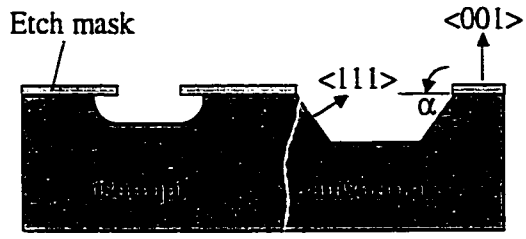

Figure 3.1: Cross-sectional views of micromachined (001) silicon. Wet anisotropic etching along <110> directions reveals {111} sidewalls with α=54.74°.

The structures revealed by wet anisotropic etching of silicon are dependant on the substrate's crystal orientation and the orientation of the masking pattern. Shown below is a schematic diagram of a (001) silicon wafer. The primary wafer flat identifies the scribe and break <110> family of directions (zone axes). To obtain an anisotropically etched profile as that shown in Figure 3.1 the masking pattern must follow <110> type directions.

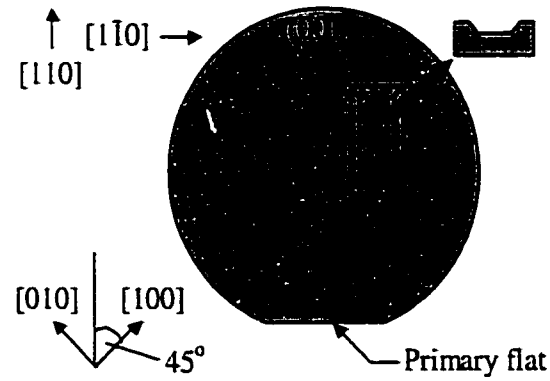

Figure 3.2: Schematic diagram illustrating the preferred direction for masking on (001) silicon wafers.

Anisotropic etching is also referred to as orientation dependent etching (ODE) as an appropriate etchant will attack the substrate's various crystal planes at different rates and is thus orientation dependent. The etching phenomenon "*apparently arises because*

different crystal planes present area densities of atoms and different surfaces which leads to different etch rates" [36]. The most important crystal plane etch rate ratio is that of the {001} family of planes to that of {111} type planes. As suggested in Figures 3.1 and 3.2, properly oriented patterns on (001) silicon result in anisotropically etched geometries defined by the slow etching {111} planes.

Popular anisotropic etchants include potassium hydroxide (KOH), tetramethyl ammonium hydroxide (TMAH) and ethylene diamine pyrocatechol (EDP). Of these three etchant systems, KOH exhibits the largest {001}/{111} etch rate ratio and so is preferable in terms of minimizing mask undercut. Unfortunately alkali metal hydroxides such as KOH attack aluminum and silicon dioxide and thus may contaminate gate oxides with mobile ions [37]. For this reason, unless strict measures [38] are taken to adequately protect susceptible areas, KOH is not postCMOS compatible. While EDP has been used in a variety of micromachining applications its high toxicity is of great concern. TMAH on the other hand poses fewer health problems. Its {001}/{111} etch rate ratio is considerably less than that of KOH, but unlike KOH it is postCMOS compatible. In fact, since TMAH is often used in developing solutions of positive photoresist, semiconductor-grade solutions are readily available.

In the work presented in this thesis wet anisotropic etching of silicon surfaces is to be used for realization of millimeter/submillimeter wave waveguides. In addition, a high-frequency packaging project is undertaken to fabricate transmission lines on the sidewalls of micromachined silicon. Successful development of these two projects requires that roughness of micromachined surfaces is minimized. The formation of hillocks on

micromachined surfaces has been noted in various investigations of wet anisotropic etching [39]-[43], and of course increase surface roughness.

It had been the early experience of the author that smoother micromachined surfaces were obtained with 25 wt. % TMAH as compared with 33 wt. % KOH – the two recipes initially attempted. In light of these results the author decided to utilize only 25 wt. % TMAH in subsequent studies. By no means does this choice indicate that in all cases TMAH is superior to KOH in terms of surface roughness. It does seem however that surface roughness of TMAH etched surfaces decreases with increasing TMAH concentration [39], [42] with virtually no hillock formation found above 22 wt. % TMAH [41]. One price to pay for using higher TMAH concentrations however is reduced etch rate. Shown in Figure 3.3 is an example of grooves micromachined in silicon using 25 wt. % TMAH held at 80°C. A typical etch rate for such features was found to be approximately 22 μm/hr with a {001}/{111} etch ratio of roughly 10:1.

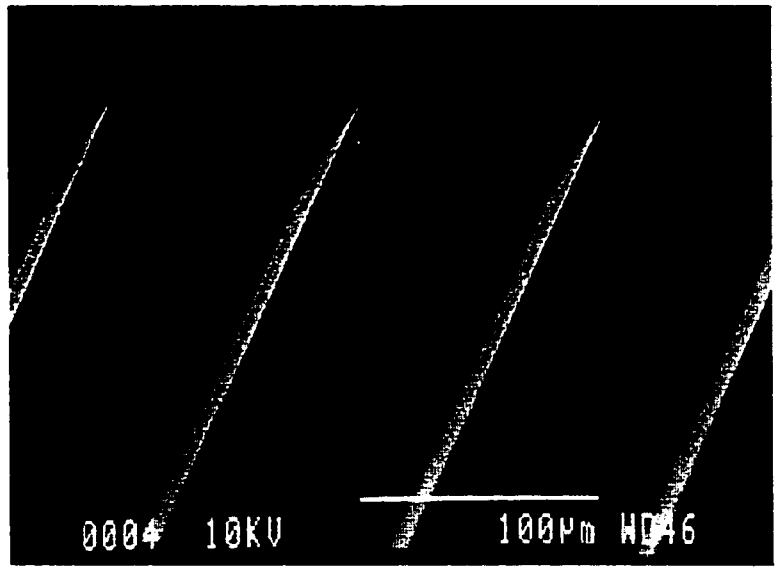

Figure 3.3: Scanning electron micrograph of micromachined grooves in (001) silicon. The features were etched with 25 wt. % TMAH held at 80°C.

The fact that wet anisotropic etching of silicon relies on crystal plane selectivity of the etchant, ultimately limits the geometries that can be defined. For instance, properly oriented concave corners can be perfectly resolved using anisotropic etchants on (001) silicon but convex corners cannot. Shown in Figure 3.4 is a scanning electron image of such features etched in silicon using the standard recipe given above.

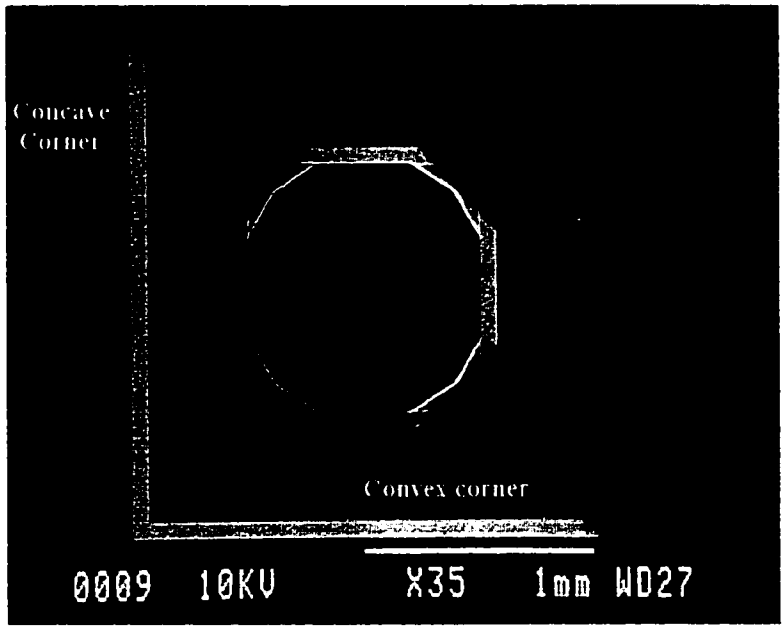

Figure 3.4: Scanning electron micrograph showing both concave and convex corners after anisotropic etching. The white lines added to the image suggest the original convex corners of the masking layer before etching.

In the figure an originally square mesa sits in the middle of a square moat. It is quite clear from the figure that concave corners are easily resolved. Convex corners on the other hand are subject to severe undercutting and so are quickly etched away. (In the figure, white lines forming the convex corners illustrate the original masking pattern.) A variety of techniques may used to compensate corners [44]-[47]. Each technique utilizes additional features incorporated on the mask at the locations of convex corners. During etching, these features are etched away to leave behind a more properly resolved corner.

Due to the additional space required for compensation features, there is a minimum necessary area around a convex corner for it to be properly resolved

In this work a technique perhaps first described in [48] is utilized. The corresponding compensation feature is an appendage pointed in the <010> directional family. Figure 3.5 gives a schematic representation of the compensation feature. In the figure, the lighter colored area is the region to be etched.

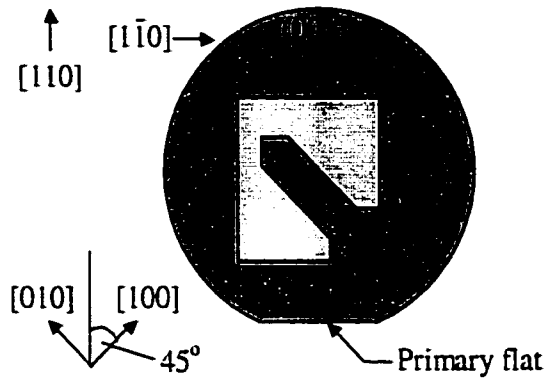

Figure 3.5: A sketch of a silicon wafer and masking pattern with appropriate compensation feature to allow for proper resolution of the corner after etching.

A scanning electron micrograph illustrating a partially etched convex corner is given in Figure 3.6. From the figure we see that the [010] compensation feature is partially etched and that the convex corner is taking shape. Both a concave and a convex corner etched in (001) silicon are shown in Figure 3.7. The convex corner was established using the [010] compensation scheme. We see that both corners are resolved quite nicely. The thin protrusion extending from the convex corner is a small remnant of the compensation bar – a few more minutes in the etchant and it would disappear.

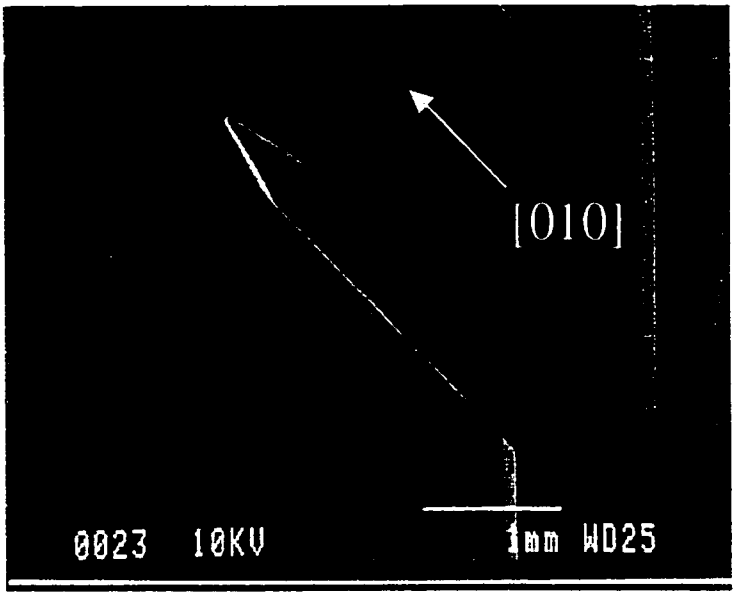

Figure 3.6: Scanning electron micrograph of a convex corner and a [010] compensation bar after partial etching.

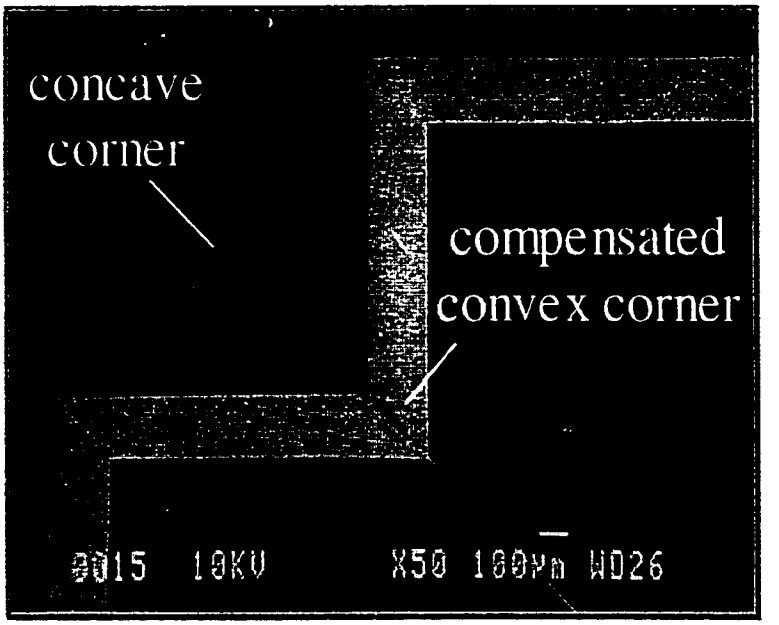

Figure 3.7: Scanning electron micrograph of a both a concave corner and a compensated convex corner after near complete anisotropic etching.

Of all the compensation features that the author has studied, it is felt that the [010] bar is the most elegant. Its design is remarkably straightforward and an understanding of its underlying principles allows a very convenient means of determining when the desired depth is reached during anisotropic etching of (001) silicon. To illustrate the proper design of a [010] compensation bar consider Figure 3.8.

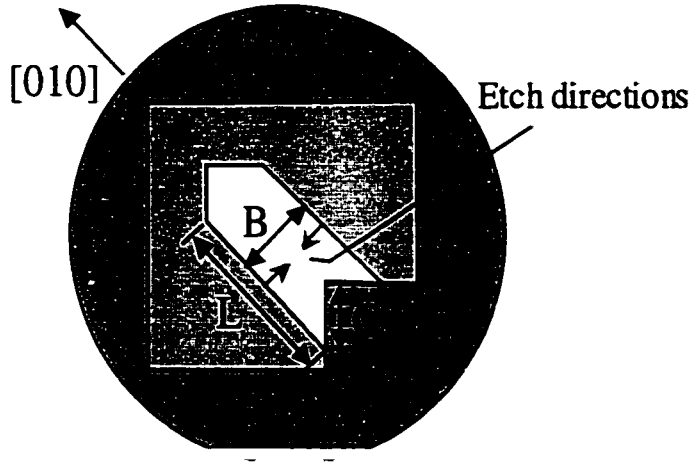

Figure 3.8: Schematic diagram illustrating of a [010] compensation bar.

If we take the desired etch depth to be "d" then the required dimensions of a [010] compensation bar dimensions are as follows:

$$B = 2d$$

and

$$C = \frac{B}{\sqrt{2}}.$$

It is not surprising that the B dimension of the compensation bar must be twice the etch depth. This result stems from the fact that the two planes of the compensation bar parallel to <010> type directions belong to the {001} family of planes -- that of the wafer surface itself. The two planes of the compensation bar in question are vertical with

respect to the wafer surface and etch laterally at a rate equal to that of the surface. These planes retreat and vanish leaving a compensated convex corner once the proscribed depth *d* has been reached. Thus one can determine when the desired depth has been reached by monitoring the evolution of a properly compensated convex corner. The dimension L depends upon the etchant used and the etch conditions. The author has found that a length of L = 5B to be more than enough when using 25 wt. % TMAH at 80°C. It should be mentioned that any compensation structure requires a certain amount of wafer real estate and thus convex corners must have enough room around them to allow for incorporation of the additional feature.

3.1.2: Deep Reactive Ion Etching

As mentioned previously, the development of various shapes using anisotropic wet etching relies on the relative selectivity among the crystal planes to the wet etchant. While smooth sidewalls are possible, realizable geometries are limited. Other techniques such a laser milling and reactive ion etching have been developed, and since they exhibit little if any crystal plane dependence, promise to alleviate these geometric restrictions. In this section the technique often referred to as deep reactive ion etching (DRIE) is considered.

A schematic diagram of the Surface Technologies Systems (STS) DRIE system used in this work is given in Figure 3.9. Operation of the system begins with loading the sample in a load-lock chamber, passing the substrate through the load-lock valve and running a helium leak check. Programming consists of selecting the flow rate of the etching and passivation gases, etching and passivation times, power and the process time.

Etching in a DRIE system typically occurs via a time-multiplexed gas-feeding [49] process. Such a process consists of a repeated cycling between successive etching and passivation steps and can perhaps be best understood with a process flow cartoon such as that given in Figure 3.10. This diagram applies to the STS Multiplex etch tool used in this investigation.

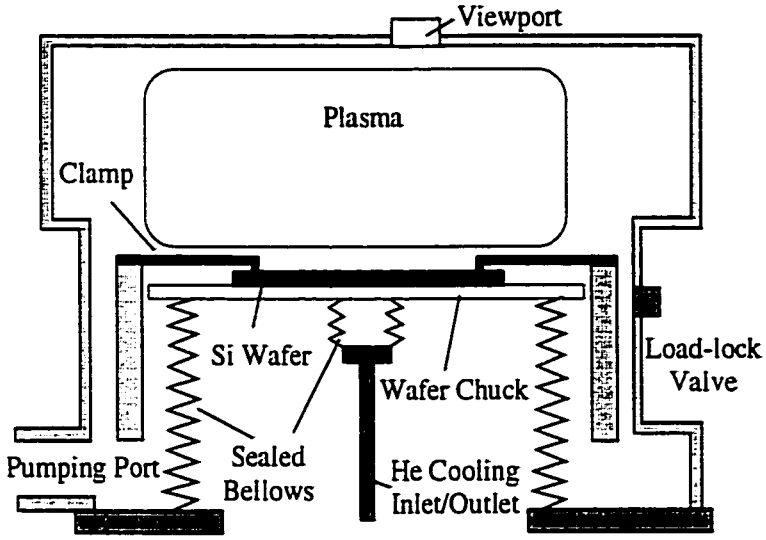

Figure 3.9: Schematic drawing of a DRIE system.

The pre-etch step in the figure shows the sample with its etch mask (~ 7 μm of 4620 photoresist was used in the work reported in this dissertation). After pressure stabilization, a passivation step (step 2 in Figure 3.10) is initiated by introducing C_4F_8 into the chamber. In this step a teflon-like polymer is plasma-deposited; a passivation step of 7 seconds was used in this investigation with on the order of 10 nm of polymer depositing in that time period.

Immediately after the passivation step the etch gas, SF_6 is introduced. The degree of anisotropy of this etch step (13 seconds long in all cases presented here) has much to do with the applied potential used to accelerate ions from the SF_6 plasma (see step 3).

Without acceleration, the silicon would be etched primarily by non-energetic reactive species in the SF_6 plasma (spontaneous thermal reaction) and thus form an isotropic type profile. As long as the reactive ion component (that component due to ion acceleration and the resulting breaking of Si-Si bonds) dominates the neutral reactive component, the etch profile will exhibit a pronounced degree of anisotropy.

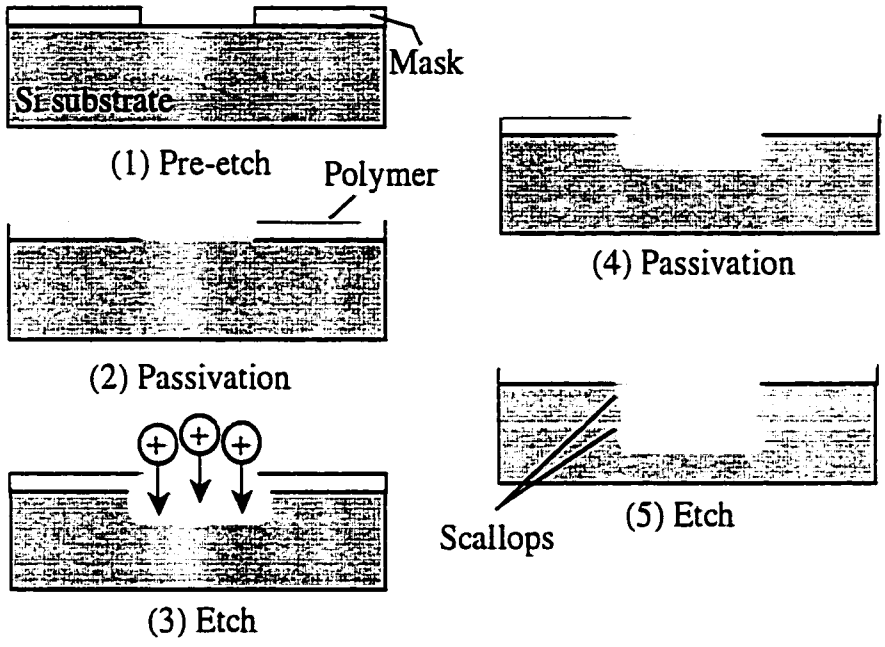

Figure 3.10: Schematic representation of the STS DRIE process flow.

The passivation layer deposited before each etch step helps to protect the lateral walls from etching and thus contributes to the anisotropy of the etched structure. The portion of the passivation layer lying in the plane of the wafer surface is removed rapidly by the accelerated ions but the layer remains on the sidewalls, thus protecting them. The passivation and etch cycling is continued for a proscribed period of time in accord with the anticipated etch rate. The etch rate was found to depend on the exposed area, but can be taken to be on the order of 5 μm/min.

The cycling between passivation and etching and the spontaneous nature of the SF_6 etch step, introduce a scalloped profile to the sidewalls. Both the height of the scallop and its horizontal depth can vary depending on conditions. Scallop depths from 50 to 300 nm have been reported [49].

The geometric restrictions imposed by anisotropic wet etching are lifted in the case of DRIE and there is no need for measures such as convex corner compensation. The sidewall profile can be controlled to a great extent by judicious choice of such parameters as etching time, passivation time, and RF power for instance. Representative scanning electron micrographs of deep-etched silicon features are given in Figures 3.11 and 3.12. The etched profile departs from normal by ~ 5°. The etch parameters used in the investigation are found in Appendix A.

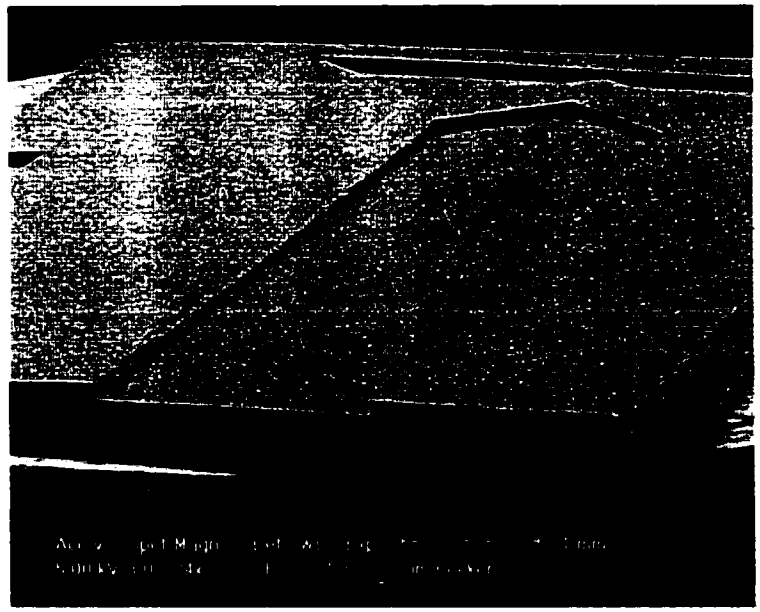

Figure 3.11: Scanning electron micrograph of deep etched silicon.

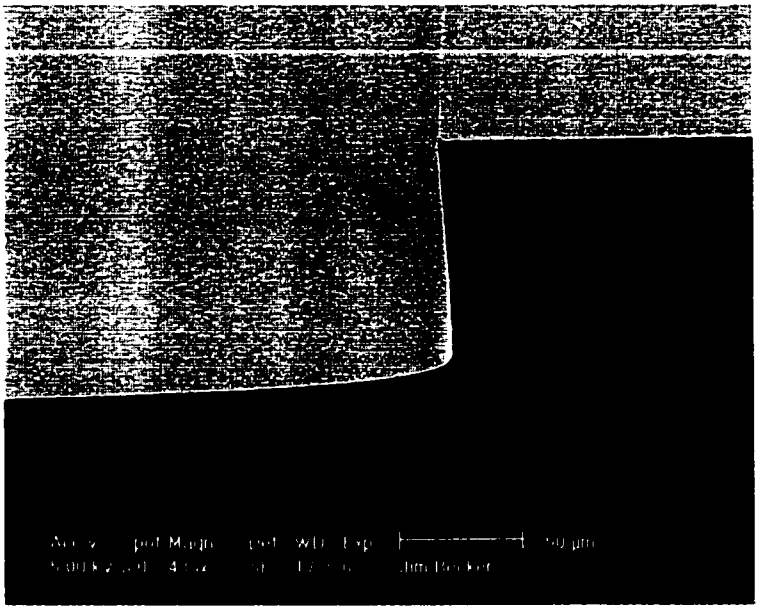

Figure 3.12: Scanning electron micrograph of a cross sectional view of a deep etched groove. Photoresist was used as a masking layer.

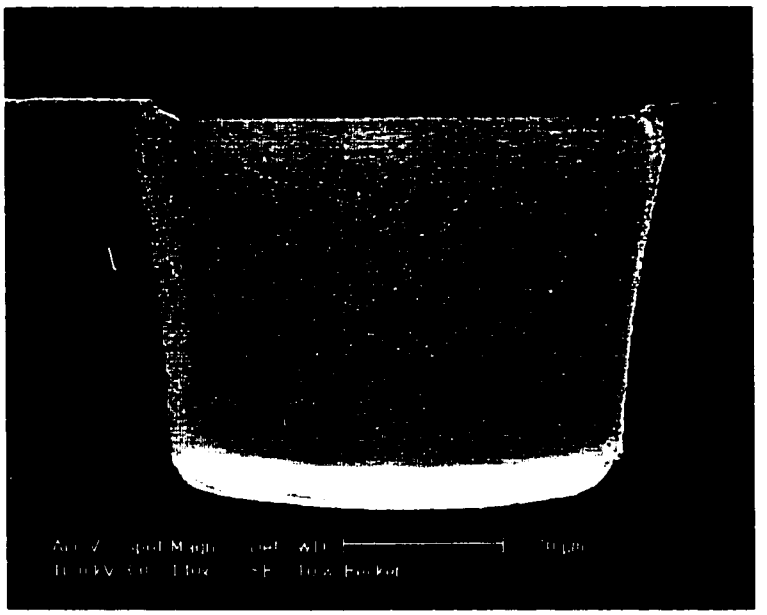

Figure 3.13: Micrograph illustrating the deep etch profile using silicon dioxide as a masking layer.

In [49] it is mentioned that excellent selectivity can be achieved using silicon dioxide and that with regard to induced surface roughness due to unequal mask recession, "*the*

use of hard mask materials such as silicon dioxide helps alleviate this problem." At the time the author was looking to the possibility of etching extremely deep channels and thus wanted a masking material that would provide the highest degree of selectivity. Minimization of surface roughness was also an important and so use of silicon dioxide as an etch mask was investigated. A cross-sectional view of a deep-etched channel in silicon using thermal oxide as an etch mask is given in Figure 3.13. From the figure, it is clear that the profile no longer exhibits nearly vertical sidewalls. It is believed that some degree of surface charging is the culprit, though further study is necessary to verify this possibility. In all subsequent work presented in this dissertation, photoresist is utilized as a mask for deep reactive ion etching.

3.2: Etching Uniformity and Surface Roughness

It is of course desirable to obtain excellent uniformity in etch depth across a wafer. To assess this in the case of TMAH an array of features were patterned and etched across ¼ piece of a 4 inch (001) silicon wafer (the typical sample size). A nominal etch depth of 300 μm was sought. The actual etched value was found to vary by ± 2% from the nominal as determined with an optical microscope.

Figure 3.14 is a photograph of a full 4 inch wafer that was deep etched in an effort to determine its uniformity characteristics. The nominal etch depth for the case of Figure 3.14 was found to be 110 μm (21.5 minute process) with an etch depth variation of ± 5% across the wafer. The actual samples used for fabrication of the transition and waveguide structures were ¼ wafer pieces and such pieces had to be mounted on full 4 inch wafers for processing in the STS. A uniformity check was done on a representative sample to ensure that a suitable bonding scheme was used. For mounting, 4620 photoresist was

spun on the 4 inch carrier (7 μm thick) and the ¼ wafer piece placed on the photoresist-covered carrier. The combination was then baked in an oven for 40 minutes at 110°C. This prolonged baking ensured that the photoresist was thoroughly dried and thus would not leave any residue on the STS wafer clamps. For a nominal etch depth of 117 μm a uniformity of better than 3% was achieved across the ¼ wafer piece.

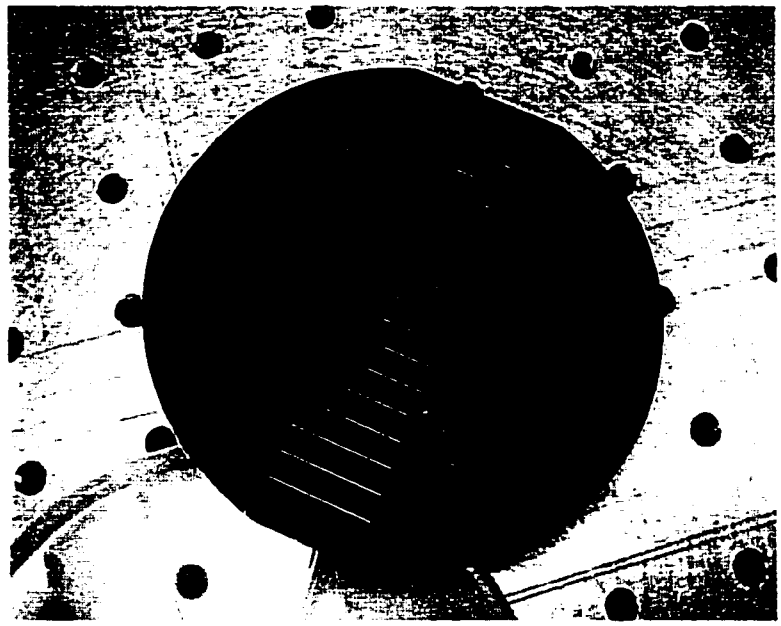

Figure 3.14: Photograph of the 4 inch wafer used to assess deep etch uniformity.

Achieving very smooth surfaces is of great importance in patterning features on the sidewalls of micromachined structures. Minimizing surface roughness is even more crucial in the development of high frequency waveguides as the loss in the guide is closely tied to surface quality. *"The two most natural ways to establish the roughness of a surface are to look at it and to run a finger over it"* [50]. This general statement effectively splits the assessment of surface roughness into two main categories, with the later means embodied by stylus type measurements. As a rather simple means to quantify the surface roughness of both wet anisotropic etching and deep reactive ion

etching, a stylus-based tool, the DEKTAK^3 surface profile measurement system [51], was used.

Figure 3.15 displays the results of several scans on three silicon surfaces, namely an unetched surface, one etched in TMAH and a third etched using the STS DRIE as described above. The results are displayed in terms of the rms roughness and arithmetic average roughness. These parameters are determined by first defining a mean surface value which may be expressed as

$$\sum_{i=1}^{N} z_i = 0$$

to ensure that the sum (N samples) of the vertical displacements (z-direction normal to the surface) is zero. The rms roughness (δ) and average roughness (R_a) are defined with respect to the mean surface level as follows:

$$\delta = \sqrt{\frac{1}{N}\sum_{i=1}^{N} z_i^2} \qquad [3.1]$$

and,

$$R_a = \frac{1}{N}\sum_{i=1}^{N} |z_i| \,. \qquad [3.2]$$

In Figure 3.15, error bars suggest the highest and lowest measured values (three scans were made for each data point displayed). From this figure we see that the un-etched surface was found to be the smoothest, though the TMAH-etched surface is nearly as smooth. The DRIE sample exhibits approximately twice the roughness of the TMAH-etched surface. To set these results in the proper perspective we must consider the limitations of the surface profilometer technique. These limitations arise from the finite size of the tip diameter (12μm in the case here) of the scanning stylus.

Consider Figure 3.16 that displays a schematic representation of a stylus traveling over a rough surface. The tip of a stylus should not be considered a perfect point, rather it has some diameter associated with it and thus may not be able to precisely trace a given profile. Figure 3.16 illustrates this point as the assumed spherical tip is unable to reach the bottom of narrow valleys. This suggests that high frequency surface fluctuations are missed.

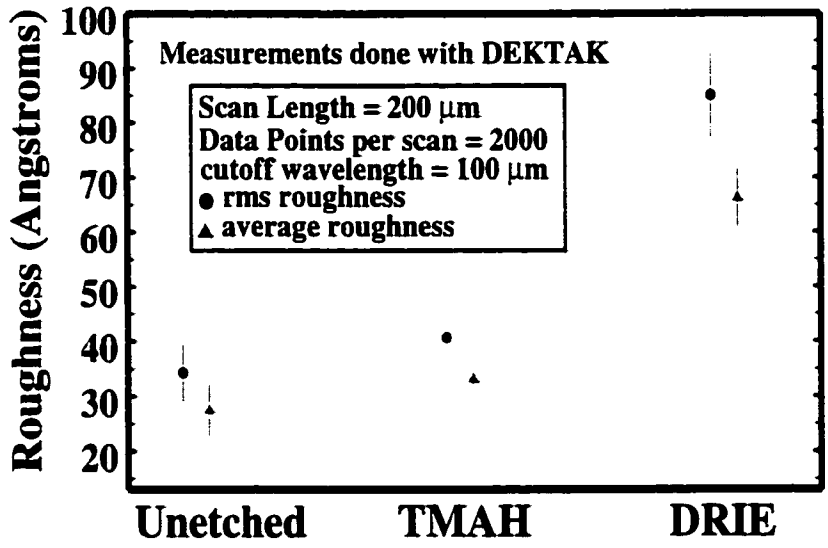

Figure 3.15: RMS and average roughness of various silicon surfaces – an unetched surface, one etched using TMAH, and one etched through DRIE.

Figure 3.16: Schematic representation of a stylus with circular tip traversing a rough surface. (Drawing after Figure 2.7 of [50].)

If for a moment we consider a simple sinusoidal surface defined as

$$y(x) = A\sin(2\pi fx), \qquad [3.3]$$

we may provide some suggestion at a limitation of the measurement data of Figure 3.15. In the above equation, "A" refers to the sinusoid's amplitude and "f" to its spatial frequency. The equation may be regarded as a parametric curve in using the following equations:

$$x = x$$

and

$$y(x) = A\sin\left(\frac{2\pi}{T}x\right).$$

In the above equations, "T" refers to the spatial period of the sinusoid. The curvature of a parametric curve is given [52] by equation 3.4. That is,

$$\kappa = \frac{\left|\dot{x}\ddot{y} - \ddot{x}\dot{y}\right|}{\left[\left(\dot{x}\right)^2 + \left(\dot{y}\right)^2\right]^{3/2}}. \qquad [3.4]$$

In equation 3.4 and all that follow, a single dot denotes the first derivative and the double dot, the second derivative. For a sinusoidal surface, the curvature reduces to as follows:

$$\kappa = \frac{\left|\ddot{y}\right|}{\left[1 + \left(\dot{y}\right)^2\right]^{3/2}}$$

and thus,

$$\kappa = \frac{\left|\left(\frac{2\pi}{T}\right)^2 A\sin\left(\frac{2\pi}{T}x\right)\right|}{\left[1+\left(\frac{2\pi}{T}A\cos\left(\frac{2\pi}{T}x\right)\right)^2\right]^{3/2}}.$$

The maximum value of curvature occurs at the peaks and troughs of the sinusoid, x = T/4 and x =(3T)/4 respectively. In such cases the curvature is given by

$$\kappa_{max} = \left(\frac{2\pi}{T}\right)^2 A = (2\pi f)^2 A.$$

This implies that the radius of curvature, ρ, is at its minimum at the points of maximum curvature, and is given by

$$\rho_{min} = \frac{1}{\kappa_{max}} = \frac{1}{A}\left(\frac{T}{2\pi}\right)^2 = \frac{1}{A(2\pi f)^2}.$$

Now if the radius of curvature at a point on the surface is smaller than that of the probe tip (r_{tip}), the stylus will not be able to precisely follow the surface. This means that to properly resolve a sinusoidal surface, the following inequality must hold:

$$r_{tip} \le \rho_{min} = \frac{1}{A(2\pi f)^2}.$$

The above equation may be reconstructed to yield the spatial frequency or period, which is given by

$$T = \frac{1}{f} \ge 2\pi\sqrt{Ar_{tip}}.$$

Assuming a 12.5 μm tip radius (that used to take the measurements of Figure 3.15) and sinusoid amplitude of 27.5 Å (the average roughness of the un-etched surface), the minimum spatial period for which such an amplitude of roughness could be resolved is

roughly 1.2 μm. In other words, given the radius of the tip used, the recorded value of 27.5 Å could accurately pertain to roughness with a characteristic period of 1.22 μm and not smaller. At the other end of the spectrum, the 66.2 Å of average roughness could not be accurately picked up from a roughness sinusoid with a period of less than 1.81 μm. It should be pointed out that a simple, single-frequency sinusoidal surface, though providing a convenient means to shed light on the limitations of stylus-based roughness measurements, most likely does not accurately represent a arbitrary surface. Rather, a true surface may be more accurately constructed with a series of sinusoids.

Both Figure 3.16 and the above simplified analysis put the results of Figure 3.15 in perspective. If the true roughness of the surface is rapidly varying and/or the roughness amplitude is great, the results of Figure 3.15 may significantly underestimate the true value.

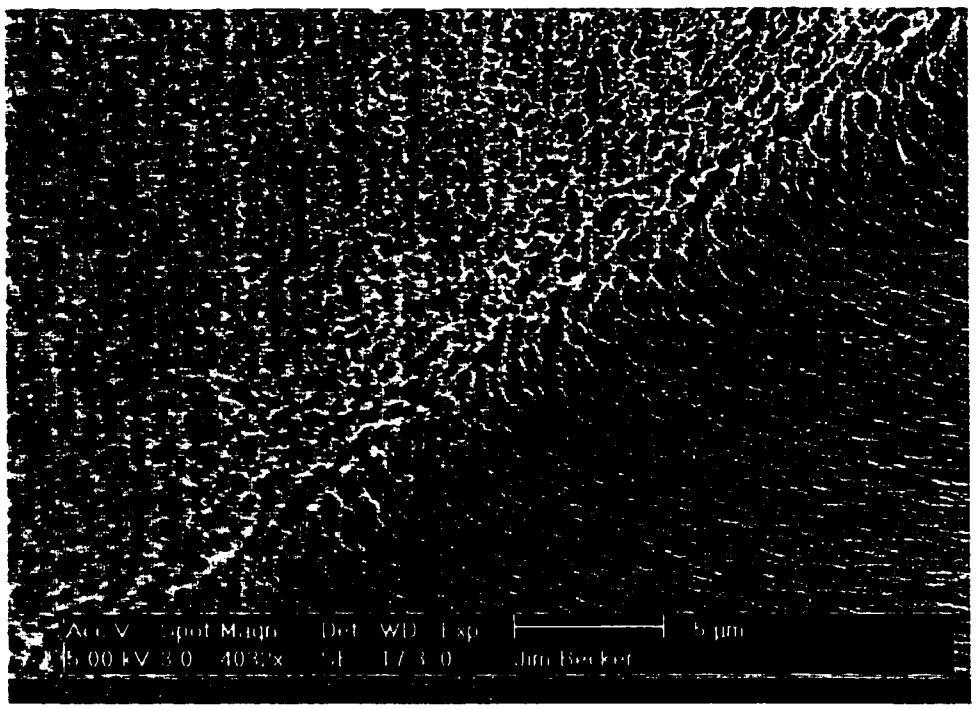

Figure 3.17: Micrograph of the bottom and sidewall of a DRIE feature.

In measuring the roughness of the various samples, only the bottom surfaces, and not the etched sidewalls were analyzed due to the geometry of stylus measurements. In the case of wet anisotropic etching, the sidewalls and the bottom surface of an etched structure appear to be of similar quality (see Figure 3.3). Contrast this with the case of a DRIE feature depicted in Figure 3.17 -- a close-up of Figure 3.12. The figure suggests that the sidewall is characterized by greater roughness, with a higher spatial frequency.

3.3: Handling Silicon Wafers of Various Thickness

A variety of silicon wafers were used in the development of the devices presented in this thesis. Wafers as thin as 100 μm and as thick as 2 mm were used. Typical processing called for wafer oxidation, sectioning, etching, metalization, dicing and bonding. Some process modifications were necessary in dealing with the various wafer types. For example, 100 μm wafers are susceptible to breakage and thus were mounted on glass slides for mechanical support. The mounting procedure, along with various fabrication recipes are given in appendix B. For oxidization, a special quartz boat was designed to accommodate the thick wafers, a schematic of which is given in Appendix C.

The starting wafers used in this investigation were all 4 inch in diameter and had to be sectioned into quarter-wafer pieces. With wafers of nominal thickness 500 μm or less, a simple scribe and break technique was used. With 2 mm thick silicon however, the scribe and break procedure yielded very rough wafer edges with significant presence of the {111} sidewall. To avoid this problem, a special dicing blade and flange set were obtained to cut through 2 mm wafers.

Figure 3.18 displays a scanning electron micrograph of the cross-section of a 2 mm thick piece of (001) silicon that has been anisotropically etched in 25 wt. % TMAH and

diced. Figure 3.19 shows a close-up of the tip of the V-groove illustrating that there is a visible degree of roughness introduced by dicing.

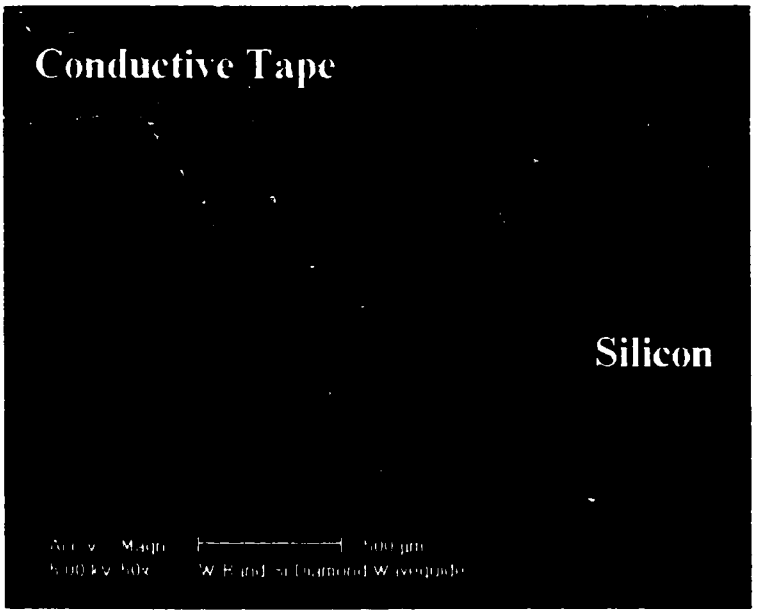

Figure 3.18: SEM image of anisotropically etched silicon, diced using a diamond-tipped blade.

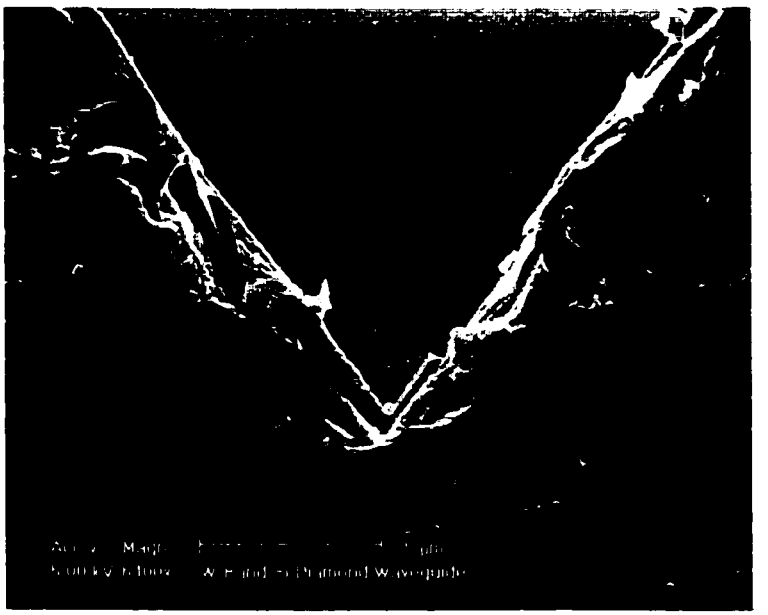

Figure 3.19: Close-up view of a diced cross-section of a V-groove anisotropically etched silicon.

Chipping is also a potential problem in dicing as demonstrated in Figures 3.20 and 3.21. Further exploration into optimizing the dicing parameters (e.g. spindle speed, feed rate, depth per pass) may improve the quality of the cut. Finally improved surface finish may be achieved through polishing.

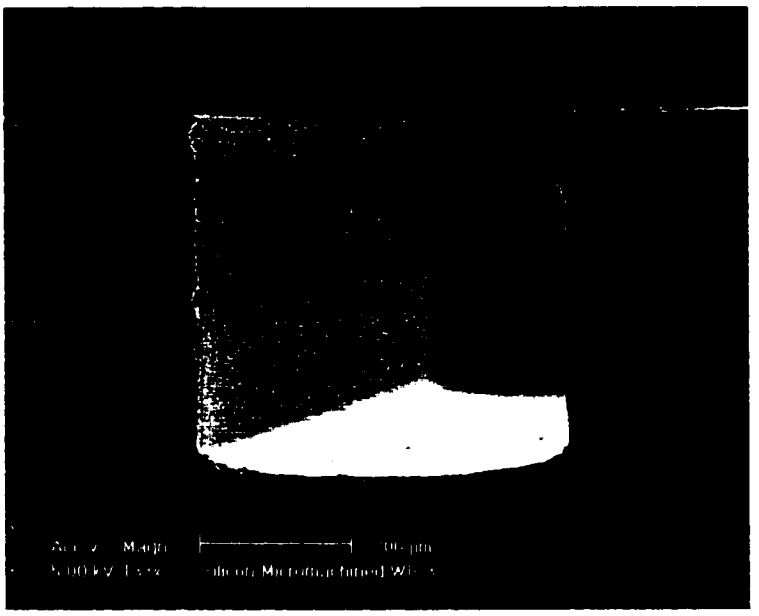

Figure 3.20: SEM image of a diced section of a deep-etched trench.

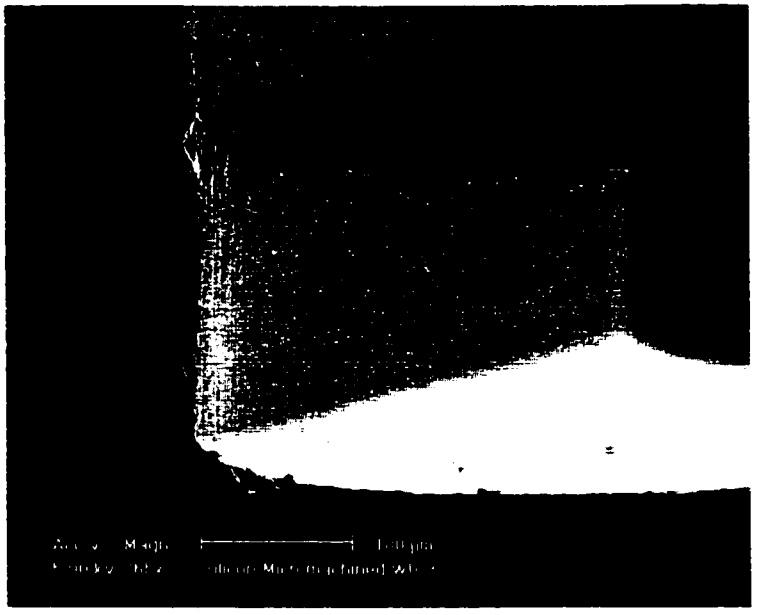

Figure 3.21: Close-up of a deep-etched trench

3.4: Simulation Tools

The reliance on high-performance electromagnetic simulation tools for the development of the various transitions investigated in the work will be underscored by the results of the analytical investigation of a magnetic loop transition described in chapter 7. The software package High Frequency Structure Simulator (HFSS) by Ansoft [53] was utilized extensively in the work presented herein. This software package allows the user to construct an arbitrary three-dimensional structure composed of material of varying constitutive parameters, and to excite the structure with well-defined electromagnetic sources. HFSS utilizes a finite element method to examine the fields within the structure, and provides the S-parameters of the structure as well as a graphical account of the fields associated with the structure and the excitation.

Three other simulation tools were utilized in the work presented here, namely IE3D by Zeland [54], Maxwell 2D by Ansoft [55], and LIBRA by HPeesof [56]. IE3D was utilized to examine the behavior of transmission line structures when full wave simulation was not necessary, Maxwell 2D provided a good estimate of the impedance of various transmission lines, and LIBRA used to model the various structures using lumped and distributed elements.

3.5: Measurement Techniques

An HP8510-based vector network analyzer test setup was the primary measurement tool used in the work presented herein. A photograph of the test setup is given in Figure 3.22. The system consists of an HP8350B sweep oscillator, HP8516A S-Parameter test set (45 MHz-40 GHz), HP8510A millimeter-wave controller, HP W85104A millimeter-

wave test set, HP83640L series swept cw generator (10 MHz-40 GHz) and an Alessi probe station.

Direct measurements of the transmission characteristics of diamond waveguides were accomplished using an HP W11644A WR-10 calibration kit (thru, short, offset short and matched load). On-wafer measurements of the FGC-to-micromachined waveguide discussed in chapter 7, were calibrated using a thru-line-reflect (TRL) protocol [57], controlled through the software package MULTICAL [58]. Model 120 GSG-150-BT picoprobes from GGB Industries were used for investigations in W-band and Model 40A GSG-150-DP GGB picoprobes for the 2-40 GHz measurements of chapter 5.

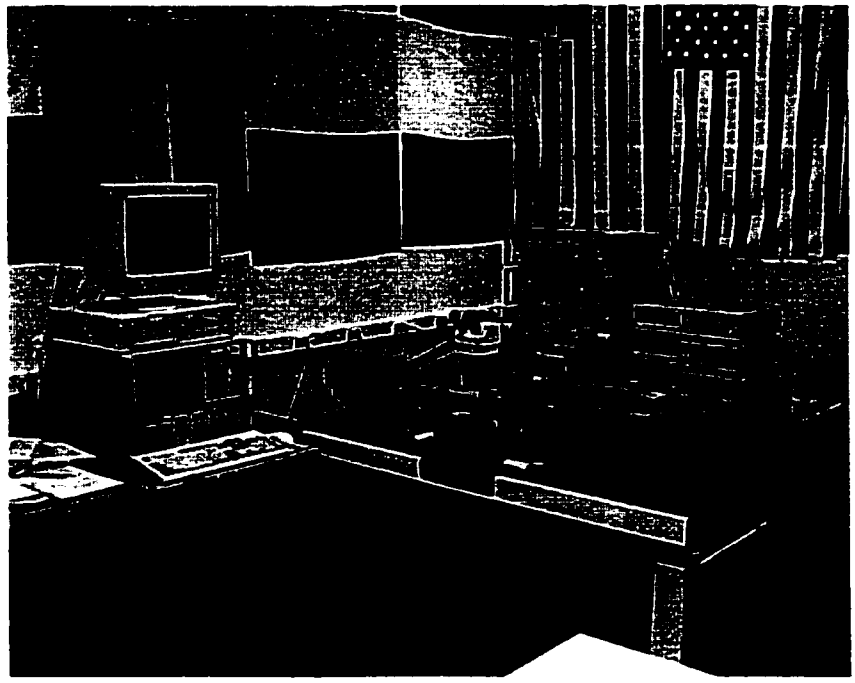

Figure 3.22: W-band measurement set-up.

3.6: Summary

This chapter presented several of the techniques and tools used to design, fabricate and test the devices presented in the later chapters of this thesis. One key fabrication

technique used in this work but not discussed in this chapter, is electrophoretic deposition of photoresist. Rather, the entirety of chapter 4 is devoted to the development of this technique toward the aim of patterning metal features on the various facets of micromachined silicon.

CHAPTER 4

ELECTROPHORETIC DEPOSITION OF PHOTORESIST AND 3D PHOTOLITHOGRAPHY ON SILICON MICROMACHINED SURFACES

4.1: Introduction

The application of photoresist is typically carried out using a "spin-on" technique as depicted in Figure 4.1. In such a process, the sample to be coated is secured via vacuum to a chuck that can rotate at a proscribed rate, for a proscribed time. Photoresist is then applied onto the sample using a dropper or syringe for example, and the sample is finally set to spin. The spin speed, spin time and type of photoresist determine the ultimate resist thickness. For example, one can spin Shipley's SC-1827 resist for 30 seconds at 3000 rpm and expect a consistent resist thickness of approximately 2.7 μm.

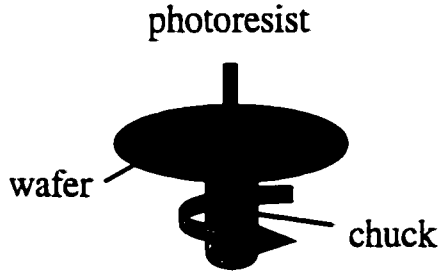

Figure 4.1: Photoresist application via conventional wafer spinning

For this study it was desired to simultaneously pattern features in the depths of silicon micromachined cavities, along cavity sidewalls and on the top surface of micromachined

wafers. Shown in Figure 4.2 is a scanning electron micrograph of a 300 μm deep cavity (etched in a silicon wafer) on which SC-1827 had been spun at 3000 rpm for 30 seconds. The micrograph reveals a photoresist coverage with significant streaking of resist near corners on the top surface, accumulation at the junction of merging crystal planes internal to the cavity, and little coverage on the ledge that extends into the cavity.

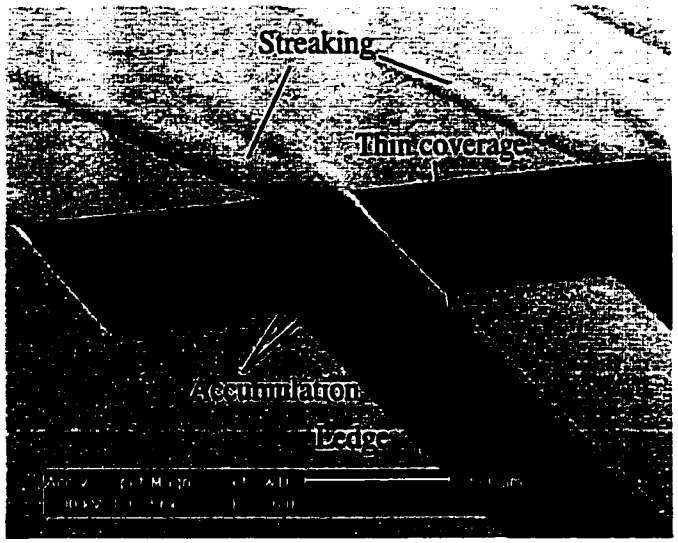

Figure 4.2: Electron micrograph of a silicon micromachined structure coated with "spun-on" resist. The coating is found to be quite nonuniform.

Near conformal coverage of photoresist is required for consistent realization of patterns that may exist on all wafer surfaces (i.e top surface, bottom of micromachined cavities and along cavity sidewalls) and thus the typical means of photoresist application (i.e. spinning) fails on micromachined surfaces. In this chapter we explore electrodeposition [59] as a means to achieve nearly conformal coverage of photoresist on silicon micromachined structures. After a brief introduction of the technique, a thorough accounting of the development of the required process will be given. The chapter will

end with a summary of suitable process parameters and suggestions to improve the process.

4.2: The Electrophoretic Deposition (EPD) Process

Instead of spinning photoresist, in electrophoretic deposition (EPD) of photoresist, the sample to be coated is immersed in an aqueous solution of photoresist, the sample then serves as either anode or cathode in an "electroplating-type" process. EPD consists of two steps, electrophoresis and deposition. Electrophoresis is simply the motion of charged particles, held in a suspension, under the influence of an electric field. Deposition may be considered as the coagulation of particles onto a substrate [60]. In a positive-depositing resist process, such as that explored in this investigation, the sample acts as the anode and a metal plate serves as the cathode. Such a process is termed "anaphoretic" as the resist particles drift toward the anode. (In a negative-depositing resist process, a "cataphoretic" process, the sample acts as the cathode and a plate electrode serves as the anode.)

EPD can be accomplished in one of two modes. In *constant-voltage* EPD, the applied potential between the electrodes is held constant. Such a process tends to be self-limiting if the material being deposited is electrically insulating in nature. This may be explained by the fact that an ever-increasing portion of the applied potential drops across the depositing film and is thus no longer available to drive electrophoresis. Constant-current EPD on the other hand, requires the current to be held constant, thus necessitating an increased potential difference between the electrodes.

The photoresist used in this investigation (Shipley's PEPR 2400, a positive-depositing photoresist) is an organic polymeric material, made up of micelles on the order of 100 nm

in size suspended in water and typically maintained at around 10% solids. These micelles are stable charged entities that, though tiny, contain the entire "microenvironment" of the photoresist. That is, each micelle contains the cross-linking polymer, photoinitiators and contrast-enhancing dye that make up a typical photoresist. Upon application of an electric field, the charged micelles migrate to the anode (the conductive substrate), are neutralized via the products of the electrolysis of the dispersing medium (water in this case), and thus agglomerate as an uncharged film on the anode surface [61], [62].

4.3: Electrodeposited Photoresist in the Printed Circuit Board Industry

The needs of the printed circuit board manufacturing community helped give birth to the development of electrodeposited (ED) photoresists in the 1980's. The generally accepted 3 mil (~ 75 μm) resolution limit of dry films, and the inability of conventionally applied wet resists to sufficiently cover via holes, spurred its development in the quest to develop miniaturized circuits with landless vias. At the present time, approximately thirty ED photoresist installations are being run in the printed circuit board (PCB) fabrication lines in Japan. Processes such as Toshiba's buried bump interconnect technology (B2it) [63] and A-Net's multilayer process [64] for cellular phone motherboards utilize ED resist in some form.

PEPR 2400 was developed specifically for the printed circuit board industry to be used as a part of a print and etch process. Shipley advertises the resist's ability to resolve 1 mil features, allow for landless, blind and buried vias, its excellent adhesion to copper surfaces, and its place as a key element in sequential multi chip module (MCM) production [65]. *In the present work, PEPR 2400 is used to develop metal patterns on*

the sidewalls of anisotropically etched (001) silicon, representing a departure from its original designed use.

4.4: The Electrophoretic Deposition Apparatus

A rather simple, but effective, electrophoretic deposition system was set up. The system consists of a pyrex vessel (either a 4L rectangular vessel or smaller beaker) which holds the photoresist solution. A polypropylene cover was fit with banana plug receptacles for the anode (center receptacle) and on either side of the anode, two similar receptacles for the cathode(s). If both sides of the sample are to be covered, a cathode is placed on either side, otherwise the sample faces a single cathode. There are two possible electrode spacings for dual-cathode deposition (i.e. two-sided deposition), 1.5 in. and 2.5 in. If one choses single-cathode deposition, the operator has a choice of 1.5, 2.5, 4 and 5 inches for the electrode spacing. Altering the electrode spacing allows for the possibility of exploring different electric field configurations.

The samples and electrodes are connected using polypropylene tubes which house a 14 gauge lead, terminated on one end with a banana plug and on the other with an alligator clip. The clip is used to hold either a sample or a rectangular stainless steel plate cathode. Each cathode is a piece of 60 mils thick, 316 stainless steel (cut 2.5" by 3.5" in cross-section for the 4 L tank and 1.5" by 2" for smaller beakers). The electrodes are connected to the leads from the supply using wing nuts to ensure that the cable does not disengage thus potentially exposing the operator to high voltage on these lines (up to 500V). The cable is a Royal Electric 14/3 SOW-A cable (i.e. a water-resistant, 14 gauge, 3 lead line). Though roughly 15 feet of cable separate the supply from the tank, negligible voltage drop on the line exists. For example, under the application of 100.0 V

according to the power supply, an independent measurement of the voltage at the sample connection was found to be 100.0 V. It should be noted that for safety reasons the power supply was far removed from the actual deposition tank.

The employed dc supply, the Hewlett-Packard HP 6035A (base rating: 0-500V, 0-5 A, 1000W), may be operated in either constant voltage or constant current modes. The nature of the front panel controls of this supply do not allow the operator adequate control of the voltage/current and deposition time (deposition time is typically between 10 and 60 seconds) for precise depositions. To overcome this problem, a program for constant voltage operation was written using HP-VEE software from Hewlett-Packard. The program allows the operator the ability to program the desired input voltage and deposition time. The program gives a running display of the measured current (constant voltage mode). Recalling that deposition is self-limiting in the constant voltage mode, a "real time" graphical display of the measured current allows the operator the ability to cut a deposition when the current falls to a desired level. An output file of the current profile of a deposition is automatically created. Operation instructions for the deposition system are given in Appendix D.

Shown in Figure 4.3 is a picture of the tank. Due to the health risks involved in using the photoresist, depositions are done under a fume hood. Figure 4.4 shows the underside of the cover, a cathode and tube connector. Finally, Figure 4.5 is a photograph of the supply and computer controller.

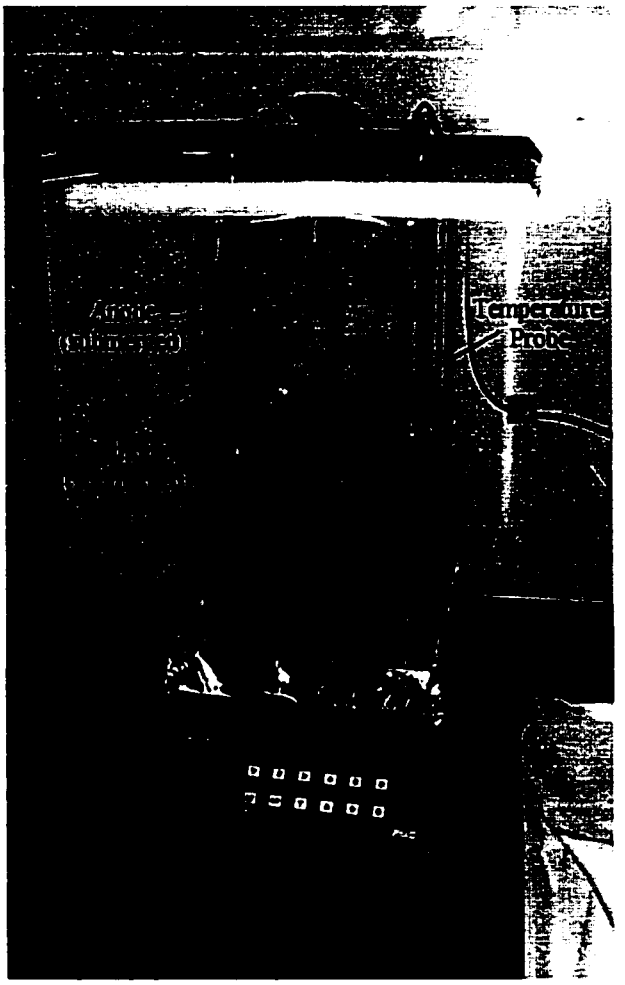

Figure 4.3: The photoresist deposition tank.

4.5: Calibration Of The Deposition System

There are several parameters that may be monitored to assess the quality/state of the photoresist solution and that govern the deposition. The first is the percent solid content, which should remain in the 9-11% range. To determine the percent solid one may simply take a small sample (say ~ 5 grams) weigh it, and then place it in an oven at 105°C for ~1.5 hours to remove the liquid content. The sample is then weighed again and the percent solids is then given by:

$$Percent\ solids = \frac{weight\ of\ sample\ before\ drying}{weight\ of\ sample\ after\ drying} x100.$$

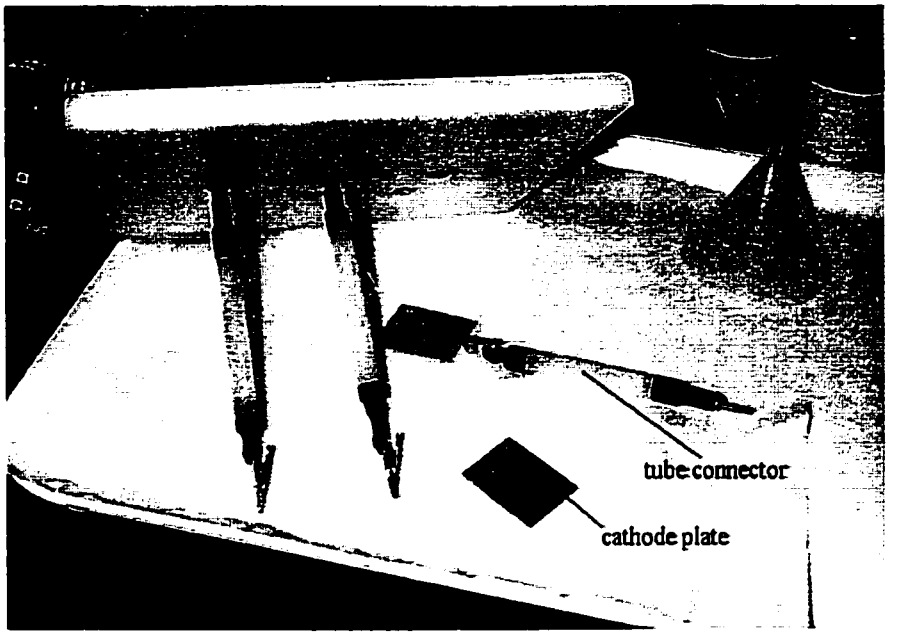

Figure 4.4: Underside of tank cover showing "tube connectors" and stainless steel cathode plates.

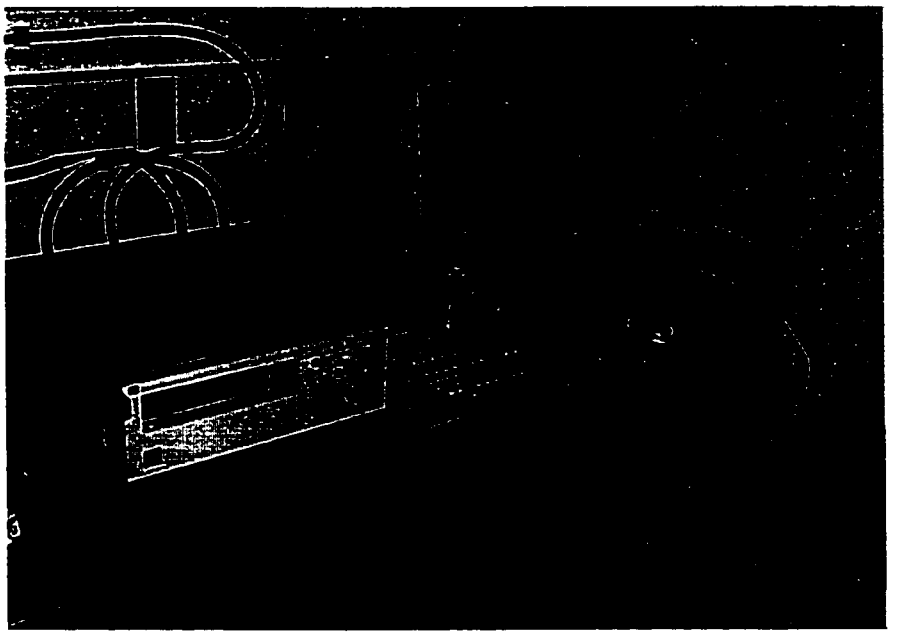

Figure 4.5: Power supply with computer controller

In this investigation, a new photoresist bath consisted of a 1:1 mixture of PEPR 2400 and deionized water; such a solution gives a percent solids of ~ 10%. The final resist thickness exhibits a strong dependence on bath temperature. Shipley [66] contends that the resist thickness can vary by more than a factor of 2.5, with *increasing* temperatures yielding *thinner* resist layers. In this investigation the bath was maintained typically at 30 ± 1 °C with the temperature monitored by an immersion probe.

Another means of controlling the final resist thickness is to use the thickness controlling agent, PEPR 2400 TC (a Shipley product). In amounts of ~ 10-15 g/L, PEPR 2400 TC may help reduce resist thicknesses by more than a factor of 2.5 [66]. PEPR 2400 TC was not used in this investigation. Finally the deposition voltage, deposition time and electrode/bath geometry will affect resist thickness.

In light of the number of parameters that affect the deposition, a few comments should be made. Either frequent monitoring and subsequent correction of the bath contents should be undertaken, or entire bath replacement should be implemented once depositions begin to deteriorate. In a printed circuit board production setting where tanks greater than 75 gallons may be used, continuous bath monitoring and correction are automated. Such systems, though complicated, keep costs down and allow for continuous use. Due to the small-scale work in this investigation, it was decided that the best method would be to establish an understanding of the behavior of our system based on a 10% solids PEPR 2400 solution, held a 30°C (middle-of-the-road values). Deposition voltage and time would be the two primary factors which would then be used to control resist thickness.

If consistent behavior could be achieved with reasonably fresh solution, it was decided that once the depositions began to deteriorate, the photoresist bath would be replaced. It should be noted that at the time of this investigation PEPR 2400 was approximately $655/gallon. As of November 2000 the price went up to over $1000 per gallon.

After a period of typically 24 hours, resist depositions would appreciably deteriorate. At one point the system was left for several weeks without use. Upon restarting the system, deposition of the resist did not occur as a thin film, rather as a series of clumps. It is believed that a significant portion of the solvent content of the resist was lost during this down time, drastically altering the viscosity of the solution. In an effort to reduce this supposed solvent loss, the resist bath would be bottled immediately after use. Finally, before a deposition on a meaningful sample was attempted, deposition on a dummy sample or two was undertaken. It was found that the deposition quality, at least in terms of visual uniformity, improved after subsequent depositions. This was found to be especially true after the solution had been residing in the tank unused for more than an hour.

Shown in Figure 4.6 are typical current profiles of 20 second constant-voltage mode depositions. Naturally, consistent deposition results were sought and Figure 4.6 is a plot of the resist thickness versus deposition voltage for several 20 second depositions; for each deposition voltage, two or three trials were made. The final resist thickness was determined with a DEKTAK profilometer that was used to examine the resist contour of patterned samples.

The resist was found to vary over the π inch^2 area by about 0.4 μm on a given sample. The variation in average thickness on separate samples was found to increase with deposition voltage as evident in Figure 4.7. Some variation may be expected as the sample was not totally immersed in the bath (the area around the alligator clip is held outside the solution to avoid coating the clip), and therefore the sample area immersed may vary somewhat from sample-to-sample. So too, a look at the inset of Figure 4.6 indicates that the deposition current was still significant at the termination of the deposition. Since the current increases with deposition voltage, differences in deposition conditions between runs will induce a greater thickness variation as the deposition voltage increases (again, as suggested in Figure 4.7).

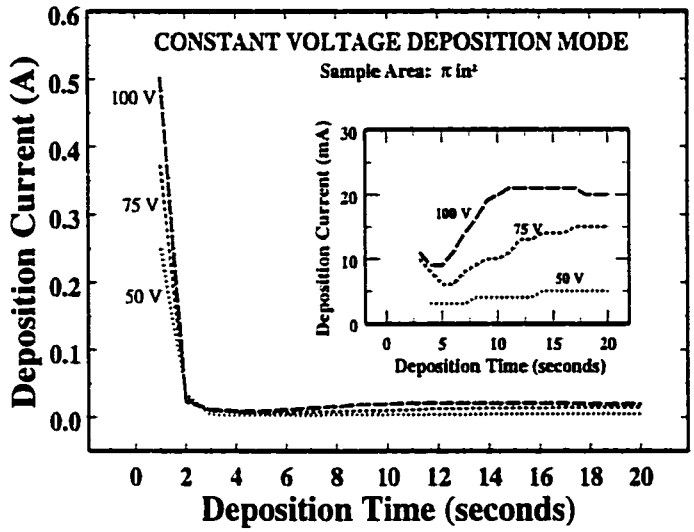

Figure 4.6: Typical deposition current profiles under constant voltage operation (all depositions: 20 seconds, 30°C).

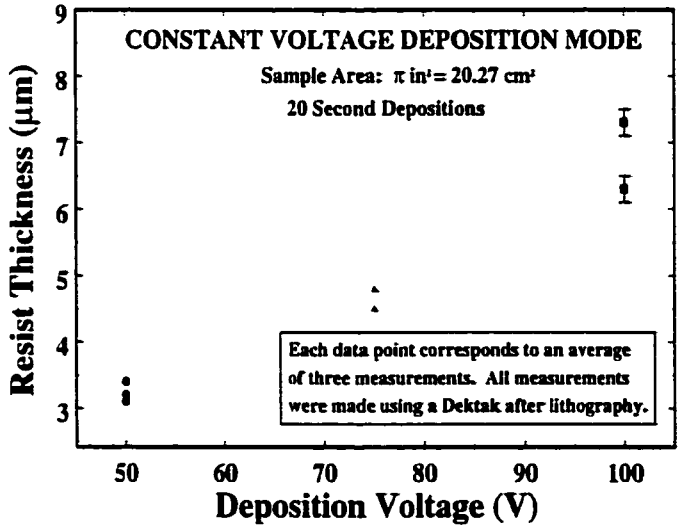

Figure 4.7: Resist thickness versus applied voltage under constant-voltage mode depositions. Resist thickness was determined after lithography; error bars on the 100V depositions are suggestive of those for other deposition voltages.

Shown in Figure 4.8 is a scanning electron micrograph of a cross-section of a cavity covered with PEPR 2400 (50 volt deposition for 20 seconds). The resist coating was found to provide consistent resist coverage over the entire micromachined surface,

though perfectly conformal coverage was not obtained. Roughly 3 μm coat the top surface (not shown), whereas approximately 5 μm cover the bottom surface. The greater thickness at the cavity bottom is believed to be an artifact of increased surface tension at the junction between the bottom surface and the merging {111} plane. The effects of the surface tension phenomenon, most evident at the junction where the resist thickness reaches a maximum vertical extent of 7.5 μm, carries over along the cavity bottom but does decrease somewhat as one moves further from the sidewall/bottom junction. As will be demonstrated below, simultaneous patterning on the top and bottom surfaces and along the cavity sidewall is quite possible using photoresist coverage as shown in Figure 4.7. Due to the increased resist thickness at the bottom of the cavity, careful attention must be given to proper exposure and development, factors that will be discussed below.

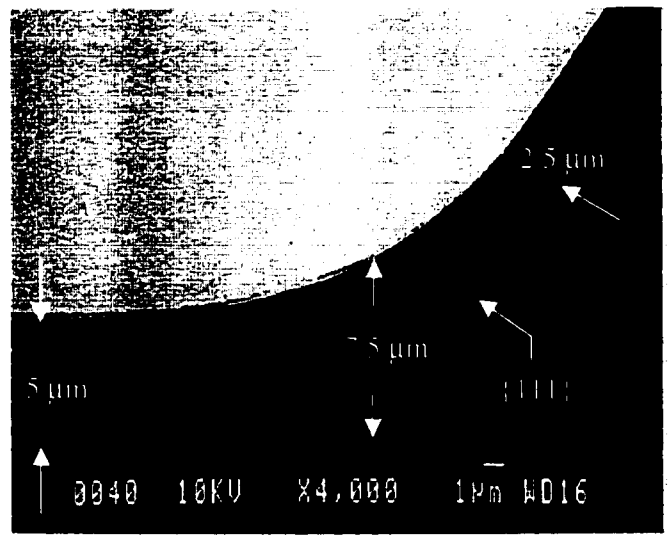

Figure 4.8: Cross-sectional view depicting the as-deposited coverage of PEPR 2400 on the bottom of a silicon micromachined cavity and the merging {111} sidewall. The thickness of the resist in various locations is depicted. The resist thickness on the top surface (not shown) is approximately 3 μm.

4.6: Patterning PEPR 2400

Shipley, the manufacturer of the PEPR 2400 supplied a brief "process manual" [66] suggesting certain chemicals to be used for developing and stripping the resist as well as information regarding drying and exposing the resist. The resist is most sensitive to light in the 380-420 nm range. For this investigation a Karl-Suss MJB-3 mask aligner was used. This mask aligner is configured to give UV radiation of 20 mW/cm^2 in the primary exposure range between 350 and 500 nm with a peak output at 405 nm.

As a first effort, the definition of FGC (finite ground coplanar) lines along the sidewalls and in the depths of a micromachined cavity was attempted. Figures 4.9 and 4.10 are scanning electron images of the first results. The fabrication parameters were as dictated in the Shipley process manual.

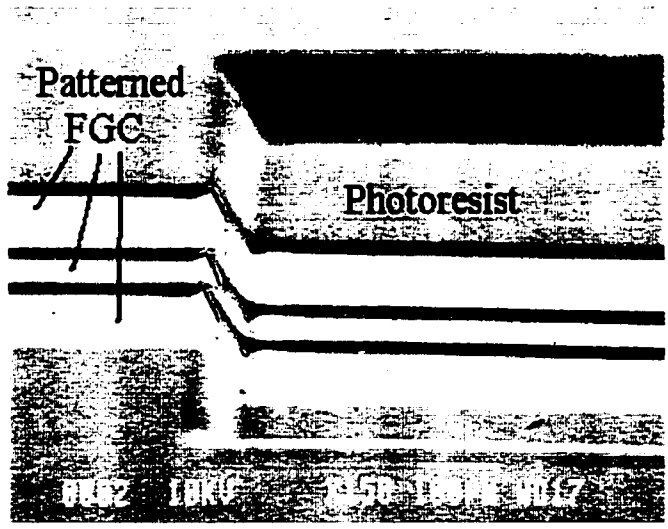

Figure 4.9: First attempt at lithography with PEPR 2400 – FGC mold, cavity depth of 70 μm.

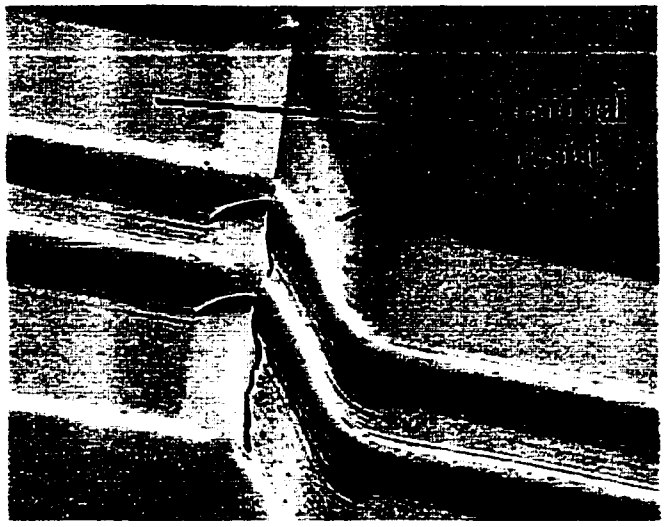

Figure 4.10: Close-up of the ledge of another cavity. Residual resist is evident and overall pattern is poorly delineated.

The mask was designed such that the developed pattern would act as a plating mold for the FGC lines. In such a layout, photoresist should be developed away from what are to become the plated lines. From the images we see that while a pattern is evident, it is quite poorly defined. Undeveloped resist remains in undesired locations, and the resist itself suffers from the existence of numerous pinhole defects.

Further investigation has led to explanations of these problems, and suitable means for avoiding them. Pinholes in the as-deposited resist occur in greater numbers as the deposition voltage increases. Shown in Figure 4.11 is a photograph of a series of short circuit-terminated FGC lines that were developed using a resist that was deposited at 100 V for 20 s. By using a sufficiently low deposition voltage, the problem of the development of pinholes may be mitigated. It is believed that pinholes evolve during deposition due to the existence of hydrogen bubbles (near the cathode) and oxygen bubbles (near the anode) that may accumulate on the wafer surface during the electrolysis of water. The substrate may be mechanically vibrated to help prevent such bubbles from remaining on the substrate surface [67].

Pinholes may also result if the substrate surface is contaminated prior to deposition [62]. Since low-voltage depositions lead to a thinner and thus more "patternable" resist (i.e. thinner resists allow the mask to come into closer proximity to the surface to be patterned), and since pinhole formation is not a severe problem at the low deposition voltages used, substrate vibration was not explored. The "pinholing" just described is not that depicted in Figures 4.9 and 4.10. The pinholes or "pockmocks" evident in these figures are due to the harsh effects of the developer and insufficient solvent removal during softbaking. A more suitable developer was determined experimentally and is discussed below.

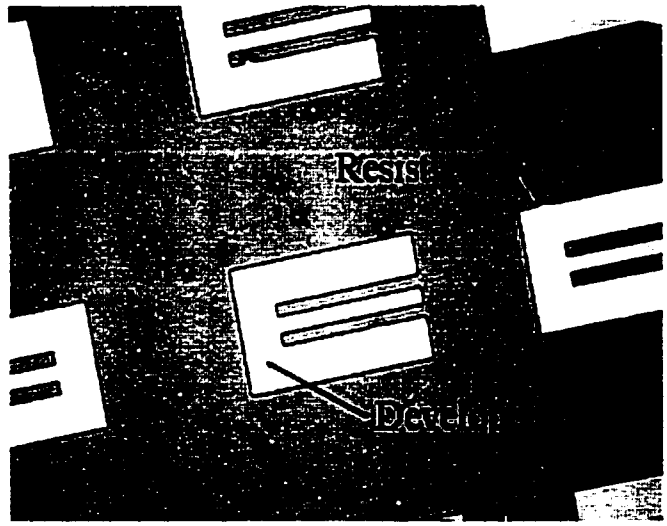

Figure 4.11: A photograph of patterned FGC short circuits illustrating the pinholes that form during large voltage depositions.

The images in Figure 4.9 and Figure 4.10 suggest that resist development may indeed pose a problem. The Shipley process manual [66] suggests a 1% sodium carbonate solution held at 38°C to be a suitable developer. Linder [68] et al. have found that sodium carbonate tends to dissolve unexposed PEPR 2400 resist rather rapidly (and attacks aluminum). In light of this fact they, "*elaborated a different development*

procedure" which *"features no noticeable attack of unexposed resist."* Unfortunately they are not able to disclose their "special developer" as the company who holds the rights to their research wishes to keep it a trade secret [69]. Shipley suggests that 0.75% sodium hydroxide (NaOH) held at 55°C be used as a PEPR *strippper*. It was felt that perhaps a more dilute form of NaOH, maintained at a lower temperature, might act as a suitable *developer*. Several concentrations of NaOH were explored; all subsequent development was done at room temperature.

Alongside the need to determine a suitable developer, an adequate softbake protocol was required. Initial attempts were carried out using a hotplate held at 105°C with baking times of 1 and 2 minutes. (The softbaking step when processing with Shipley's 1827 is typically done in this range.) Sufficient softbake was found to be critical in establishing well-defined photolithographic patterns.

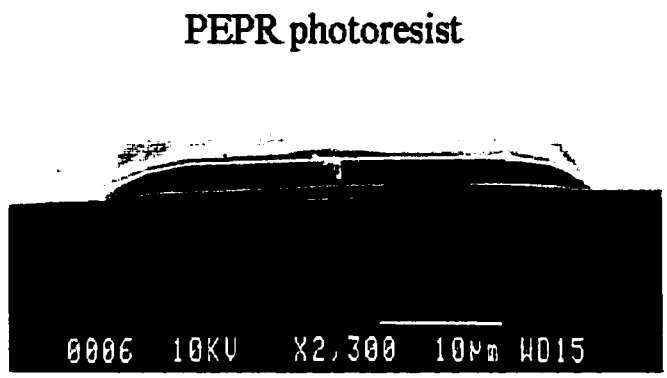

Figure 4.12: A developed PEPR line using a 2 minute softbake @ 105°C.

Shown in Figure 4.12 is a near cross-sectional view of a PEPR photoresist line that underwent a softbake of 2 minutes. Development of the pattern was achieved with a 0.2

N NaOH solution at room temperature, with a UV exposure time of 20 seconds (~ 400 mJ). While the resist is fairly smooth, its profile is quite poor. The sloping sidewalls extend on the order of six microns on either side of the line, an unexceptable amount. A similar pattern processed in an identical manner save for the fact that it underwent a five minute softbake on a hotplate held at 105°C is shown in Figure 4.13. As evidenced by the figure, sidewall sloping has been reduced to ~ 1 micron. Further investigation has suggested that a 10 minute softbake at 105°C yields excellent results. Another interesting example of the fact that the 2 minute softbake was insufficient is revealed in Figure 4.14. This sample, softbaked for 2 minutes at 105°C, was examined with an SEM. The resist began to bubble and rupture when the electron beam was focused tightly on the sample. Figure 4.14 is an SEM image of the sample upon backing off from the tight focus. The trail of bubbles originating in the center began on extremely tight focus, the square rupture delineates an entire raster area under tight focus. After rastering at that focus, the beam was backed off slightly to take the picture shown in the figure.

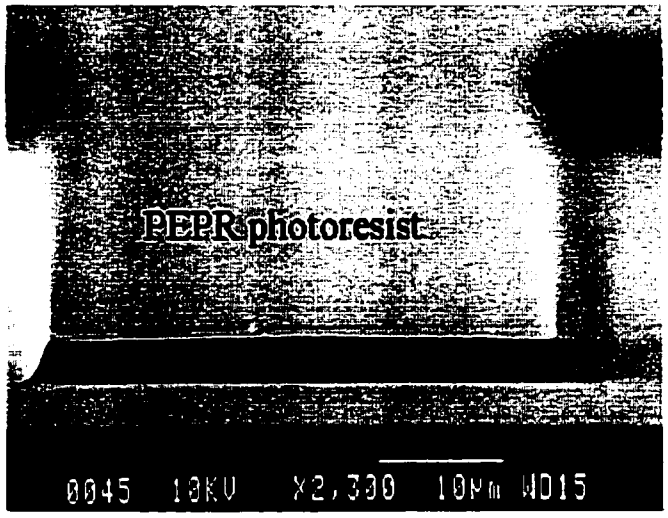

Figure 4.13: A developed PEPR line using a 5 minute softbake @ 105°C.

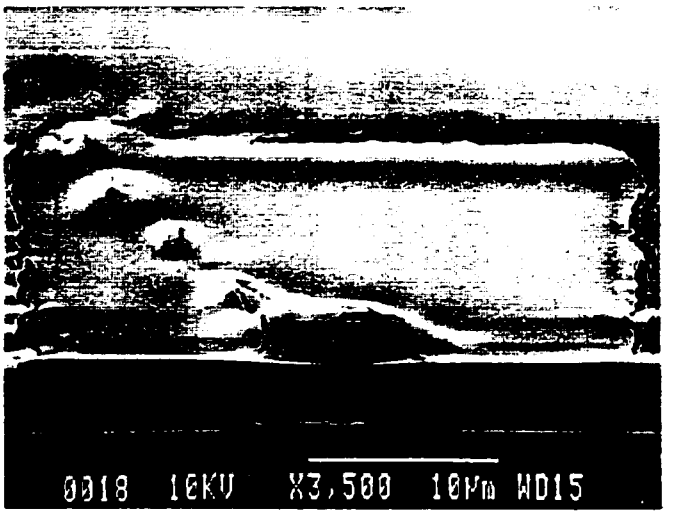

Figure 4.14: Further evidence of an insufficient softbake – damage to the resist by a scanning electron beam.

After establishing that a 10 minute softbake was desirable, an adequate developer was sought. Shown in Figure 4.15 is a short circuit FGC developed with 0.8N NaOH for approximately 1 minute. While the pattern is reasonably well defined, the developer attacked the resist aggressively around the perimeter of the pattern. In such cases, there is not much room for error in development time.

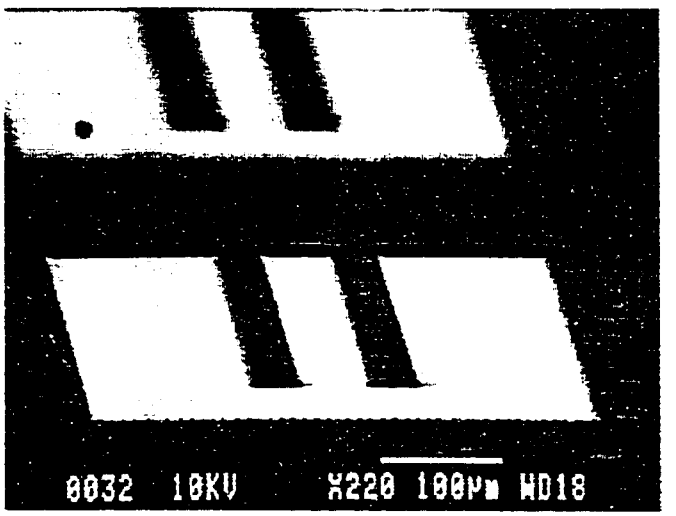

Figure 4.15: A patterned short circuit FGC using PEPR. The rough edges of the pattern are attributed to a too aggressive developer (0.8 N NaOH).

In Figure 4.16 we see a well-developed pattern, one which rivals that attained with standard resists and was achieved with a 10 minute softbake and development in 0.25N NaOH for ~ 1 minute. And finally, Figures 4.17, 4.18 and 4.19 show patterns resolved on 3D surfaces (using the same process) – all which reveal the potential of electrodepositable resist. A discussion of the ultimate resolution attainable will be discussed in section 4.8.

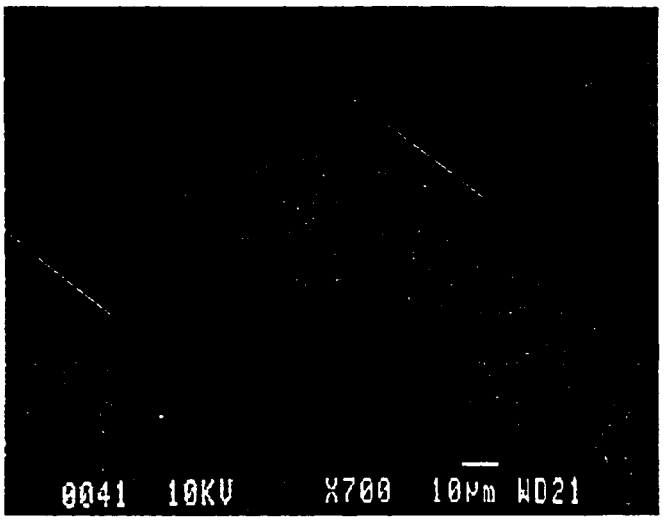

Figure 4.16: Close-up of a well-developed pattern in PEPR 2400.

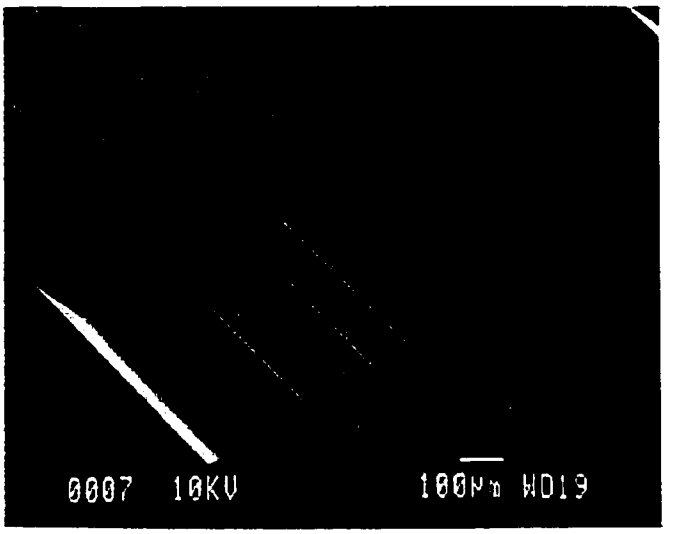

Figure 4.17: FGC line patterned into and out off a 100µm deep cavity

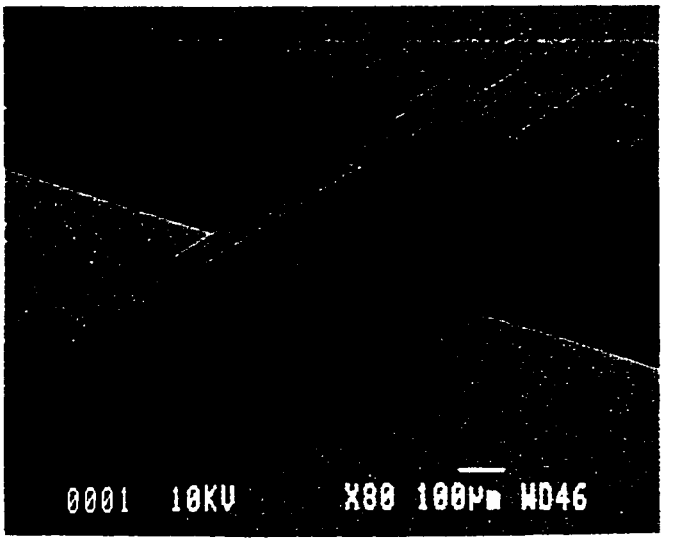

Figure 4.18: FGC line transitioning into a 300 µm deep cavity via a series of loops.

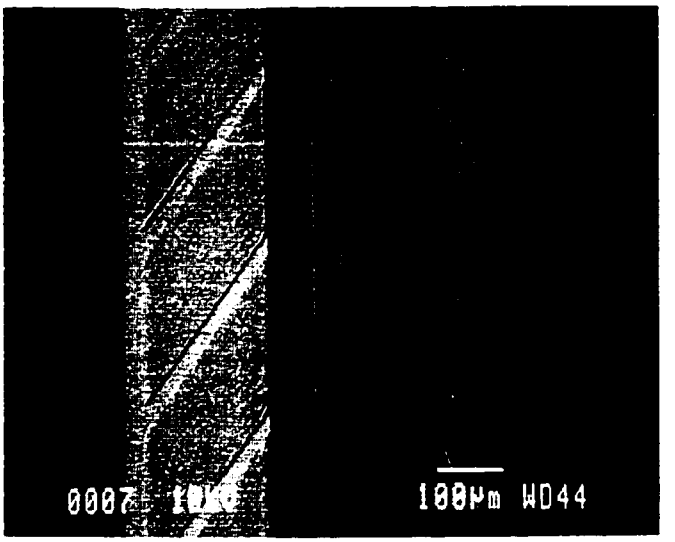

Figure 4.19: 50 µm wide lines patterned from a ledge to the bottom of a 300 µm deep micromachined cavity.

Patterning layers in photoresist allows one to subsequently pattern metal and dielectric layers that define a circuit. The patterned photoresist layer may be used to establish other layers by serving as an etch mask, a plating mold or as a liftoff mask. The most common role of the photoresist layer is perhaps that of an etch mask. In an effort to obtain

significant metal thickness (several skin depths at the operating frequency) however, metal plating is often used. Since we were seeking at the time for maximum metal thickness, the use of PEPR 2400 as a Au plating mold was initially explored.

4.7: PEPR 2400 as Au plating mold

To use PEPR 2400 as a Au plating mold, the wafer was coated with a Ti/Au/Ti (500Å/1000Å/500Å) layer which served both as a metal seed for PEPR deposition and as a seed layer for subsequent Au plating. Approximately 3 μm of PEPR was deposited and a plating mold was exposed and developed in the resist according to the results given in the previous section. The wafer was then subject to a "descum" in an O_2 plasma @ 100 W for 1 minute to remove any residual resist. To improve the strength of the resist, the sample was "hard baked" at 130°C for up to 10 minutes. The top Ti layer was then removed to expose the Au layer to be plated. The Ti layer was etched in a 10:1 mixture of deionized water and hydrofluoric acid. It should be mentioned that removing a 500Å layer of Ti typically takes only a few seconds in this manner; it was discovered that a Ti layer that had been coated with PEPR required ~ 10-15 seconds however. At this point the sample was ready for Au plating.

Au plating of such samples was found to be problematic at best. Two difficulties were encountered. First, adhesion of the resist to the underlying Ti layer was found to be of insufficient strength to withstand the rigors of Au plating. This was evidenced by the fact that often, part of the resist mold would slide off during plating as suggested in Figure 4.20 below. Another problem that was encountered was unwanted plating between the signal and ground lines (thus shorting the transmission line), often occurring at the cavity edge, and illustrated in Figure 4.21.

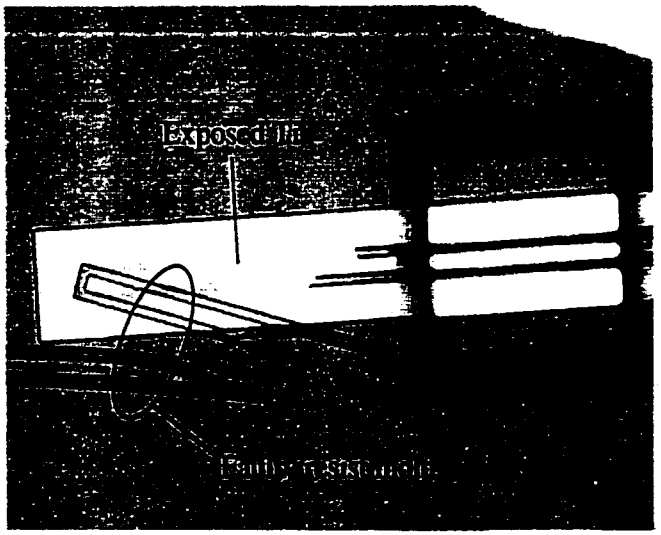

Figure 4.20: Demonstration of poor adhesion of resist to underlying Ti layer during Au plating.

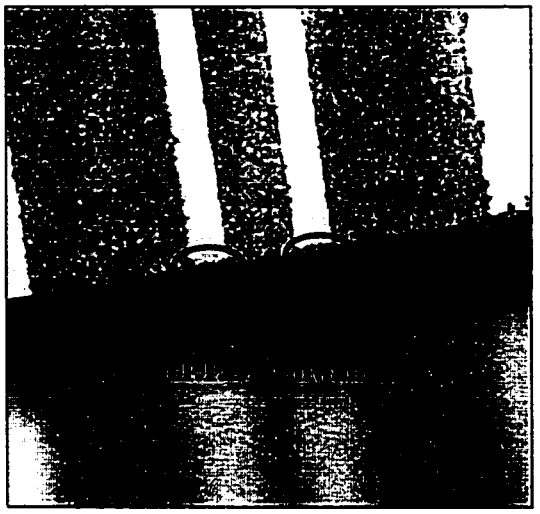

Figure 4.21: Unwanted plating between signal and ground lines causing an electrical shorting of the FGC line.

At the time of this work the author was aware of only two published accounts of the use of PEPR 2400 in the research literature. One deals with the X-ray sensitivity of the resist for use in a LIGA process [70]. In this paper no effort is made to pattern metal lines, only to pattern the photoresist. The other paper [68] does describe the use of PEPR

2400 as a plating mold. However, in this work only a single line is plated per via and is approximately 100 μm wide. Our needs are more demanding as we need multiple thin lines, closely spaced. Our experience suggesting that PEPR 2400 did not serve as a good metal-plating mold has been corroborated by a representative of Shipley [71].

As a final note here, it should be mentioned that Au, Cr and Al were also tried as plating seed layers, though none seemed to offer any improvement in adhesion. One means to solve the resist adhesion problems may lie in the use of a seed layer of Cu. It is expected that resist adhesion would be optimized in this case as the resist was designed for Cu surfaces. Investigation of alternate metal plating baths may also reveal suitable conditions for establishing PEPR 2400 as a metal plating mold.

4.8: PEPR 2400 as a liftoff mask

Many of the structures investigated in this thesis are eventually to be used at W-band and above. In light of the skin effect at these frequencies, a Au metal thickness of ~ 1μm is sufficient for most purposes (1μm Au ≈ 4 skin depths at 99 GHz). This opens the door to liftoff as a means of metal patterning. The cross-sectional profile of the resist is critically important in a liftoff procedure and both suitable and unsuitable cross-sections are suggested below in Figure 4.22.

The liftoff procedure calls for the development of a pattern in the photoresist. A metal layer is then evaporated over the entire sample, after which the sample is immersed in a solvent to remove the resist mold and "liftoff" the unwanted metal. Ideally, the only metal that should remain on the sample after liftoff is that which was deposited in the areas in which no photoresist existed immediately prior to evaporation. In the liftoff process it is important that the resist has a cross-section such that the evaporated metal

does not make a continuous film lest it be difficult to liftoff where desired. The left hand drawing in Figure 4.22 depicts a resist with a profile for which liftoff is nearly impossible (see Figure 4.12 as well). In such a situation, the solvent is unable to find access to remove the resist and liftoff the metal that was deposited upon it.

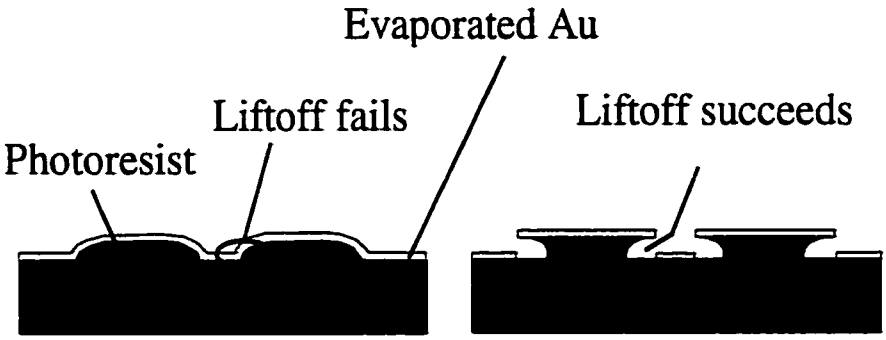

Figure 4.22: Resist profiles and lift-off success.

Contrast this situation with that depicted on the right hand side of Figure 4.22. Here the resist profile is such that the evaporated metal (which deposits in a "line-of-sight" fashion) is no longer continuous, allowing solvent to attack the resist and liftoff the unwanted areas of metal. The question arises as to how we can obtain the resist profile with PEPR 2400 to make liftoff a possibility.

A solution has emerged which makes use of the rather poor adhesion between PEPR 2400 and the Ti seed upon which it is deposited. (Though unknown at the time of the development of this process, a similar process developed for another ED resist has been reported in [72].) By avoiding a softbake on a hotplate and rather submitting the PEPR 2400-coated sample to a vacuum dry, it is possible to remove the solvent content of the resist without fostering improved adhesion between the resist and the metal seed. A 1.5 hour vacuum dry (base pressure 1×10^{-6} torr) was found to be sufficient for this purpose.

After vacuum drying the sample is exposed in typical fashion, the development procedure is somewhat altered however and requires careful supervision. Whereas the development of a pattern in soft-baked PEPR 2400 (10 minutes @ 105°C) takes approximately 1 minute or more, vacuum-dried PEPR 2400 develops in ~ 10 seconds and will be completely lifted off the wafer (and thus unusable) in about 40 seconds. For successful development of the resist effecting a profile that will make subsequent metal liftoff possible, the resist is slightly overdeveloped (typical development time ~ 15-20 seconds). After development, the sample is subjected to an O_2 plasma "descum" at 150W for 2 minutes to remove residual resist.

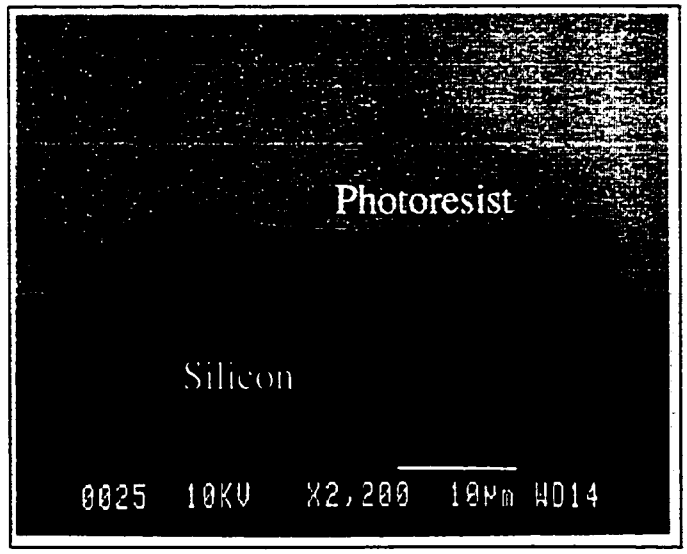

Figure 4.23: Scanning electron micrograph of PEPR 2400 ready for metal evaporation in a metal liftoff process.

A scanning electron micrograph of a line of resist having undergone vacuum drying and development (but not the descum) is shown in Figure 4.23. Clearly evident in the figure is the desired lifting of the resist edges that will permit subsequent metal liftoff. The figure also alludes to the fact that the entire resist could be undercut if the

development is not closely monitored. Figure 4.24 displays another sample with PEPR 2400, this time having undergone full treatment to develop a metal liftoff mold (including the descum step). We find a nice clean pattern waiting to undergo metal evaporation.

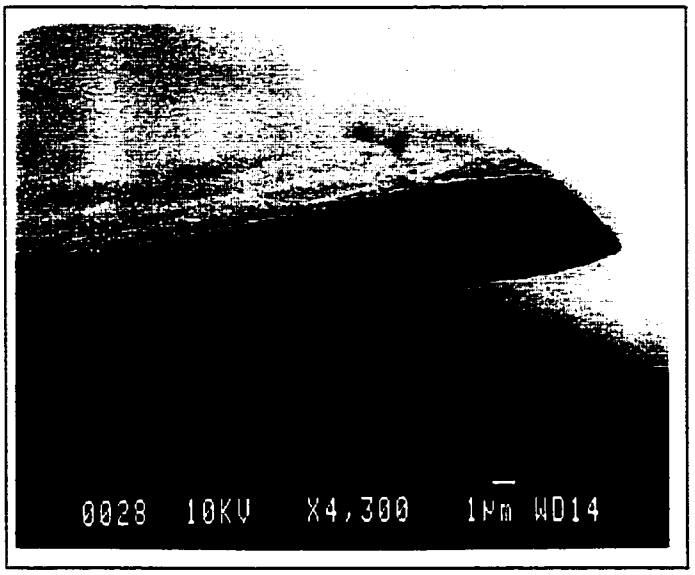

Figure 4.24: Scanning electron micrograph PEPR 2400 ready for metal evaporation in a metal liftoff process.

4.9: Diffraction Effects During Resist Exposure

In contact printing of patterns in photoresist, the mask is in intimate contact with the photoresist. This is clearly not possible when simultaneously exposing patterns on several surfaces of micromachined silicon. While the mask will indeed be in contact with the top surface of the micromachined silicon wafer, a considerable gap (up to 300 μm for the sample depicted in Figures 4.16 and 4.17 for instance) will exist between the mask and the cavity sidewalls and bottom. When exposing a pattern not in intimate contact with the mask, a certain amount of resolution will be lost due to the effects of diffration. A schematic drawing of the situation is given in Figure 4.25.

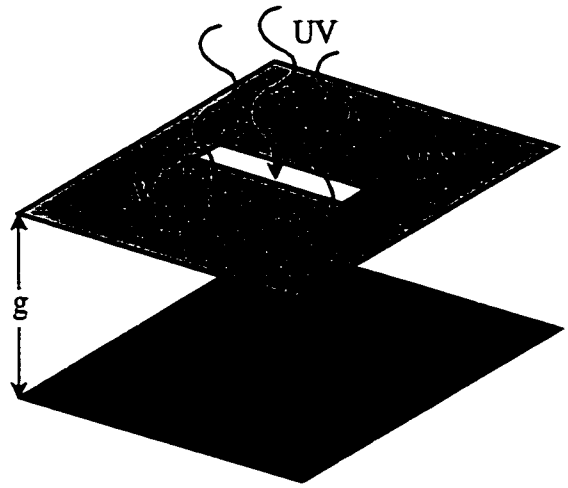

Figure 4.25: Schematic diagram illustrating a separation between a mask and the imaging plane.

In the figure, a mask with a slit of width W is separated from the imaging plane by a distance g. A pattern of the slit is to be reproduced on the imaging plane and to do so, the mask is illuminated with ultraviolet radiation of wavelength λ. The primary exposure wavelength of the mask aligner used during the work reported here is ~ 405 nm (0.405 μm). The minimum slit width (W) used in any mask was ~50 μm and the mask/image plane separation distance (g) typically fell between 0 μm (for the top wafer surface) and 400 μm for the depth of a cavity. The situation is governed by Fresnel diffraction if the following inequalities are true:

$$\lambda << g < \frac{W^2}{\lambda} .$$

In the lower limit of near field diffraction, the minimum linewidth may be approximated by the following equation [68],[73]:

$$\text{resolution} \sim \sqrt{\lambda g} .$$

Ideally then, for a 400 μm separation between the mask and the imaging plane and an exposure wavelength of 0.405 μm, one could expect no better than a minimum linewidth of approximately 13 μm. Care must be taken in defining attainable resolution as the above formulation does not take into account the effects of a non-ideal illumination source, light absorption in the resist [74] nor the effects of developing. Far better is it to experimentally determine the limitation for a given application.

4.10: Summary

The development of a fabrication process to establish metal patterns on the various facets of anisotropically etched (001) silicon is detailed in this chapter. A thorough study of the yield that characterizes such a process is needed to assess its application to large-scale manufacturing. While the use of PEPR 2400 as a plating mold was not successfully achieved in this work, such a process would be desirable to realize metalization thickness of several skin depths at frequencies in the low gigahertz range. Modification of the resist deposition conditions and an investigation of other metal plating processes may prove key to developing such a process. In chapter 5, the fabrication process detailed in this chapter is utilized to develop a novel transmission line structure suitable for a variety of electronic packaging applications.

CHAPTER 5

SILICON MICROMACHINED MULTILEVEL AND MULTILAYER TRANSITIONS FOR HIGH FREQUENCY APPLICATIONS

5.1: Introduction

One of the limiting elements of many microwave and millimeter wave systems is the package used to connect the system to the outside world and as such the issue of packaging has received significant attention in recent years [75]. Diverse issues such as electromagnetic isolation, heat dissipation, and mechanical stability are important considerations in designing electronic packages. Silicon micromachining has been proposed as a potential solution to the dilemma posed by the drive toward increasing circuit density while reducing system cost. In its favor, silicon has good mechanical [76] and thermal [77] properties and is capable of supporting high-performance microwave and millimeter wave circuitry in a cost-effective manner. By micromachining silicon using the techniques described in chapter 2, it is possible to extend the capabilities of silicon in ways that offer potential solutions to some of today's packaging efforts.

For instance, the need to isolate RF-MEM (microelectromechanical) switches from humidity-driven effects such as stiction [78] may be addressed by silicon micromachining techniques. In this chapter, the initial efforts at developing transmission lines that provide access to the top surface and the depths of a silicon micromachined

wafer are described. The logical extension of this work is the development of a novel class of multiple-wafer vertical transitions and RF-MEM switch packaging architectures.

5.2: Multilevel Finite Ground Transmission Lines

One packaging architecture of interest is depicted in Figure 5.1. In the figure, a flip chip (an amplifier circuit for instance) is bonded in a micromachined cavity. RF and DC access to the chip are provided by transmission lines that are patterned on the top wafer surface, the cavity sidewalls and the depths of the cavity. To do so in a consistent manner requires the ability to simultaneously pattern features on the various facets of the micromachined substrate. The technique of electrodeposition of photoresist as described in the previous chapter, seems ideally suited to such an application. To complete the packaging of the flip chip of Figure 1, a capping wafer could be added.

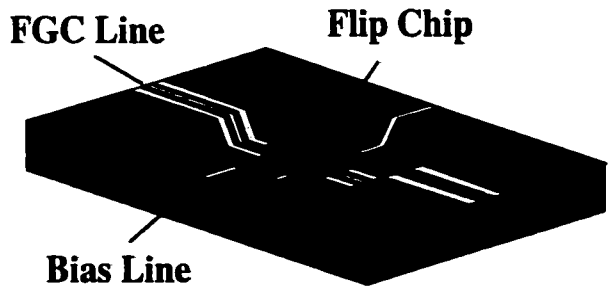

Figure 5.1: A packaging architecture relying on the ability to simultaneously pattern features on the various facets of micromachined silicon.

A test structure used to examine such an architecture is suggested in Figure 5.2. Fabrication of the structure consisted of wet anisotropic etching of (001) silicon in TMAH, electrodeposition of PEPR 2400, and metal liftoff (1000Å Ti/ 1 μm Au). The details of anisotropic etching and patterning with PEPR 2400 may be found in chapter 2

and chapter 4 respectively. Figure 5.3 shows a scanning electron image of a transition revealing some key features of the realized structure.

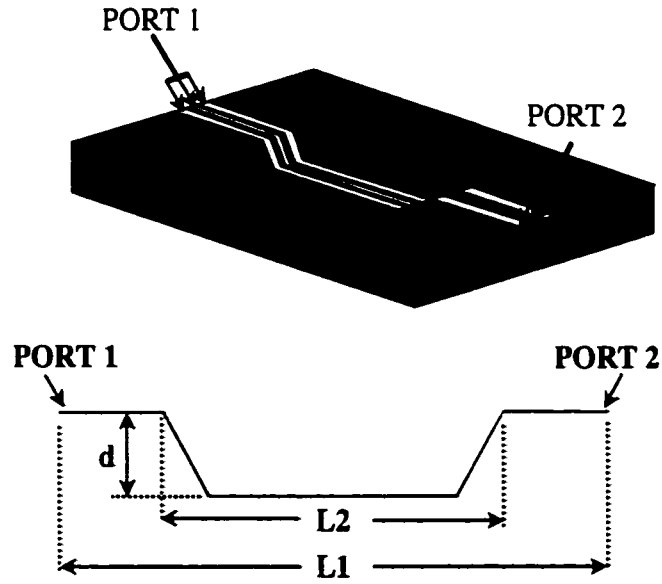

Figure 5.2: Schematic representation of the multilevel test structure.

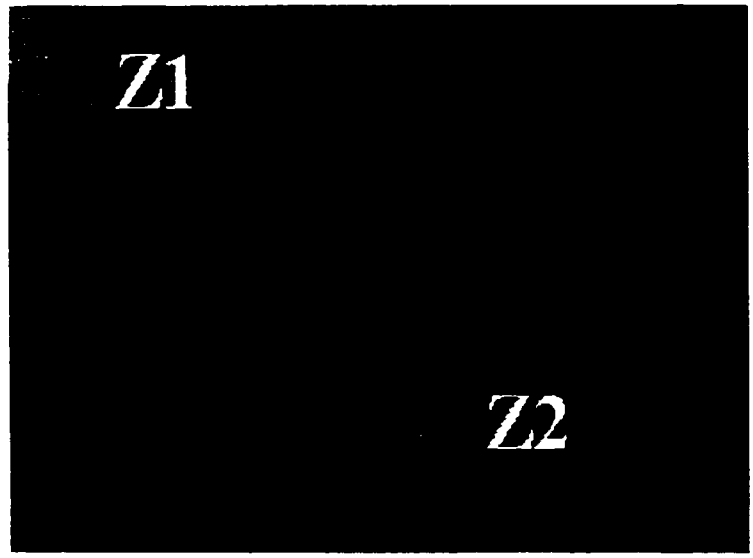

Figure 5.3: SEM image of an FGC multilevel transition. The line of impedance Z1 is printed on the top surface of the wafer and that of impedance Z2 is realized in the bottom of a micromachined cavity (110 μm deep in this case).

Figure 5.3 reveals that the fabricated FGC line is not perfectly uniform along its length. The lengths of transmission line patterned on the top surface were measured to have center conductor, slot, and ground plane widths of 92 μm, 72 μm and 140 μm (92/72/140) respectively. As described in chapter 4, diffraction of UV light occurs during the pattern exposure step due to the gap (110 μm in this case) that exists between the mask and the bottom of the micromachined cavity. This unwanted diffraction tends to smear patterns, and transmission lines of dimensions 104/58/156 were resolved on the bottom surface of the cavities. Bulging of the transmission line is visible at the intersection of the cavity surface and the slanting sidewall and is an artifact of increased resist thickness at such locations (see Figure 4.7), the resist drying procedure, and diffraction. The dimensions of such section were measured to be approximately 125/35/178.

The impedance of each of these sections of transmission line was estimated using IE3D and found to be 59 Ω (92/72/140), 53 Ω (104/58/156) and 44 Ω (125/35/178) respectively. Due to this mismatch in impedance, it was anticipated that a standing wave pattern would be evident in the measured results. Indeed, such a pattern can be seen in the measured return loss given in Figure 5.4. The measurements were performed using an HP8510C network analyzer and a set of 40A picoprobes with on-wafer calibration made possible through a TRL protocol (see section 3.2). The measured structure is that depicted in Figure 5.2 with L1 = 8 mm (after de-embedding), L2 = 5 mm, and d = 110 μm. In addition to the measured data, Figure 5.4 includes the s-parameters of a LIBRA-based model.

The LIBRA model broke the structure up into sections of transmission line of impedance Z1=59 Ω and Z2= 55Ω (see Figure 5.3), corresponding to the impedance of the sections of line on the top and bottom surfaces. Due to their small length, the bulging sections with impedance of 44 Ω were ignored in this simplified model, though perhaps their effects start to be felt at the highest frequencies tested. In the LIBRA model, each section of transmission line was given the appropriate impedance (from IE3D), length (measured), effective dielectric constant (IE3D) and attenuation (measured). The attenuation of each segment was estimated using the measured attenuation at 20 GHz (as determined with MultiCal [58]) of the 92/72/140 line. An illustration of the LIBRA model is given in Figure 5.5.

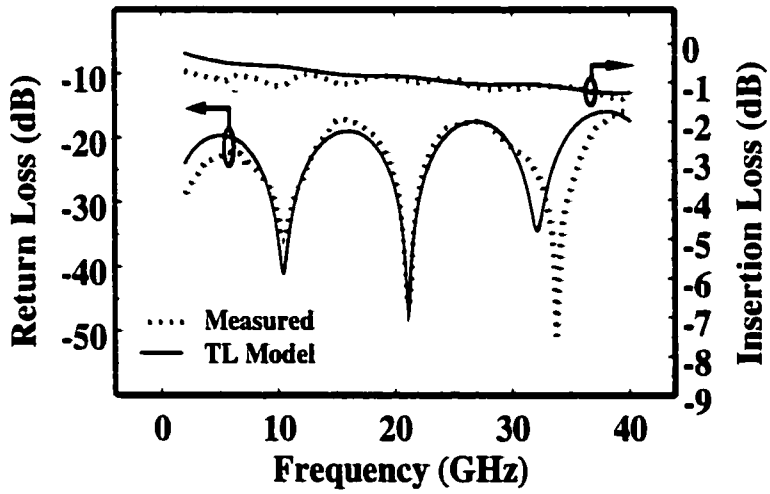

Figure 5.4: Measured and modeled results of a back-to-back multilevel FGC transition.

Since the measured results were calibrated with an on-wafer protocol to the 59 Ω transmission line sections (the top sections – those that were physically probed), the port impedance in the LIBRA model was set to 59 Ω. The lengths of the sections were taken to be (L1-L2)/2 for the Z1 sections and L2 for the Z2 section. In fact the L2 section of

the actual structure was somewhat less owing to the sloping sidewalls of the cavity. Again, the bulging sections were ignored. Parasitic capacitance that exists at the bending sections of line was modeled with shunt capacitors. The capacitor value (0.0111 pF) was that obtained by matching the first null in the modeled return loss with that of the measured data through an optimization routine in LIBRA.

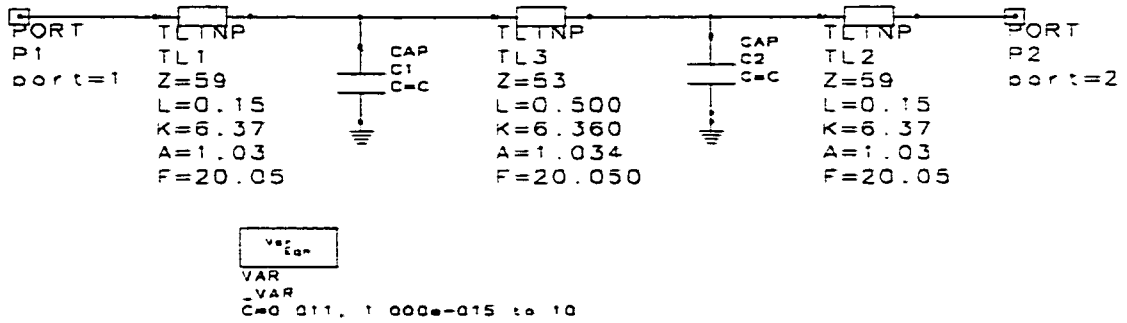

Figure 5.5: LIBRA model of the back-to-back multilevel transition. The port impedances were set to 59 Ω.

Good agreement between the measured and modeled results extend throughout most of the 2-40 GHz measurement band with some breakdown in the model beginning to occur near 30 GHz. Such departure between measured and modeled results at the high frequency end seems likely due to the simple circuit model used. A more accurate accounting of the actual lengths of the sections and inclusion of the bulging sections seem necessary to precisely model the transition near 40 GHz.

The insertion loss of a back-to-back transition was compared to that of a planar line of equal horizontal extent. Specifically the planar line was 8 mm long and the back-to-back transition slightly longer (8.156 mm) due to the sloping cavity sidewalls. An average loss of less than 0.08 dB per transition was measured with a maximum loss of approximately

0.17 dB in the 2-40 GHz range. The average and maximum values are based on measurement of five identical test structures.

One potential extension of this work could come in the form of through-wafer vertical transitions as suggested in Figure 5.6. Herrick et al. [79] have investigated a three-via vertical interconnect using 90 μm thick micromachined silicon. In this work, they report an impressive minimum loss per transition of 0.6 dB (at 90 GHz), which when scaled scaled to 30 GHz, is expected to exhibit an insertion loss of less than 0.2 dB. The transition reported here compares favorably to the three-via transition in several ways.

The measured loss per transition of the single-via structure described above exhibits an average loss of only 0.08 dB per transition across the 2-40 GHz band, requiring neither the quarter-wavelength stub nor the capacitive airbridge found in the three-via transition. Even a modest decrease in insertion loss per transition would pay dividends when considering the many transitions need on a given MMIC. In addition, the single-via transition detailed in this chapter is more compact than the three via interconnect with multiple transitions per via possible. These advantages are only potential as further work is necessary to extend the multilevel transition to a thru-wafer vertical interconnect.

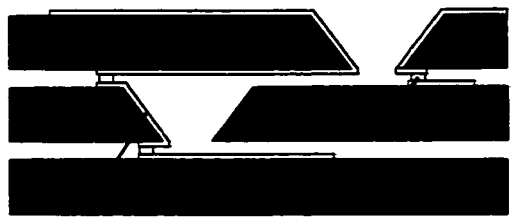

Figure 5.6: Schematic representation of single-via vertical transitions micromachined through multiple silicon wafers.

It is worthy to note some work presently being investigated at Michigan which combines the multilevel transition with a three-via interconnect. The idea behind this

effort is to provide a hermetic package for an RF-MEM switches. In such a scheme, the switch is to be accessed through a combination of a multilevel transition (100 μm deep) with a 100 μm deep three-via vertical interconnect. In this manner both rf and dc is made available to a switch that is established on the opposite side of the wafer. The switch is to be surrounded by a gold-plated rectangle; a similar rectangular pattern is developed on a capping wafer that is to be bonded to the wafer carrying the switch. In such a manner a hermetic seal is to be provided [80].

5.3: Simulation of a DRIE Three-Via Interconnect

Chapter 2 discussed the use of DRIE for silicon micromachining. Part of the attraction of the DRIE process stems from the fact that etching is no longer crystal-orientation dependent, thus allowing a variety of shapes to be realized. Another attractive feature of DRIE is that it is a dry process requiring only a simple photoresist mask. It seems that these features could be exploited in both the multilevel transition/three-via switch package and perhaps in a compact three-via transition.

One potential process flow for developing a three-via deep-etched vertical transition is given in Figure 5.7. In the first step, a Ti metalization (step *a*) is deposited on the top surface. Apertures are opened in the Ti layer (step *b*) to be used as windows for subsequent deep etching. In step *c*, FGC lines are patterned on the top surface. In step *d*, deep-etched vias originating from the top surface are developed to act as backside alignment keys. Backside IR alignment could be used instead. In step (e), the three-via interconnect is etched and terminates at the bottom of the top layer metalization. Step (f) illustrates the finished product – a metalization has been sputtered and defined photolithographically on the wafer bottom.

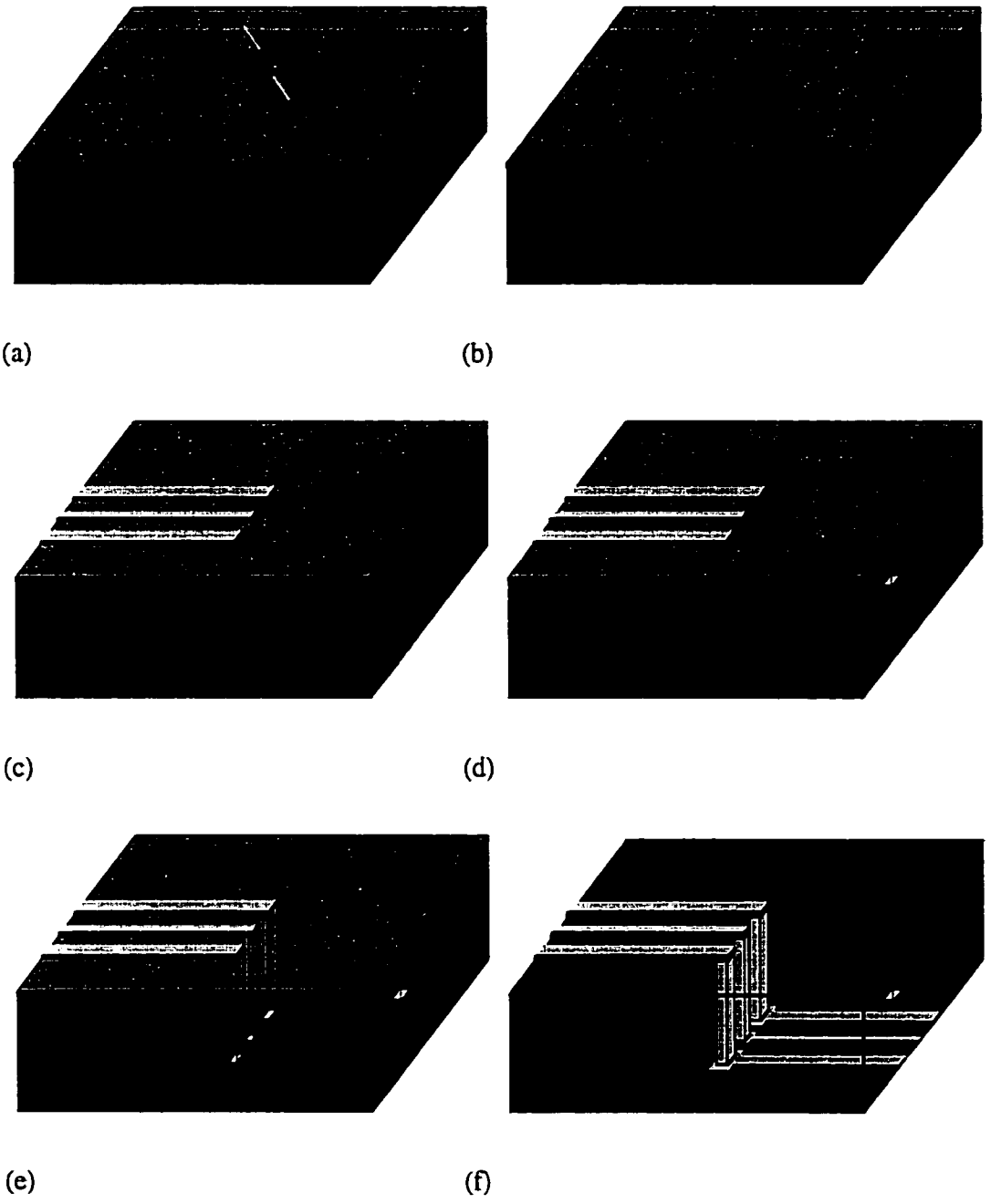

Figure 5.7: A proposed process flow for a deep-etched thru-wafer interconnect.

Finally, since there are no micromachined apertures on the top layer, defining additional metalization and/or dielectric layers on the top surface should be straightforward. Even if deep etching is done after developing the circuitry on the top surface, since the etching is

a dry process and is masked by photoresist, the circuitry should be easily protected which may not be the case with anisotropic etching.

To begin to evaluate the electromagnetic behavior of the transition, initial IE3D simulation results are included. The first structure to be simulated resembles that of Figure 5.7f with Figure 5.8 revealing its precise dimensions. Simulation results of this structure are given in Figure 5.9 from which it appears that the transition performs reasonable well up to a few GHz whereupon the amount of signal transmitted begins to steadily drop. To better understand the transition a simple LIBRA-based model was constructed.

In the model, the feed lines (60/40/130) are represented by their 51 Ω impedance. The three-via combination is treated as a separate 200 μm long transmission line. The impedance of this section was determined with MAWELL 2D and found to be roughly 28 Ω. The impedance of this section in considerably lower than that of the feed lines as the via is imbedded in silicon thus increasing the line capacitance. The effective dielectric constant of this section is that of silicon, 11.7.

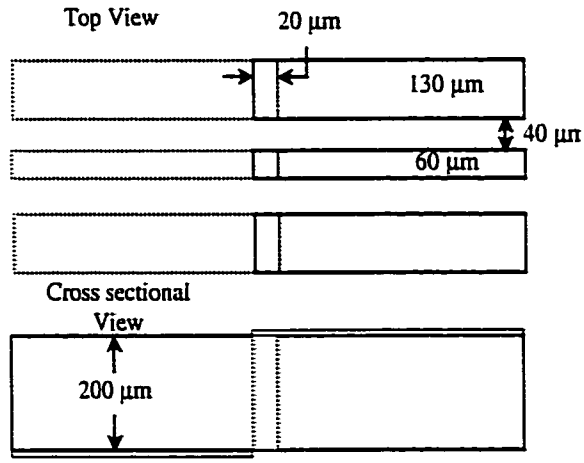

Figure 5.8: Schematic representation of a deep-etched thru-wafer interconnect.

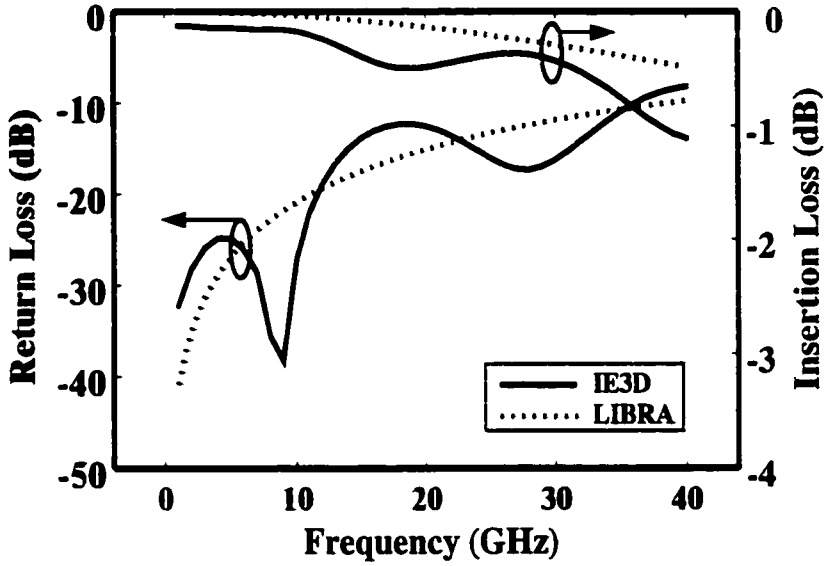

Figure 5.9: Simulated performance of a deep-etched three-via thru-wafer interconnect.

Since the IE3D model assumed perfect conductors, ideal transmission lines were used in the LIBRA model. With such an element, one is required to enter the line's impedance and electrical length at a given frequency. The 28 Ω via has an electrical length of 0.82° at 1 GHz. Since the via is electrically small in length at 1 GHz, the effects of its lower impedance are not felt. The increase in return loss as frequency increases is due in part to the increasing electrical length of the via, thus making the impedance mismatch between feed line and via more important. Naturally, parasitic reactive elements also play a significant role in the transition's performance. It was felt that if the impedance of the via could be set to that of the feed lines, the return loss would be greatly reduced. Using MAXWELL 2D the dimensions of a near 50 Ω (actually 46.5 Ω) via were established. Back-to-back DRIE-via transitions with the appropriate dimensions were simulated with the results given in Figure 5.10. The design included tapering of the FGC lines to the vias.

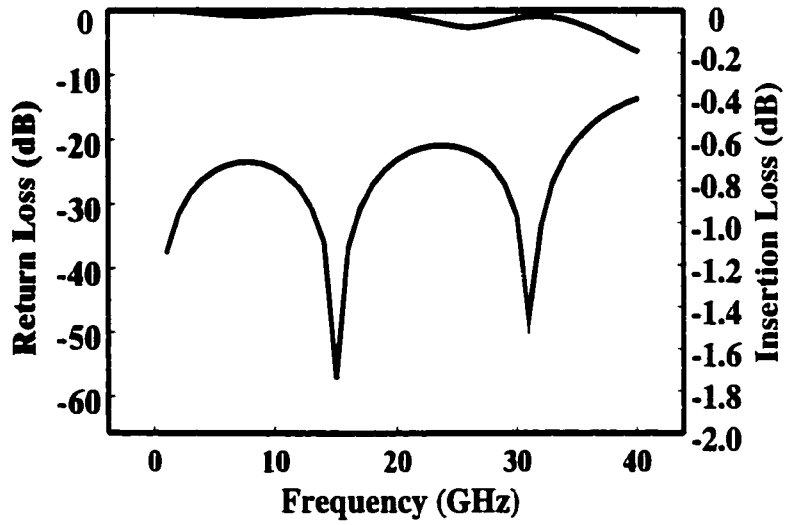

Figure 5.10: Simulated performance of an improved version of a deep-etched three-via thru-wafer interconnect. The results are for back-to-back transitions.

A comparison between Figure 5.9 and Figure 5.10 shows a clear improvement in the transition performance. A loss of about 0.1 dB per transition exists at 40 GHz in the improved design. Further modeling including an accurate accounting of both conductive and radiation loss as well as fabrication and testing are necessary to allow definitive analysis of deep-etched transition and to arrive at an optimum design.

As a final note, even if radiation loss becomes a problem in the deep-etched transition, a variety of means may be explored to mitigate the effect. One rather novel means may be to include deep-etched holes around the via to help suppress surface waves. In short, with further investigation the deep-etched thru-wafer interconnect may prove an attractive alternative to the wet-etched three-via interconnect.

CHAPTER 6

MICROMACHINED WAVEGUIDES

6.1: Introduction

The attractive signal transfer properties of hollow metal waveguides as well as the difficulties of manufacturing precise waveguides at THz frequencies were described in chapter 2. A variety of micromachining techniques have been investigated over recent years to alleviate these manufacturing difficulties. In this chapter the properties of three "micromachinable" waveguides are investigated. Two of the guides are realizable through wet anisotropic etching of (001) silicon and are defined by {111} planes, with the third of rectangular cross section made possible with DRIE. Measured results of an anisotropically etched silicon diamond waveguide for operation at W-band is given.

6.2: Silicon Micromachined Waveguide Geometries

Three waveguide cross sections that are realizable through silicon micromachining are displayed in Figure 6.1. The rectangular waveguide may be formed through DRIE of silicon or through wet anisotropic etching of (110) oriented silicon as in [11]. Both the silicon diamond waveguide and the silicon hexagonal waveguide evolve quite naturally from the {111} crystal planes of anisotropically etched (001) silicon. The propagation

characteristics, demonstrating the dominant mode cutoff frequency of each waveguide, are given in Figure 6.2.

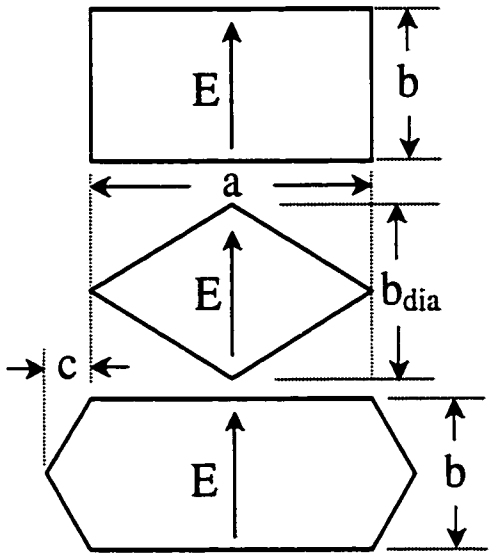

Figure 6.1: Cross sections of three waveguides realizable via silicon micro-machining: rectangular waveguide, silicon diamond waveguide and silicon hexagonal waveguide.

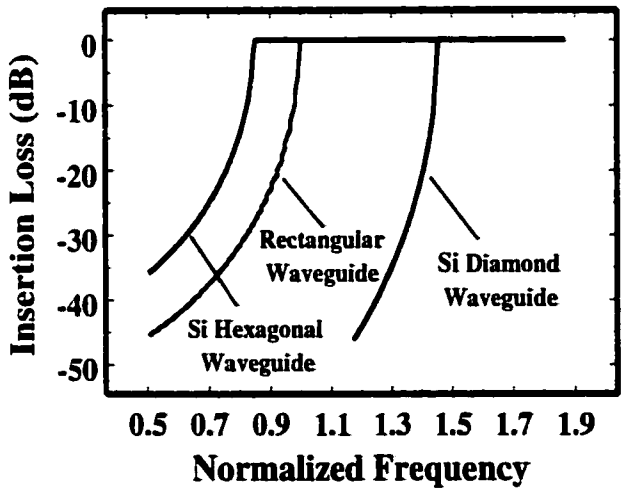

Figure 6.2: The propagation characteristic of three waveguides of differing cross section.

Figure 6.2 is based on each waveguide sharing the same broad wall dimension *a*. Furthermore, the rectangular waveguide and the silicon hexagonal waveguide have the

same height, *b*. The *c* and b_{dia} dimensions of the silicon hexagonal and diamond waveguides are based on the sloping {111} planes of crystalline silicon and are thus defined as $c = b/\left(2\sqrt{2}\right)$ and $b_{dia} = a/\sqrt{2}$. In the figure, the insertion loss of each guide is plotted against a normalized frequency, given as the ratio of the frequency to that of the cutoff frequency of the rectangular waveguide.

From the figure, it is clear that for given *a* and *b* dimensions, the cutoff frequency of the silicon hexagonal guide is roughly 0.85 that of the rectangular waveguide with the cutoff frequency of the silicon diamond waveguide pushed considerably past that of the other two. Differences in the cutoff frequency are of course a result of the variations in cross section. By properly modifying the dimensions of the hexagonal and diamond guides, their cutoff frequencies may be matched to that of a given rectangular guide. More important than the absolute value of the waveguide's cutoff frequency however is the guide's single-mode bandwidth. The single-mode bandwidth of the standard rectangular waveguide (a=2b) is 2:1, that of the silicon hexagonal waveguide is nearly 2:1 and that of the diamond waveguide roughly 1.33:1.

Analytical expressions for the defining parameters of the rectangular waveguide and the silicon diamond waveguide will be given below. Due to the failure to establish a viable transition from a planar line to the silicon hexagonal waveguide (see Chapter 7), we omit any further discussion of this waveguide.

6.2.1: Rectangular Waveguide

The most typical hollow metal waveguide is of rectangular cross section. The characteristics of rectangular waveguide are well understood and are conveniently defined analytically. Signal propagation is carried through transverse electrical (TE)

and/or transverse magnetic (TM) modes in accord with the cross sectional dimensions of the waveguide (see Figure 6.1) and the operating frequency. The cutoff frequencies of the infinite possible TE modes and TM modes are given as follows:

$$f_{c_{m,n}} = \frac{1}{2\pi\sqrt{\mu\varepsilon}}\sqrt{\left(\frac{m\pi}{a}\right)^2+\left(\frac{n\pi}{b}\right)^2}\,.$$

For TE modes, m and n may take on any integer value whereas TM modes are only defined for nonzero values of m and n. We will focus exclusively on rectangular waveguides with a = 2b, filled by vacuum ($\mu=\mu_o$ and $\varepsilon=\varepsilon_o$). Furthermore we will restrict the waveguide to frequencies of single mode operation. In such a case, the cutoff frequency of the single propagating mode is that of the dominant TE_{10} mode, and given by the following:

$$f_{c_{1,0}} = \frac{c}{2a}\,.$$

Dropping the subscript for simplicity in notation, the propagation constant, guided wavelength, phase velocity and wave impedance of the dominant mode are as follows:

$$\beta = \sqrt{k^2-\left(\frac{\pi}{a}\right)^2}\,,$$

$$\lambda_g = \frac{2\pi}{\beta}\,,$$

$$v_p = \frac{\omega}{\beta}\,,$$

and,

$$Z_{TE} = \frac{k}{\beta}\eta .$$

In the above equations the wavenumber (free-space), k, and the intrinsic impedance of free space, η are given as follows:

$$k = \frac{2\pi f}{c},$$

and,

$$\eta = 120\pi .$$

In addition to the wave impedance, Z_{TE}, impedance expressions based on power and current, power and voltage and voltage and current may be defined as follows for a rectangular waveguide [81]:

$$Z_{pi} = Z_{TE}\frac{\pi^2 b}{8a} \qquad [6.1]$$

$$Z_{pv} = Z_{TE}\frac{2b}{a} \qquad [6.2]$$

$$Z_{vi} = Z_{TE}\frac{\pi b}{2a} \qquad [6.3]$$

The availability of analytical expressions for the various parameters of the waveguides presented in this study may aid in modeling waveguide behavior in terms of transmission lines. For this reason, similar expressions for the silicon diamond waveguide will be given in the following section.

6.2.2: Silicon Diamond Waveguide

In expressing the governing equations of the diamond waveguide it is helpful to define a factor c_f, which is simply the ratio of the cutoff frequency of the dominant mode in a

rectangular guide of broad wall dimension a to that of a diamond guide of corresponding dimension a. (See Figure 6.1). That is,

$$c_f = \frac{f_{c,rect}}{f_{c,diamond}} \approx 0.685 .$$

The numerical value of 0.685 was determined through the results of full-wave simulation using HFSS. The cutoff frequency, propagation constant and wave impedance of the dominant mode of the silicon diamond guide may then be expressed as follows.

$$f_{c,diamond} = \frac{c}{2ac_f} ,$$

$$\beta_{Diamond} = \sqrt{k^2 - \left(\frac{\pi}{ac_f}\right)^2} ,$$

$$Z_{Diamond} = \frac{k}{\beta_{Diamond}} \eta ,$$

and,

$$Z_{Diamond} = \eta \left[1 - \left(\frac{f_{c,Diamond}}{f} \right)^2 \right]^{-1/2} .$$

HFSS simulation has demonstrated that the dominant mode is TE in nature and thus the dominant-mode impedance is that of a TE mode. (See [81] for additional details on the modes of the diamond waveguide.) The phase constant of a W-band diamond waveguide (a = 2.540 mm) as determined with HFSS, along with a curve computed using the corresponding equation, are given in Figure 6.3. The analytical curve and full-wave simulation results agree within 1% over most of the frequency range suggesting the accuracy of the analytical expression.

The impedance equations [6.1] through [6.3] of the rectangular waveguide are all simply the wave impedance of the guide multiplied by a constant that depends on the a and b dimensions. It is expected that similar expressions should be available for the silicon diamond waveguide. In the case of the diamond waveguide, the b_{dia} dimension is set by selection of the a dimension and as a result, no independent control of these two dimensions is possible. For this reason, the impedance expressions for the silicon diamond waveguide may be expressed without reference to the cross sectional dimensions. (The effects of the diamond's dimensions are of course felt in the waveguide's wave impedance.) The impedance expressions for the silicon diamond waveguide are given as follows:

$$Z_{Diamond,pi} = 0.482 Z_{Diamond} \qquad [6.4]$$

$$Z_{Diamond,pv} = 1.25 Z_{Diamond} \qquad [6.5]$$

$$Z_{Diamond,vi} = 1.292 Z_{Diamond} \qquad [6.6]$$

As an example of the accuracy of the impedance equations, Figure 6.4, displays the voltage-current impedance as determined with equation [6.6] along with the corresponding full-wave simulation results (HFSS). The agreement between the simulated and calculated impedance values is within 1% throughout most of the single-mode frequency range of the waveguide. Similar agreement exists between HFSS and the corresponding analytical equations for $Z_{Diamond,pi}$ and $Z_{Diamond,pv}$. This is true for two reasons. First, the expression for the wave impedance of the diamond waveguide (TE mode) gives the proper form to the impedance curves and second, the scaling factors were selected such that each analytical curve matched that of HFSS at 110 GHz. The

impedance equations [6.1] through [6.6] may be used in circuit modeling of the diamond waveguide as outlined in Appendix E.

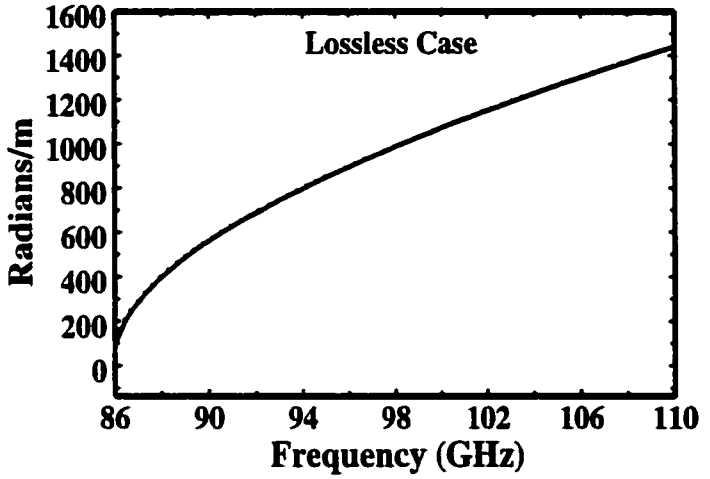

Figure 6.3: Phase constant of a W-band silicon diamond waveguide (a=2.540 mm) – both full-wave and analytical results are given.

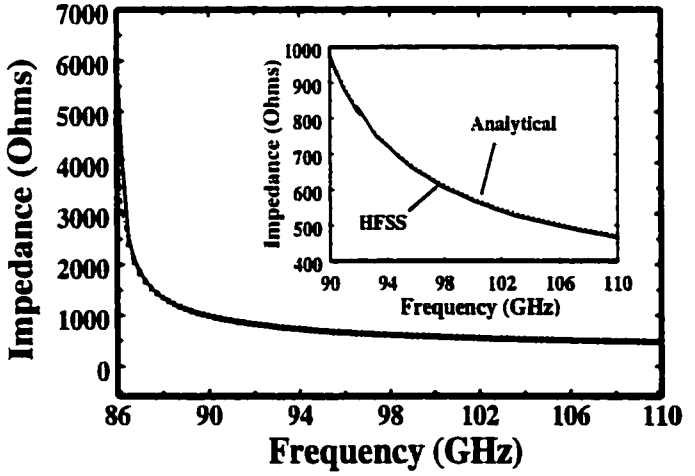

Figure 6.4: Voltage-Current impedance (Zvi) of a diamond waveguide with a = 2.54 mm.

6.3: Measured and Modeled Performance of the Si Diamond Waveguide

6.3.1: Measured results

Initial work in fabricating and testing micromachined waveguides has been carried out. Each waveguide was formed in a split-block manner in which the two halves of the waveguide were anisotropically wet etched in TMAH. The pieces of micromachined silicon (2mm thick) were then diced, cleaned in a "piranha" etch, metalized (Ti/Au – 750 Å /1.1 μm) through sputter deposition and bonded using an Electronic Visions bonder.

The top and bottom halves of the waveguide were aligned using etched pits and glass spheres. Increased undercut due to changing solution concentrations caused the pits in the tested samples to be somewhat larger than expected. Due to the enlarged alignment pits, some misalignment of the top and bottom halves was experienced. Figures 6.5 shows a scanning electron micrograph image of the cross section of a bonded diamond

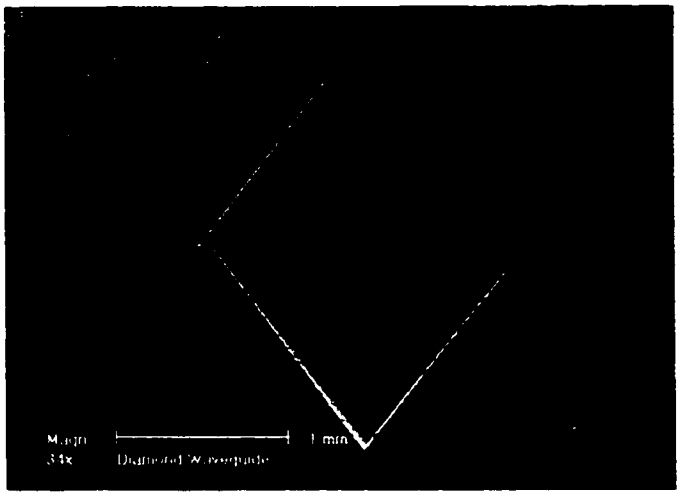

Figure 6.5: SEM of the cross section of a bonded silicon diamond waveguide. The 64 μm lateral offset between the upper and lower halves is a result of enlarged alignment pits.

waveguide – roughly 64 μm of misalignment exist between the two portions of the waveguide. The measured results presented later in this chapter are for a waveguide with a misalignment of less than 10 μm. Near perfect alignment is anticipated in a re-fabrication and has been routinely achieved with previous devices.

Diamond waveguides were measured at W-band using a WR-10 based measurement system. To aid in aligning the diamond waveguide to the input and output WR-10 of the measurement system, silicon micromachined flanges were attached to each end of the diamond waveguide. These flanges, mimicking standard waveguide flanges, were micromachined using DRIE. Figures 6.6 and 6.7 displays photographs of micromachined waveguides with attached flanges. Figure 6.8 shows a close-up of a silicon diamond waveguide and Figure 6.9 a close-up of a deep etched WR-3.

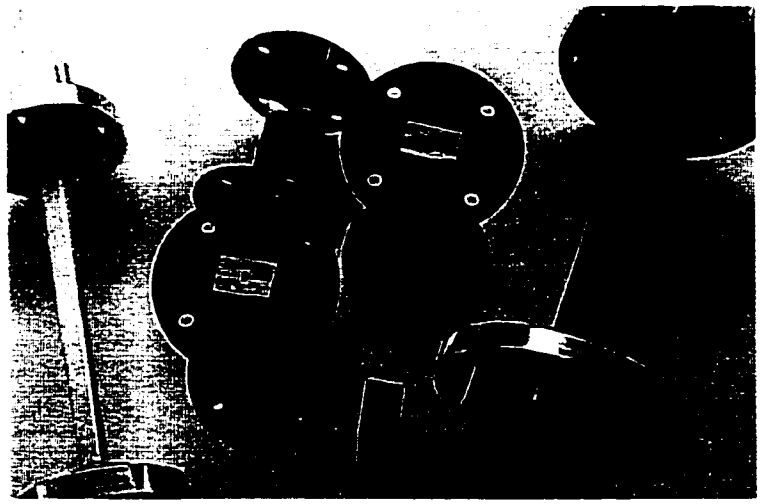

Figure 6.6: Photograph of both conventional (the leftmost and rightmost) and micromachined waveguides.

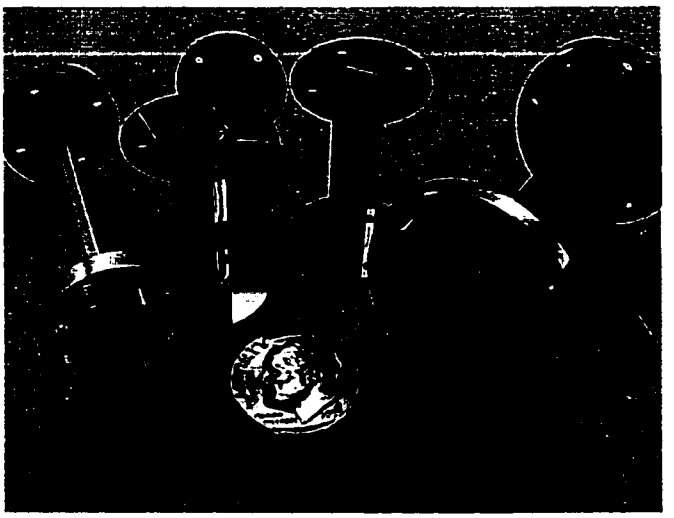

Figure 6.7: Micromachined and conventional (leftmost and rightmost) waveguides.

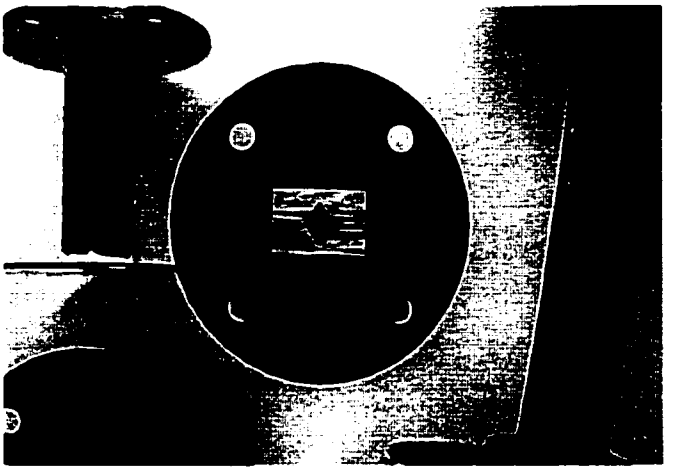

Figure 6.8: Close-up of a silicon diamond waveguide.

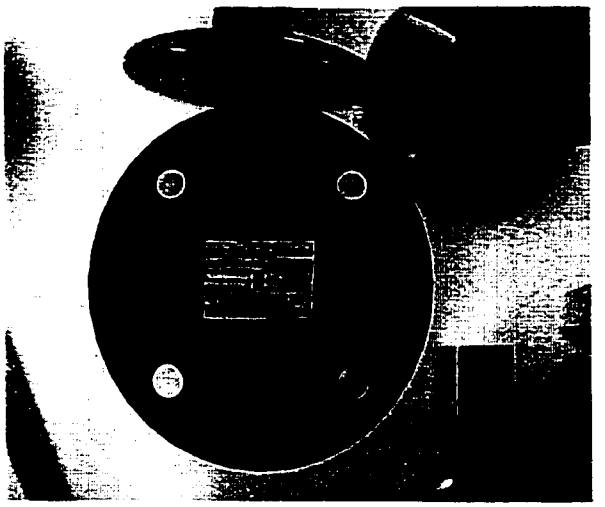

Figure 6.9: Close-up of a DRIE silicon WR-3.

The measurement system was calibrated to the ends of the input and output WR-10 ports using a standard waveguide calibration routine (short, offset short, matched load, and thru). Proper calibration was verified by examining the calibrated response of both the thru line and the short. The thru line exhibited negligible insertion loss and a return loss of better than -50 dB throughout the measurement range of 75-110 GHz. The calibrated response of the waveguide short exhibited a minimum return loss of –0.18 dB and phase = 180° ± 0.03° throughout. Figure 6.10 shows two photographs of the connection of the diamond section with the WR-10 feeds.

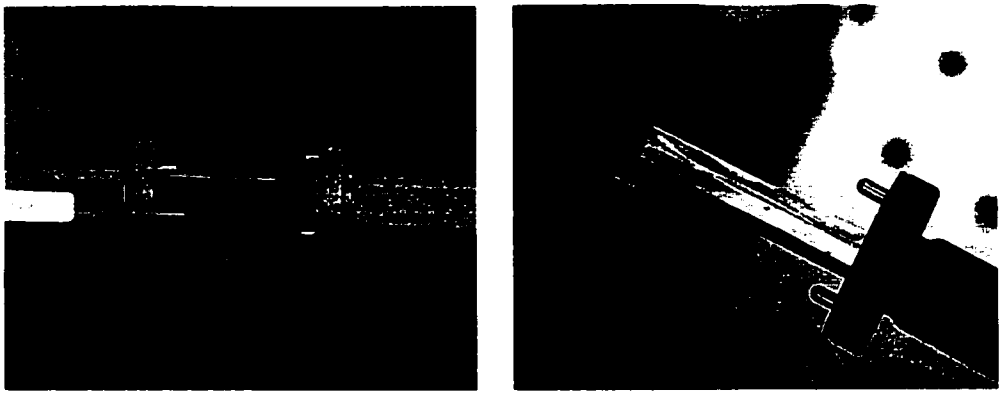

Figure 6.10: Two photographs of the connection of a section of W-band silicon diamond waveguide with conventional machined WR-10 feeds.

The measured response of a section of diamond waveguide of length 2.73 cm and cross sectional dimensions a = 2418 μm, b = 1710 μm is given in Figure 6.11. Clearly present in the insertion loss curve is the typical cutoff behavior of the dominant mode of a waveguide. Using equation 6.11, with a = 2514 μm, we expect a cutoff frequency of ~ 87.1 GHz which agrees well with the measured data. The standing wave pattern of the return loss is due to the mismatch between the WR-10 ports and the diamond waveguide. The nulls correspond to roughly $\lambda_g/2$ separation between the WR-10 ports, where λg is

the guided wavelength of the diamond waveguide, with reactive elements at the junction displacing the nulls slightly from exact $\lambda_g/2$ locations.

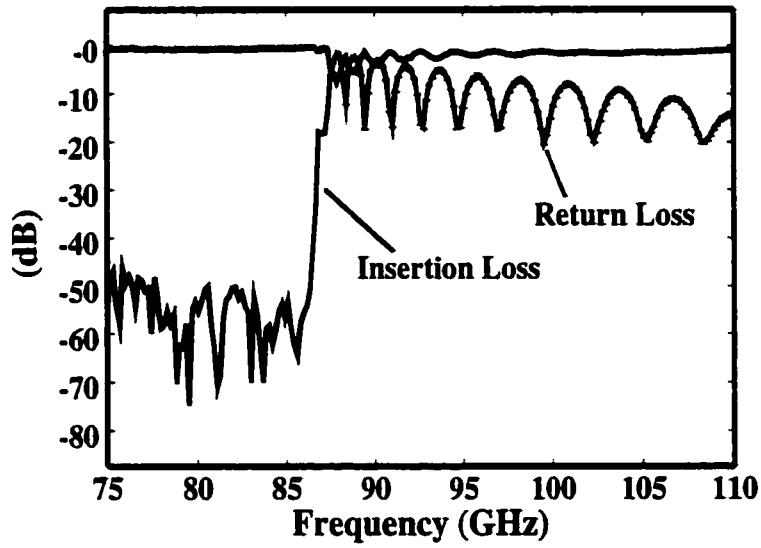

Figure 6.11: Measured s-parameters of a section of silicon diamond waveguide with dimensions of a = 2514 μm, b= 1778 μm, and length = 2.73 cm.

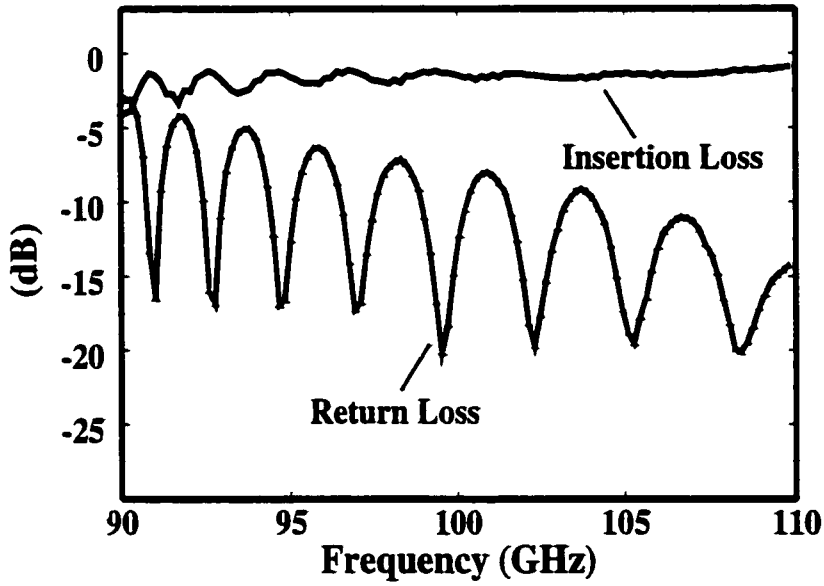

Figure 6.12: Passband s-parameters of a section of silicon diamond waveguide with dimensions of a = 2514 μm, b= 1778 μm, and length = 2.73 cm.

Figure 6.12 shows a close-up of the waveguide's passband. We see that the trend in the return loss is such that its peaks are steadily decreasing with frequency. This is a result of the decreasing impedance of the silicon diamond waveguide with increasing frequency, which thus becomes closer to that of the WR-10 ports.

6.3.2: Modeling of the diamond waveguide and test setup

Scanning electron microscopy and a conventional microscope revealed that the cross sectional dimensions of the measured diamond waveguide were approximately 2514 μm x 1778 μm (a x b) with a length of 2.73 cm (determined with a caliper). Full-wave simulation of the structure was completed using HFSS. The model consisted of a 2.73 cm section of diamond waveguide with appropriate cross sectional dimensions. Small sections of WR-10 were used to excite the diamond waveguide and the S-parameters de-embedded to the flange of the diamond guide. Such a model mimicked the measured setup (recall a waveguide calibration was used to move the reference plane to the flange of the diamond waveguide).

The conductivity of the walls of the modeled diamond waveguide was adjusted until the simulated insertion loss matched the measured results at the low frequency end of the diamond waveguide's passband. The frequency range to match simulated and measured insertion loss results was chosen at the low end of the scale as it was felt that parasitics due to imperfect connection between the WR-10 feeds and the diamond waveguide would be not be as critical at that part of the passband. A conductivity of 5.0×10^6 $(\Omega\text{-m})^{-1}$ was found to result in good agreement at the low frequency end. The return and insertion loss of the measured waveguide and the simulated version just described are given in Figure 6.13.

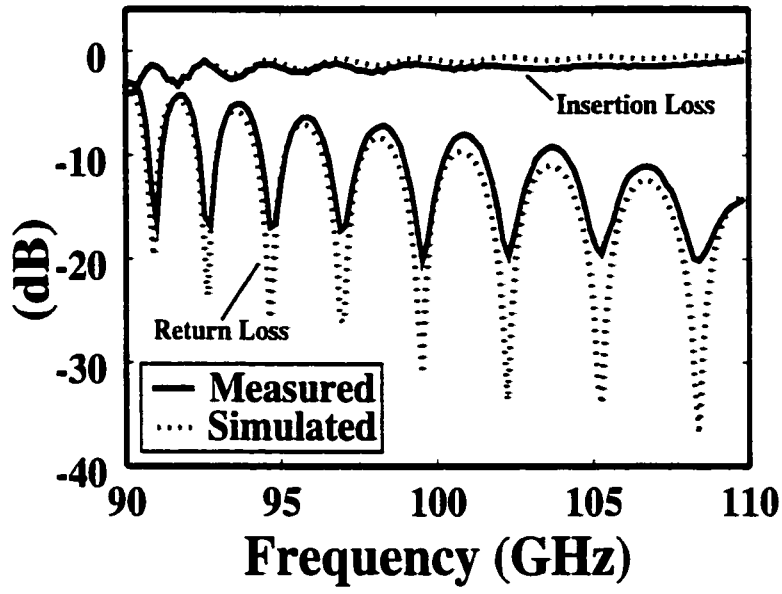

Figure 6.13: Simulated and measured insertion loss of a diamond waveguide (a = 2514 μm, b = 1788 μm, length = 2.73 cm.) A metal conductivity of 5.0×10^6 $(\Omega\text{-m})^{-1}$ was assumed for simulation.

The simulated and measured results of Figure 6.13 agree quite well in form over the waveguide's passband. The magnitude of the insertion loss of the measured guide falls short of the simulated results at higher frequencies. This result is believed to be an artifact of an imperfect connection between the diamond waveguide and the WR-10 feed ports. An example of the importance of the integrity of waveguide connections is demonstrated in Figure 6.14. In the figure, the s-parameters of a straight section of WR-10 are given for the case in which the guide is connected with two tightened screws at each connection and the case in which one of the screws at one of the connections is slightly loosened. A noticeable variation in the s-parameter response is evident in both the insertion and return loss results. The amount transmitted in the case in which a single screw is loosened is less, by as much as 0.37 dB, than that in the fully tightened case.

Clearly the quality of the connection can have a significant impact on the measured loss of the waveguide.

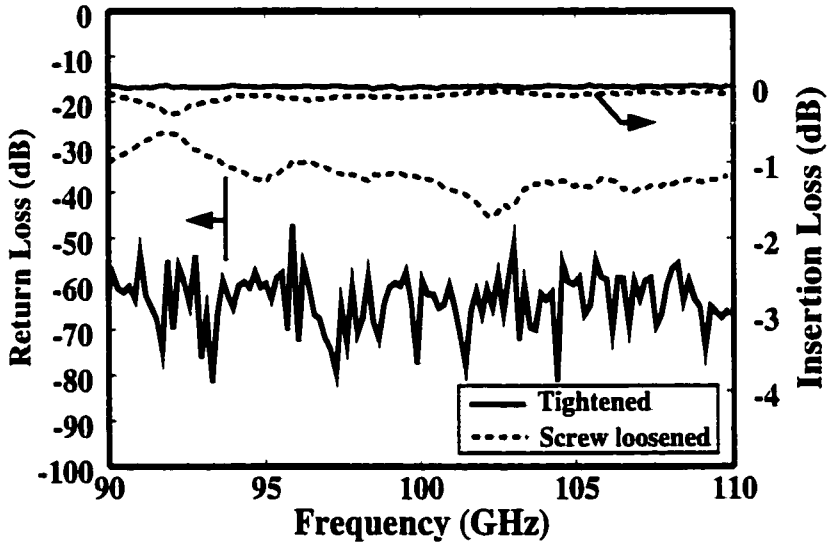

Figure 6.14: S-parameters of a straight section of WR-10. The solid curves display the performance of the waveguide when the flange connections to the excitation guides are properly tightened. The dashed curves give the results when a single connection screw is loosened.

Figure 6.15 displays the loss per guided wavelength as a function of frequency for the diamond waveguide of Figures 6.11 through 6.13. The isolated dots represent results based explicitly on measured insertion loss at the given frequency. These data points do not take into consideration the mismatch that exists between the waveguides and so overestimate the loss. The data points were selected at frequencies at which the return loss exhibited local minima however, and thus inaccuracies due to neglecting the return loss are mitigated. Further discussion of modeling the interconnection of the WR-10 feeds and the diamond waveguide is given in Appendix E.

The curves in Figure 6.15 were generated using insertion loss results from modeling the waveguide in HFSS. In these simulations, the excitation ports were defined to be the

diamond waveguide apertures and thus no mismatch existed in the simulated structures. As mentioned previously, an assumed conductivity of 5.0 x 10^6 $(\Omega\text{-m})^{-1}$ was found to match the insertion loss of the measured waveguide quite well at the low frequency end (up to about 93 GHz). For this reason, one of the curves (the solid curve) of Figure 6.15 shows the results of an HFSS simulation of a diamond waveguide assuming this conductivity. The simulated loss curve agrees quite well with the measured data at the low frequency end. A similar simulation was run with an assumed conductivity of 1.0 x 10^6 $(\Omega\text{-m})^{-1}$. In this case the simulated waveguide exhibits a higher loss than the measured guide at lower frequencies but is closer to the measured results at the high frequency end.

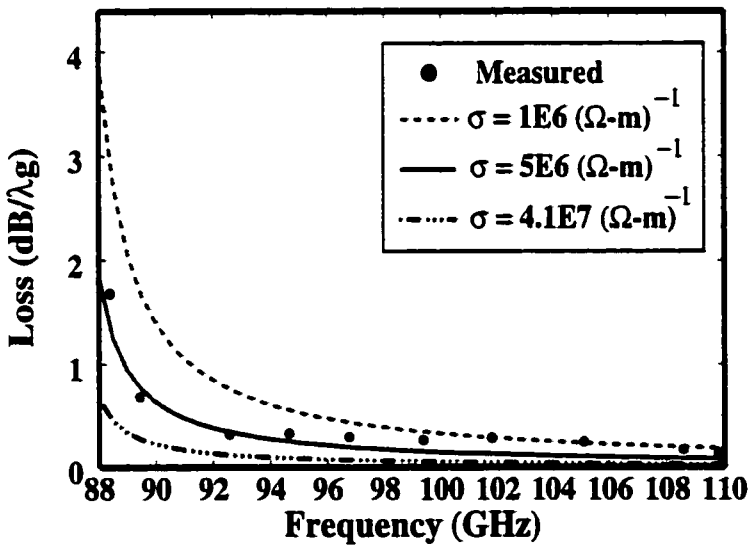

Figure 6.15: Loss performance of a W-band diamond waveguide (a = 2514 μm, b = 1788 μm). The dots represent loss per guided wavelength results based explicitly on measured insertion loss. The curves represent loss as determined through full-wave simulation for varying conductivities.

It seems quite reasonable that the conductivity of 5.0 x 10^6 $(\Omega\text{-m})^{-1}$ is more representative of the actual conductivity of the guide and that the waveguide's higher

frequency performance is obscured to some degree by the imperfect connections at the input and output flanges. Finally in Figure 6.15 simulation results for case of an assumed metal conductivity of 4.1×10^7 $(\Omega\text{-m})^{-1}$ (that of gold) is given and represents the optimum performance that could be reasonably expected.

The measured performance of the silicon diamond waveguide is compared in Figure 6.16 with that of other transmission lines developed on silicon. The results for the Finite Ground Coplanar (FGC) transmission line and the Micromachined Finite Ground Coplanar (MFGC) transmission line are taken from Table 2.1 of Herrick [9] and represent the best results found in that table. Extrapolated values for the FGC and MFGC were calculated based on conductive loss only. The microshield transmission line has been discussed in [83] and [84] – the results of Figure 6.16 are extrapolated based on the work of Weller [83]. Specifically, the best results of Figure 2.7 of [83] were used; at 40 GHz, the microshield in question exhibited a loss of ~ 0.3 dB/cm. The dB/λg value of the microshield was calculated assuming an effective dielectric constant of 1.07 (see relevant curves of [83]).

Transmission Line	Frequency	α (dB/cm)	α (dB/λ_g)	Ref.
Si WR-10	110 GHz	0.12	0.04	[11]
Si Diamond Waveguide	110 GHz	0.30	0.08 (0.135)	This work
SU-8 WR-10 (Reduced Height)	110 GHz	1.58	0.5	[32]
FGC	94 GHz 110 GHz	1.95 2.108	0.26 0.24	[9] Extrapolated
MFGC	94 GHz 110 GHz	0.80 0.87	0.13 0.12	[9] Extrapolated
Microshield	110 GHz	0.493	0.13	Extrapolated from [83]

Figure 6.16: Attenuation table of various transmission lines developed on silicon.

The results from the Si micromachined WR-10 are taken from the work of McGrath [11]. The quoted value of 0.04 dB/λ_g for the silicon WR-10 was actually determined at 100 GHz, but "*the measured loss is about 0.04 dB per wavelength across most of the band*" [11]. While no value for the loss in dB per unit length was given in the paper, 0.04 dB per wavelength should translate into an attenuation of ~0.11 dB/cm at 110 GHz for a WR-10. The quoted value of 0.135 dB/λ_g for the diamond waveguide is that taken directly from measurement and 0.08 dB/λ_g from the assumed conductivity of 5 x 10^6 $(\Omega\text{-m})^{-1}$ that was found to fit the measured data very well at lower frequencies. As evidenced by the values presented in Figure 6.16, the silicon diamond waveguide exhibits attenuation values that are competitive with the best results of planar lines developed on silicon and approach those of the silicon micromachined WR-10.

6.4: Conclusions

The difficulty in conventional manufacturing of THz waveguides has led investigators to explore micromachining techniques to replace conventional fabrication techniques. In this study, the silicon diamond waveguide has been fabricated and tested at W-band and has demonstrated loss performance competitive with (if not superior to) the best results from planar lines on silicon and a silicon WR-10. It is believed that the reported performance of the silicon diamond waveguide was limited by the integrity of the connection of the guide to the test structure and not by the inherent properties of the waveguide itself.

Through polishing to improve surface quality of the waveguide at the flanges and through the use of a flange that would allow tightening, it is believed that the performance of the diamond waveguide should approach its ideal. In an actual system,

the diamond may not need to be connected externally but rather utilize micromachined horn antennas to transmit and receive signals making the interconnection problem moot. To the author's knowledge the results presented herein are the only measured results reported on the silicon diamond waveguide. Interest in the diamond waveguide is evidenced by the work of Shenouda et al. [82] who have reported calculated attenuation curves for the diamond waveguide and measured radiation patterns of horn antennas that evolve naturally from the diamond waveguide.

The limited single-mode bandwidth of the diamond waveguide may be a concern in some systems. While Shenouda et al. [82] have proposed the incorporation of metallic fins within the diamond waveguide as a means to improve bandwidth, fabrication complexities may make development more difficult. A rectangular waveguide exhibits a significantly larger bandwidth than the diamond waveguide and should be characterized by lower loss. Deep reactive ion etching (DRIE) is a means to develop such waveguides in silicon. Figures 6.6, 6.7 and 6.9 show a WR-3 waveguide realized in silicon using DRIE; due to a lack of proper test equipment, the waveguide has not yet been tested. Perhaps the most important issue in developing the deep-etched waveguide is surface roughness. Future measurements should help address the prospect of employing DRIE of waveguides for THz system applications.

CHAPTER 7

PLANAR LINE TO MICROMACHINED WAVEGUIDE TRANSITIONS

7.1: Introduction

There are a variety of means used to couple signals from either coax or from planar circuitry to waveguides. While considerable work has been done on microstrip-to-waveguide transitions, comparatively fewer efforts have been made to establish suitable transitions from waveguide to FGC lines [85],[86]. In this chapter both magnetic and electric field coupling from an FGC transmission line to a micromachined waveguide are considered.

Analytical examination of an ideal side-launch magnetic coupling transition is detailed in the first part of this chapter. While the analytical model provides insight into the operation of the transition, its approximating nature underscores the need for full-wave simulation. Converting the idealized transition to a realizable micromachined version revealed that substrate coupling causes the magnetic-coupled micromachined version to be impractical. For this reason, an E-plane probe has been developed and is reported in the later portion of this chapter. Initial results demonstrate the viability of a fully micromachined version at 100 GHz. While the initial results are encouraging, additional fabrication challenges exist for extending the transition to true terahertz frequencies.

7.2: Magnetic field coupling

One means of coupling to a waveguide is through the use of a probe that interacts with the magnetic field existing within the guide. The proper orientation of a given probe is dictated by the mode pattern of the field. Below in Figure 7.1 is a schematic diagram of a rectangular waveguide with arrows suggesting the form of the magnetic field of the dominant TE mode (a > b).

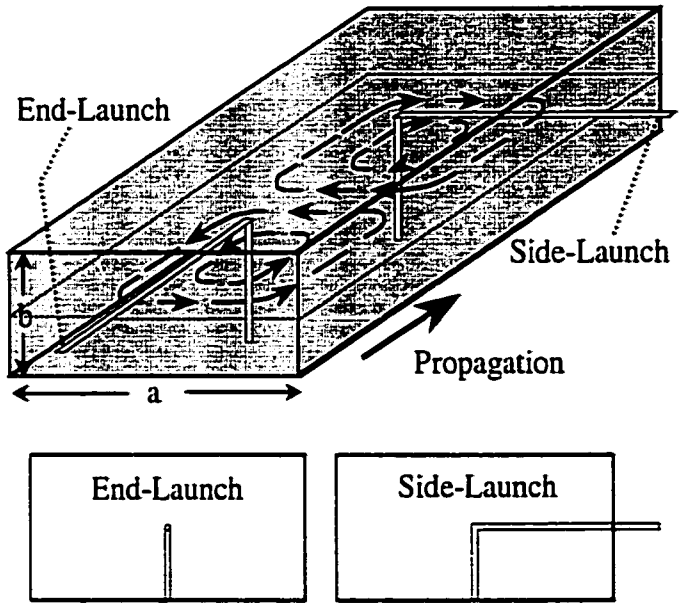

Figure 7.1: Schematic representation of coupling to the dominant-mode (via the magnetic field) in a rectangular waveguide using of either an end-launch or a side-launch loop probe.

Two probes are included in the figure, either of which can be used to couple with the magnetic field, and thus with the dominant mode. In both cases shown in the figure, the probe enters the waveguide through the narrow wall and forms a full loop by connection with the bottom wall of the waveguide. The end-launch loop is formed in the direction of propagation (i.e. the axial direction) and the side-launching loop, tranverse to the

direction of propagation. Figures 7.2 and 7.3 reveal, as originally envisioned, physically realizable side- and end-launch transitions to a micromachined waveguide. Both transitions rely on the extension of a signal ledge into the guide and upon which a loop is patterned. To begin discussion of magnetic coupling to the waveguide, a simplified model is pursued.

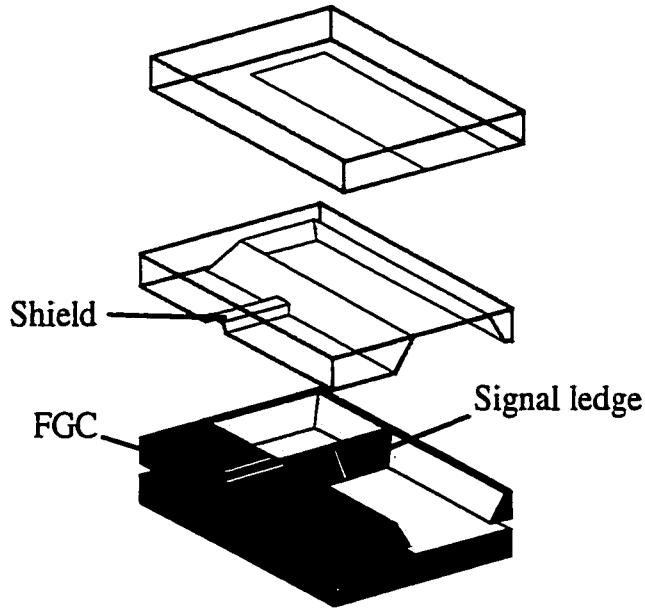

Figure 7.2: "Exploded" view of the originally proposed side-launch transition.

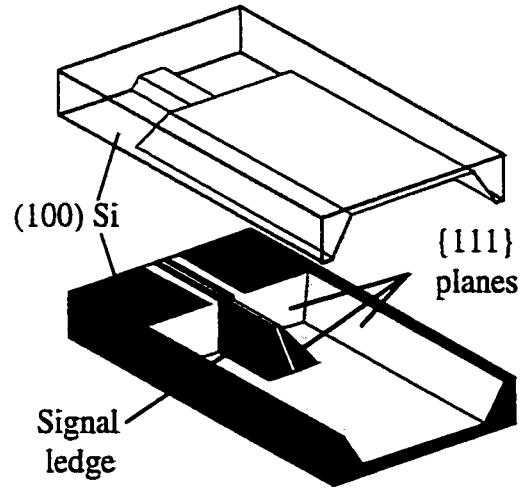

Figure 7.3: Schematic diagram of the originally proposed end-launch transition. A backing wafer could be included to allow for metallization underneath the signal ledge.

7.2.1: "Coaxial FGC" Side-Launching Transition Structure

In this section we consider a *rectangular* waveguide fed with a *fully-shielded* FGC line. Simple schematic diagrams of the structure are given in Figures 7.4 and 7.6. Such a structure is chosen as a starting point for several reasons. First, this transition affords the best possibility to form an analytical solution of the problem of achieving efficient signal transfer from the line to the guide. It was hoped that the basic model built on this analytical solution should serve as a guideline to aid in developing the more complex transition of Figure 7.2. A second reason why the structure is attractive as a starting point rests in the fact that it is fully-shielded thus eliminating radiation loss. To further simplify matters, all conductors are considered to be perfectly conducting. By neglecting loss, simulation time is significantly improved; more important is the fact that deembedding along the FGC line to the mouth of the feed will allow us to get an accurate feel for the input impedance at that point.

An accurate accounting of the input impedance at the feed point is of course critical for matching to the transmission line. It has been found that when employing an unshielded line in the waveguide feed structure, a significant portion of the reflected signal may be lost to radiation and thus is unaccounted for in the return loss, as monitored at the excitation port of the FGC line feed. In such cases, deembedding to the mouth of the feed does not give an accurate indication of the input impedance at that point.

A static field analysis using Maxwell 2D (Ansoft HFSS) aided in selecting an appropriate geometry for the coaxial FGC line; a schematic diagram of the chosen geometry is given in Figure 7-5. An impedance of 55 Ω was settled on for the coaxial FGC. This coaxial FGC line was then used to feed a rectangular waveguide as suggested

in Figure 7.6. The top wall of the guide is omitted from the figure for clarity. The position of the loop from the backshort (denoted "ℓ") and the loop's "extension length" (denoted "L") may be varied to help effect a good match between the transmission line and the waveguide. The height of the probe (h) is fixed at half the waveguide height in order to facilitate potential fabrication (see Figure 7.22 for clarification of this point).

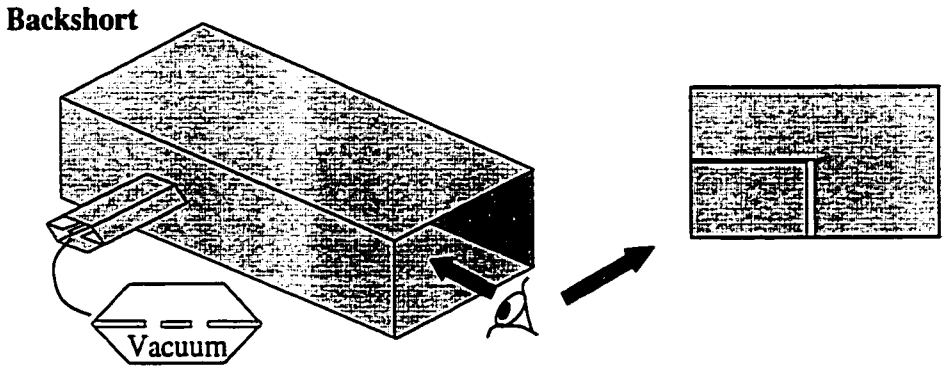

Figure 7.4: Schematic diagram of the initial side-launch structure – a rectangular waveguide fed with an fully shielded FGC line.

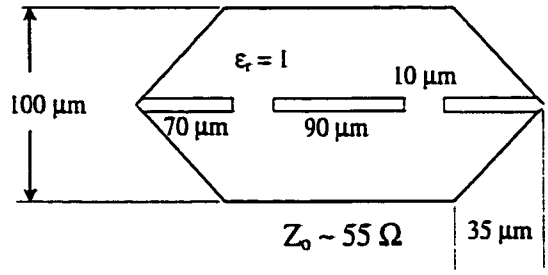

Figure 7.5: Schematic diagram of the selected coaxial FGC line.

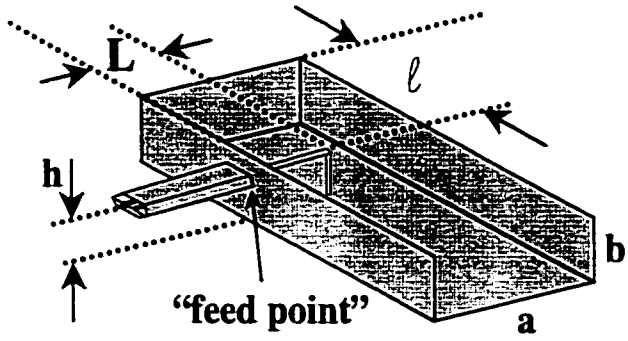

Figure 7.6: Schematic diagram illustrating the parameters used to match the FGC line to the waveguide. The top wall of the waveguide has been omitted for clarity.

7.2.2: Analytical Analysis of the Coaxially-fed Side-Launching Loop

The analysis that follows draws heavily from the work of Harrington [87]. Figure 7.7 offers additional views of the side-launching transition depicted in Figure 7.6 and will serve as aid during our analytical analysis. The waveguide has the cross-sectional dimensions of width a and height b, with the magnetic probe considered to lie exclusively in the z = 0 cross-section.

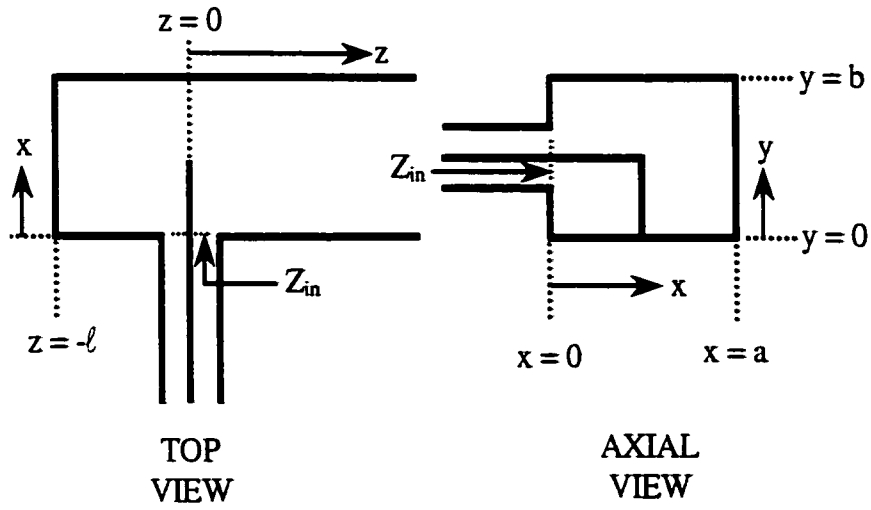

Figure 7.7: Top and axial views of a coax-to-waveguide feed that utilizes magnetic field coupling via a side-launching loop.

For this transition to operate, a backshort is placed at $z = -\ell$ and it is assumed that the guide has a matched termination at $z = +\infty$. Since the boundary conditions that we will invoke are based upon the transverse (i.e. the x and y) components of the electromagnetic field, we write:

$$\bar{E}_t^+ = \sum_i \frac{V_i}{1+\Gamma_i^+}\left(e^{-\gamma_i z} + \Gamma_i^+ e^{\gamma_i z}\right)\hat{e}_i \qquad [7.1]$$

and

$$\bar{H}_t^+ = \sum_i \frac{V_i Y_i}{1+\Gamma_i^+}\left(e^{-\gamma_i z} - \Gamma_i^+ e^{\gamma_i z}\right)\hat{h}_i \qquad [7.2]$$

for the $z \geq 0$ region.

The following define the symbols in the above equations:

- $\bar{E} \equiv$ electric field,
- $\bar{H} \equiv$ magnetic field,
- $t \equiv$ transverse component,
- $+ \equiv +z$ component or coefficient,
- $V_i \equiv$ mode voltage of the i^{th} mode,
- $\Gamma_i^+ \equiv +z$ reflection coefficient for the i^{th} mode referred to z=0,
- $\gamma_i \equiv$ propagation constant for the i^{th} mode,
- $Y_i \equiv$ characteristic admittance of the i^{th} mode,
- $\hat{e}_i \equiv$ electric field mode function of the i^{th} mode, and
- $\hat{h}_i \equiv$ magnetic field mode function of the i^{th} mode.

In a similar fashion for the $z \leq 0$ region, we have:

$$\vec{E}_t^- = \sum_i \frac{V_i}{1+\Gamma_i^-}\left(e^{\gamma_i z} + \Gamma_i^- e^{-\gamma_i z}\right)\hat{e}_i \qquad [7.3]$$

and

$$\vec{H}_t^- = -\sum_i \frac{V_i Y_i}{1+\Gamma_i^-}\left(e^{\gamma_i z} - \Gamma_i^- e^{-\gamma_i z}\right)\hat{h}_i \ . \qquad [7.4]$$

It should be noted that the $1+\Gamma$ factor in the denominator of equations [7.1] through [7.4] has been added to simplify the expressions ensuring continuity of the transverse component of the electric field at $z = 0$. This is illustrated by recalling that the Γ_i's have $z = 0$ as their reference plane. That is,

$$\vec{E}_t^+(z=0) = \sum_i \frac{V_i}{1+\Gamma_i^+}\left(e^{-\gamma_i 0} + \Gamma_i^+ e^{\gamma_i 0}\right)\hat{e}_i = \sum_i V_i \hat{e}_i$$

and

$$\vec{E}_t^-(z=0) = \sum_i \frac{V_i}{1+\Gamma_i^-}\left(e^{-\gamma_i 0} + \Gamma_i^- e^{\gamma_i 0}\right)\hat{e}_i = \sum_i V_i \hat{e}_i \ .$$

The boundary condition for the transverse component of the magnetic field in the cross-section of the probe states that

$$\vec{J}_s = \hat{u}_z \times \left(\vec{H}_t^+ - \vec{H}_t^-\right)\Big|_{z=0} \qquad [7.5]$$

where $\vec{J}_s$ is simply the current in the $z = 0$ cross-section and exists on the loop probe. Inserting equations [7.2] and [7.4] into equation [7.5] we find that,

$$\vec{J}_s = \hat{u}_z \times \left(\sum_i \frac{V_i Y_i}{1+\Gamma_i^+}\left(1-\Gamma_i^+\right)\hat{h}_i + \sum_i \frac{V_i Y_i}{1+\Gamma_i^-}\left(1-\Gamma_i^-\right)\hat{h}_i \right),$$

or simply

$$\bar{J}_s = \hat{u}_z \times \left(\sum_i V_i Y_i \left(\frac{1-\Gamma_i^-}{1+\Gamma_i^-} + \frac{1-\Gamma_i^+}{1+\Gamma_i^+} \right) \hat{h}_i \right) . \qquad [7.6]$$

Now let's scalar multiply both sides by $\hat{e}_i$, thus obtaining for each mode i:

$$-\bar{J}_s \bullet \hat{e}_i = V_i Y_i \left(\frac{1-\Gamma_i^-}{1+\Gamma_i^-} + \frac{1-\Gamma_i^+}{1+\Gamma_i^+} \right) e_i^2 .$$

One property of the normalized mode vector is that (see page 383 of [87])

$$\int_s e^2 ds = 1 . \qquad [7.7]$$

Therefore, integrating over the $z = 0$ cross-section for a single mode, we find that

$$-\int_s \bar{J}_s \bullet \hat{e}_i ds = V_i Y_i \left(\frac{1-\Gamma_i^-}{1+\Gamma_i^-} + \frac{1-\Gamma_i^+}{1+\Gamma_i^+} \right) . \qquad [7.8]$$

From the above series of equations we see that the fields can be completely determined if the excitation source $\bar{J}_s$ and the mode reflection coefficients are known. That is, the mode voltages may be determined from [7.8] and then used in [7.1] through [7.3]. This will not be our approach however as we will derive a value for the input impedance based on an assumed current distribution and the known mode vectors.

The stationary formulation for the input impedance yields the result that

$$Z_{in} = -\frac{1}{I_{in}^2} \int_s \bar{E} \bullet \bar{J}_s ds \qquad [7.9]$$

where the integration is over the $z = 0$ cross-section and I_{in} refers to the input current at

$x = 0$. Since $\bar{J}_s$ has only a transverse component (i.e. no z component), the transverse electric field is the only component of the electric field that would survive in the dot product of equation [7.9] and is given by:

$$\bar{E}_t\Big|_{z=0} = \sum_i V_i \hat{e}_i \,. \qquad [7.10]$$

Recognizing that $\hat{u}_z \times \hat{h}_i = -\hat{e}_i$, we find using equations [7.6] and [7.10], that equation [7.9] may be recast as

$$Z_{in} = \frac{1}{I_{in}^2} \int_s \sum_i V_i^2 Y_i \left(\frac{1-\Gamma_i^-}{1+\Gamma_i^-} + \frac{1-\Gamma_i^+}{1+\Gamma_i^+} \right) e_i^2 ds \,.$$

Once again invoking equation [7.7], we have

$$Z_{in} = \frac{1}{I_{in}^2} \sum_i V_i^2 Y_i \left(\frac{1-\Gamma_i^-}{1+\Gamma_i^-} + \frac{1-\Gamma_i^+}{1+\Gamma_i^+} \right) . \qquad [7\text{-}11]$$

Solving equation [7.8] for V_i and recognizing $1/Y_i$ as the characteristic impedance of mode i, denoted Z_i, we may write that

$$V_i = -\frac{Z_i \int_s \bar{J}_s \bullet \hat{e}_i ds}{\frac{1-\Gamma_i^-}{1+\Gamma_i^-} + \frac{1-\Gamma_i^+}{1+\Gamma_i^+}} \,.$$

Using this result in equation [7.11] we arrive at a stationary formula for the input impedance of a zero-thickness (i.e. probe with negligible axial dimension) coax-to-waveguide feed, (equation 8-143 of [87]) namely,

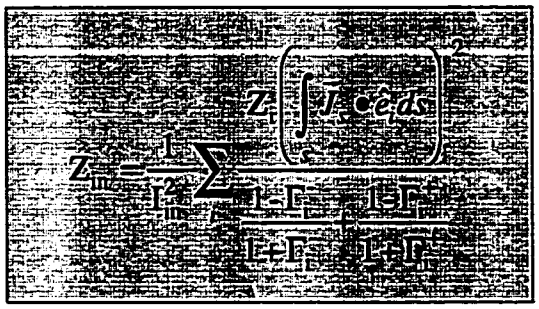

[7.12]

Equation [7.12] may be recast by noting that the plus and minus wave impedances of the i^{th} mode referred to z = 0 are as follows:

$$\hat{Z}_i^+ = Z_i \frac{1+\Gamma_i^+}{1-\Gamma_i^+} \qquad [7.13]$$

and

$$\hat{Z}_i^- = Z_i \frac{1+\Gamma_i^-}{1-\Gamma_i^-}. \qquad [7.14]$$

These results are derived as follows by considering continuity of the wave impedance at the z = 0 interface. For instance, in the $z \geq 0$ region,

$$Z_i^+(z) = \frac{E_t^+(z)}{H_t^+(z)} = \frac{\dfrac{V_i}{1+\Gamma_i^+}\left(e^{-\gamma_i z} + \Gamma_i^+ e^{\gamma_i z}\right)}{\dfrac{V_i Y_i}{1+\Gamma_i^+}\left(e^{-\gamma_i z} - \Gamma_i^+ e^{\gamma_i z}\right)}.$$

Evaluating the above expression at z = 0 we obtain expression [7.13]; and in a similar fashion from $\hat{Z}_i^-$, expression [7.14].

Now let's take the parallel combination of the + and – impedances at z = 0. That is,

$$\hat{Z}_i^+ \parallel \hat{Z}_i^- = \frac{\hat{Z}_i^+ \hat{Z}_i^-}{\hat{Z}_i^+ + \hat{Z}_i^-},$$

which can be rewritten as follows:

$$\hat{Z}_i^+ \parallel \hat{Z}_i^- = Z_i \frac{\dfrac{\left(1+\Gamma_i^+\right)\left(1+\Gamma_i^-\right)}{\left(1-\Gamma_i^+\right)\left(1-\Gamma_i^-\right)}}{\dfrac{\left(1+\Gamma_i^+\right)}{\left(1-\Gamma_i^+\right)}+\dfrac{\left(1+\Gamma_i^-\right)}{\left(1-\Gamma_i^-\right)}} = Z_i \frac{\dfrac{\left(1+\Gamma_i^+\right)\left(1+\Gamma_i^-\right)}{\left(1-\Gamma_i^+\right)\left(1-\Gamma_i^-\right)}}{\dfrac{\left(1+\Gamma_i^+\right)\left(1-\Gamma_i^-\right)+\left(1+\Gamma_i^-\right)\left(1-\Gamma_i^+\right)}{\left(1-\Gamma_i^+\right)\left(1-\Gamma_i^-\right)}}.$$

And thus,

$$\hat{Z}_i^+ \parallel \hat{Z}_i^- = Z_i \frac{\left(1+\Gamma_i^+\right)\left(1+\Gamma_i^-\right)}{\left(1+\Gamma_i^+\right)\left(1-\Gamma_i^-\right)+\left(1+\Gamma_i^-\right)\left(1-\Gamma_i^+\right)}. \qquad [7.15]$$

Now the denominator of equation [7.12] may be arranged as follows:

$$\frac{1-\Gamma_i^-}{1+\Gamma_i^-}+\frac{1-\Gamma_i^+}{1+\Gamma_i^+} = \left[\frac{\left(1+\Gamma_i^+\right)\left(1+\Gamma_i^-\right)}{\left(1+\Gamma_i^+\right)\left(1-\Gamma_i^-\right)+\left(1+\Gamma_i^-\right)\left(1-\Gamma_i^+\right)}\right]^{-1}.$$

Thus equation [7.12] can be rewritten as

$$Z_{in} = \frac{1}{\Gamma_{in}^2}\sum_i \left(\int_s \bar{J}_s \bullet \hat{e}_i ds\right)^2 \frac{\left(1+\Gamma_i^+\right)\left(1+\Gamma_i^-\right)}{\left(1+\Gamma_i^+\right)\left(1-\Gamma_i^-\right)+\left(1+\Gamma_i^-\right)\left(1-\Gamma_i^+\right)},$$

which using equation [7.15] leads finally to

$$Z_{in} = \frac{1}{\Gamma_{in}^2}\sum_i \left(\int_s \bar{J}_s \bullet \hat{e}_i ds\right)^2 Z_i \parallel Z_i. \qquad [7.16]$$

Equation [7.16] suggests, as Harrington ([87] p. 427) points out, the result that the $z > 0$ and $z < 0$ guides appear in parallel for each mode. We now take departure from Harrington's analysis to investigate the effects of the backshort that exists at $z = -\ell$ (see Figure 7.7).

We will concern ourselves with the effects of the backshort on $Z_i^-(z)$, and then transfer its effects via boundary conditions at the $z = 0$ interface.

In the region $z \leq 0$,

$$Z_i^-(z) = -\frac{E_t^-(z)}{H_t^-(z)} = \frac{\dfrac{V_i}{1+\Gamma_i^-(z)}\left(e^{\gamma_i z} + \Gamma_i^-(z)e^{-\gamma_i z}\right)}{\dfrac{V_i Y_i}{1+\Gamma_i^-(z)}\left(e^{\gamma_i z} - \Gamma_i^-(z)e^{-\gamma_i z}\right)}.$$

This may be expressed as follows:

$$Z_i^-(z) = Z_i \frac{e^{\gamma_i z} + \Gamma_i^-(z)e^{-\gamma_i z}}{e^{\gamma_i z} - \Gamma_i^-(z)e^{-\gamma_i z}} . \qquad [7.17]$$

From equation [7.17] it is clear that we must determine the minus reflection coefficient for each mode as a function of z (in the $z \leq 0$ region). To aid in this effort, consider the following figure (Figure 7.8) that depicts the $z \leq 0$ region as a uniform transmission line with characteristic impedance Z_i and propagation constant γ_i, each corresponding to the mode i. The line is terminated with a load impedance Z_L located at $z = -\ell$.

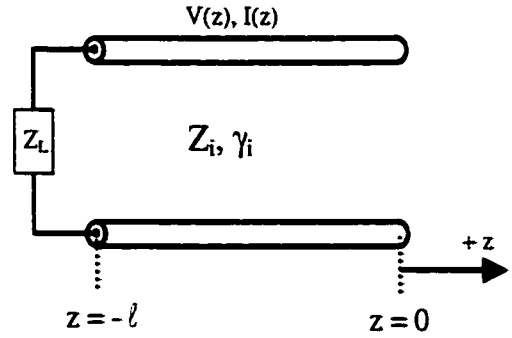

Figure 7.8: A transmission line representation of the $z \leq 0$ region of the waveguide.

The excitation source, namely the loop as depicted in Figure 7.7, lies in the z = 0 cross-section. The incident wave in the $z \leq 0$ region (i.e. that incident on the load) may thus be expressed as follows:

$$\text{Incident Wave} \equiv V_i^- e^{j\gamma_i z}.$$

Any mismatch that exists between the line and the load impedance produces a reflected wave that may be expressed as:

$$\text{Reflected Wave} \equiv V_i^+ e^{-j\gamma_i z}.$$

It is important to note that V_i^+ and V_i^- are both referenced to z = 0 to be in accord with the stationary impedance formulation detailed above. The total voltage and current on the line (again, in the $z \leq 0$ region) of the i^{th} mode may be expressed as:

$$V_i^{z\leq 0}(z) = V_i^+ e^{-j\gamma_i z} + V_i^- e^{j\gamma_i z}$$

and

$$I_i^{z\leq 0}(z) = \frac{V_i^+}{Z_i} e^{-j\gamma_i z} - \frac{V_i^-}{Z_i} e^{j\gamma_i z}$$

respectively. The total voltage and current are related at the load by the load impedance as shown below. That is,

$$Z_L = \frac{V_i^{z\leq 0}(-\ell)}{I_i^{z\leq 0}(-\ell)} = \frac{V_i^+ e^{j\gamma_i \ell} + V_i^- e^{-j\gamma_i \ell}}{\frac{V_i^+}{Z_i} e^{j\gamma_i \ell} - \frac{V_i^-}{Z_i} e^{-j\gamma_i \ell}}$$

or,

$$Z_L = Z_i \frac{V_i^+ e^{j\gamma_i \ell} + V_i^- e^{-j\gamma_i \ell}}{V_i^+ e^{j\gamma_i \ell} - V_i^- e^{-j\gamma_i \ell}}.$$

Rearranging the above equation we find that

$$Z_L\left(V_i^+ e^{j\gamma_i \ell} - V_i^- e^{-j\gamma_i \ell}\right) = Z_i\left(V_i^+ e^{j\gamma_i \ell} + V_i^- e^{-j\gamma_i \ell}\right)$$

or,

$$V_i^+ e^{j\gamma_i \ell}(Z_L - Z_i) = V_i^- e^{-j\gamma_i \ell}(Z_L + Z_i).$$

Recalling that V_i^+ corresponds to the reflected wave in this case, it is true that

$$\frac{V_i^+ e^{j\gamma_i \ell}}{V_i^- e^{-j\gamma_i \ell}} = \frac{Z_L + Z_i}{Z_L - Z_i} = \Gamma_i^-(z = -\ell) .$$

In the case of Figure 7.7, $Z_L = 0$ and therefore,

$$\Gamma_i^-(z = -\ell) = \frac{V_i^+ e^{j\gamma_i \ell}}{V_i^- e^{-j\gamma_i \ell}} = -1 . \qquad [7.18]$$

Equation [7.18] may be rearranges to reveal that

$$V_i^+ = -V_i^- e^{-j2\gamma_i \ell} . \qquad [7.19]$$

Equation [7.17] calls for a knowledge of the Γ_i's; at $z = 0$,

$$\Gamma_i^-(z = 0) = \frac{V_i^+}{V_i^-} = -e^{-j2\gamma_i \ell} . \qquad [7.20]$$

Making use of equation [7.19] for the $z \leq 0$ region we find that,

$$\Gamma_i^-(z) = \frac{V_i^+ e^{-j\gamma_i z}}{V_i^- e^{j\gamma_i z}} = \frac{-V_i^- e^{-j2\gamma_i \ell} e^{-j\gamma_i z}}{V_i^- e^{j\gamma_i z}} .$$

Simplifying the above equation we arrive at the following:

$$\Gamma_i^-(z) = -e^{-j2\gamma_i(z+\ell)} . \qquad [7.21]$$

It is clear that expression [7.21] satisfies both [7.18] and [7.20]. Inserting equation [7.21] into [7.17], we find that

$$Z_i^-(z) = Z_i \frac{e^{\gamma_i z} - e^{-j2\gamma_i(z+\ell)} e^{-\gamma_i z}}{e^{\gamma_i z} + e^{-j2\gamma_i(z+\ell)} e^{-\gamma_i z}} .$$

This leaves us with the following expression for the wave impedance of the i^{th} mode as a function of z in the $z \leq 0$ region:

$$Z_i^-(z) = Z_i \frac{e^{\gamma_i z} - e^{-j\gamma_i(3z+2\ell)}}{e^{\gamma_i z} + e^{-j\gamma_i(3z+2\ell)}} . \qquad [7.22]$$

When evaluated at $z = 0$, equation [7.22] reduces to the following expression:

$$Z_i^-(z=0) \equiv \hat{Z}_i^- = Z_i \frac{1 - e^{-j2\gamma_i \ell}}{1 + e^{-j2\gamma_i \ell}} . \qquad [7.23]$$

We assume that the waveguide is matched in the $z \geq 0$ region and thus all Γ_i^+'s $= 0$. This implies that (see equation [7.13]),

$$\hat{Z}_i^+ = Z_i \text{ for all i} .$$

Thus equation [7.16] may be recast to reveal that

$$Z_{in} = \frac{1}{I_{in}^2} \sum_i \left(\int_s \bar{J}_s \bullet \hat{e}_i ds \right)^2 Z_i \,\|\, \hat{Z}_i^- . \qquad [7.24]$$

Let us further assume that the *only propagating mode is the dominant mode* (i = 0 mode), that is, we are operating in the waveguide's proscribed single-mode frequency band. Under such an assumption the following are true:

$$Z_i \text{ is real for i} = 0$$

and

$$Z_i \text{ is imaginary for all i} \neq 0 .$$

Consider again equation [7.23], and replacing $2\gamma_i \ell$ with θ, we find that

$$Z_i^-(z=0) \equiv \hat{Z}_i^- = Z_i \frac{1-e^{-j\theta}}{1+e^{-j\theta}} .$$

This expression may be expanded and then simplified as follows:

$$\hat{Z}_i^- = Z_i \frac{1-e^{-j\theta}}{1+e^{-j\theta}} = Z_i \frac{[1-\cos(\theta)]+j\sin(\theta)}{[1+\cos(\theta)]-j\sin(\theta)} .$$

Multiplying by the complex conjugate of the denominator and continuing from there we find that,

$$\hat{Z}_i^- = Z_i \frac{1-\cos^2(\theta)+j2\sin(\theta)-\sin^2(\theta)}{[1+\cos(\theta)]^2+\sin^2(\theta)} .$$

We can manipulate the above equation to reveal that

$$\hat{Z}_i^- = Z_i \frac{j2\sin(\theta)}{2[1+\cos(\theta)]} = jZ_i \frac{2\sin\left(\frac{\theta}{2}\right)\cos\left(\frac{\theta}{2}\right)}{2\cos^2\left(\frac{\theta}{2}\right)} = jZ_i \tan\left(\frac{\theta}{2}\right),$$

and thus,

$$\hat{Z}_i^- = jZ_i \tan(\gamma_i \ell). \qquad [7.25]$$

Returning to equation [7.24], we see that the parallel combination of Z_i and $\hat{Z}_i^-$ is of interest, and which, using [7.25], may be expressed in a convenient form as demonstrated below. Namely,

$$Z_i \parallel \hat{Z}_i^- = Z_i \parallel jZ_i \tan(\gamma_i \ell) = \frac{jZ_i^2 \tan(\gamma_i \ell)}{Z_i + jZ_i \tan(\gamma_i \ell)}$$

or,

$$Z_i \parallel \hat{Z}_i^- = Z_i \frac{\tan^2(\gamma_i \ell)}{1+\tan^2(\gamma_i \ell)} + jZ_i \frac{\tan(\gamma_i \ell)}{1+\tan^2(\gamma_i \ell)} .$$

We may further simplify the previous equation to reveal that,

$$Z_i \left\| \hat{Z}_i^- = Z_i \sin^2(\gamma_i \ell) + jZ_i \frac{1}{2}\sin(2\gamma_i \ell) \right. . \qquad [7.26]$$

The parallel combination of the impedances exhibits the following properties:

$$Z_i \left\| \hat{Z}_i^- = 0 \right. \quad \text{when } \gamma_i \ell = n\pi \quad \text{where n = 0, 1, 2, 3, ...}$$

$$Z_i \left\| \hat{Z}_i^- = Z_i \right. \quad \text{when } \gamma_i \ell = m\frac{\pi}{2} \quad \text{where m = 1, 3, 5, ...}$$

or,

$$Z_i \left\| \hat{Z}_i^- = 0 \right. \quad \text{when } \ell = n\frac{\lambda_{gi}}{2} \quad \text{where n = 0, 1, 2, 3, ...}$$

$$Z_i \left\| \hat{Z}_i^- = Z_i \right. \quad \text{when } \ell = m\frac{\lambda_{gi}}{4} \quad \text{where m = 1, 3, 5, ...}$$

The above conditions reveal that we may short out a given mode by locating the loop an integer number of half-wavelengths (for the given mode) from the backshort. By placing the loop an odd integer number of quarter-wavelengths for the given mode from the backshort, we are left with simply the mode impedance. Of course, in the general case, each mode will contribute to both the real and imaginary portions of the input impedance.

We now may rewrite [7.24] as

$$Z_{in} = \frac{1}{\Gamma_{in}^2} \sum_i \left(\int_s \bar{J}_s \bullet \hat{e}_i ds \right)^2 \left(Z_i \sin^2(\gamma_i \ell) + jZ_i \frac{1}{2}\sin(2\gamma_i \ell) \right) . \qquad [7.27]$$

As long as there are no obstacles in the guide near the feed, we may assume that $\Gamma_i^- = \Gamma_i^+ = 0$ for all $i \neq 0$ as the $i \neq 0$ modes are evanescent in the frequency range

considered and thus will rapidly decay from the z = 0 cross-section. This implies that, in accord with [7.13] and [7.14],

$$\hat{Z}_i^+ = \hat{Z}_i^- = Z_i \quad \text{for } i \neq 0$$

and

$$\hat{Z}_i^+ \| \hat{Z}_i^- = \frac{Z_i}{2} \quad \text{for } i \neq 0 .$$

Now let's define "n" as does Harrington ([87] p. 427), namely,

$$n^2 = \frac{1}{I_{in}^2}\left(\int_s \vec{J}_s \bullet \hat{e}_0 ds\right)^2 . \qquad [7.28]$$

With the help of [7.28], equation [7.27] may be expressed as,

$$Z_{in} = n^2\left[Z_0 \sin^2(\gamma_0 \ell) + jZ_0 \frac{1}{2}\sin(2\gamma_0 \ell)\right] + \frac{1}{I_{in}^2}\sum_{i\neq 0}\left(\int_s \vec{J}_s \bullet \hat{e}_i ds\right)^2 \frac{Z_i}{2} . \qquad [7.29]$$

This expression for the input impedance may be broken up into its real and imaginary components as follows. Recalling that all Z_i for $i \neq 0$ are imaginary, we may write

$$R_{in} = n^2 Z_0 \sin^2(\gamma_0 \ell) \qquad [7.30]$$

and

$$X_{in} = jn^2 \frac{Z_0}{2}\sin(2\gamma_0 \ell) + \frac{1}{I_{in}^2}\sum_{i\neq 0}\left(\int_s \vec{J}_s \bullet \hat{e}_i ds\right)^2 \frac{Z_i}{2} . \qquad [7.31]$$

Our next step is to consider the current distribution on the probe. Before doing so however we express the input impedance in the rather general form from which we will build an equivalent circuit. Specifically,

$$Z_{in} = n^2 Z_0 \left\| \hat{Z}_0^- + jX \right. \qquad [7.32]$$

where

$$X = \frac{1}{I_{in}^2} \sum_{i \neq 0} \left(\int_s \bar{J}_s \bullet \hat{e}_i ds \right)^2 \left| Z_i \left\| \hat{Z}_i^- \right| \right. .$$

From equation [7.32], the following equivalent circuit (Figure 7.9) for the transition may be constructed (and is similar to that given in Harrington [87] Figure 8-26a). We see that the factor n may be considered as the turns ratio of a transformer. It should be kept in mind that the transforming action on the parallel combination of the dominant mode impedances results in a contribution to both the real and imaginary parts of Z_{in} as, while Z_o is purely real, $\hat{Z}_0^-$ is in general imaginary.

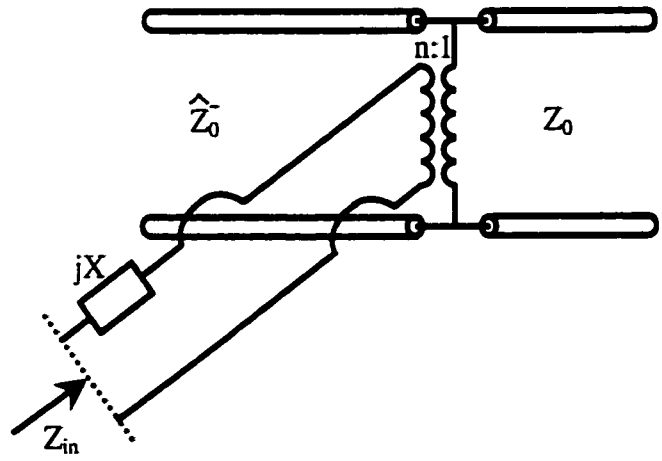

Figure 7.9: An equivalent circuit for the side-launching waveguide transition.

To determine the turns ratio n, we must obtain an expression for $\bar{J}_s$, the current existing on the loop. In Figure 7.10 below, the schematic diagram of Figure 7.7 is given with the addition of a few key dimensions to aid in our description of $\bar{J}_s$.

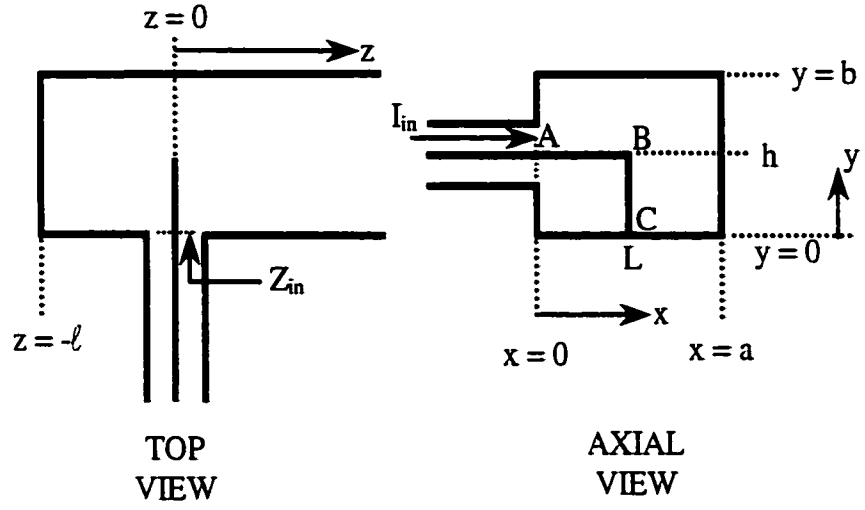

Figure 7.10: Top and axial views of a coax-to-waveguide feed that utilizes magnetic field coupling via a side-launching loop.

We divide the probe into sections AB and BC corresponding to the $\hat{x}$ and $\hat{y}$ components of the probe (and thus current) respectively. We consider the case in which the current is assumed to be cosinusoidal.

For section AB,

$$\bar{J}_{AB} = \begin{cases} \hat{x}\cos(k(L+h-x))\delta(y-h)\delta(z) & 0 \le x \le L \\ 0 & \text{otherwise} \end{cases} \qquad [7.33]$$

and for section BC,

$$\bar{J}_{BC} = \begin{cases} \hat{y}\cos(ky)\delta(x-L)\delta(z) & 0 \le y \le h \\ 0 & \text{otherwise} \end{cases} \qquad [7.34]$$

where $k = 2\pi/\lambda$ is the wavenumber of free space.

The dominant mode (TE_{10}) vector, in the case of a rectangular waveguide of cross-section dimensions as depicted in Figures 7.10 (a>b), may be expressed as follows:

$$\hat{e}_0 = \frac{\bar{E}_{t,i=0}}{V_0} = \hat{y}\frac{E_t \sin\left(\frac{\pi x}{a}\right)}{bE_t} = \hat{y}\frac{1}{b}\sin\left(\frac{\pi x}{a}\right).$$

A discussion of mode voltages, currents and vectors may be found in [87] (pp. 71-72 and 383-388) and [88] (pp. 316-319).

Now,

$$I_{in} = \left|\bar{J}_s\right\|_{x=0,y=h,z=0} = \cos[k(L+h)] \,. \qquad [7.35]$$

Therefore from equation [7.28], we may write that

$$n^2 = \frac{1}{\cos^2[k(L+h)]}\left(\int_s \left(\bar{J}_{AB} + \bar{J}_{BC}\right) \bullet \hat{e}_0 ds\right)^2 .$$

We note that the current in arm AB, $\bar{J}_{AB}$, does not interact with the dominant mode defined by the mode vector $\hat{e}_0$ (i.e. $\bar{J}_{AB} \bullet \hat{e}_0 = 0$). Therefore the expression for the turns ratio simplifies as follows:

$$n^2 = \frac{1}{\cos^2[k(L+h)]}\left(\int_s \bar{J}_{BC} \bullet \hat{e}_0 ds\right)^2 . \qquad [7.36]$$

The question may arise as to with which modes the current in arm AB would interact. $\bar{J}_{AB}$ creates an electric filed in the $\hat{x}$ direction. Modes having components in such a direction would be TE_{nm} where $m \neq 0$, and all TM modes. Since such modes are at best evanescent in the frequency range of interest, their effect would only be felt in terms of the reactive component of the input impedance, and will be considered shortly. Substituting [7.34] into [7.35] and taking the square root, we are left with the following:

$$n = \frac{1}{\cos[k(L+h)]} \int_0^a \int_0^b \hat{y}\cos(ky)\delta(x-L)\delta(z) \bullet \hat{y}\frac{1}{b}\sin\left(\frac{\pi x}{a}\right)dxdy .$$

Since we are integrating in the z = 0 cross-section, δ(z) in effect drops out of the equation. The integration with respect to x will also be conveniently evaluated due to the δ(x-L) factor. Finally the evaluation range of the y integration is reduced to 0 to h – the extent of the BC arm. This leaves us with:

$$n = \frac{1}{b}\frac{1}{\cos[k(L+h)]} \int_0^a \sin\left(\frac{\pi x}{a}\right)\delta(x-L)dx \int_0^h \cos(ky)dy$$

which may be evaluated as follows:

$$n = \frac{1}{b}\frac{\sin\left(\frac{\pi L}{a}\right)}{\cos[k(L+h)]}\left(\frac{1}{k}\sin(ky)\right)\Big|_0^h$$

or,

$$n = \frac{1}{b}\frac{\sin\left(\frac{\pi L}{a}\right)}{k\cos[k(L+h)]}(\sin(kh)) .$$

Finally we find that

$$n^2 = \frac{1}{b^2}\left[\frac{\sin\left(\frac{\pi L}{a}\right)\sin(kh)}{k\cos[k(L+h)]}\right]^2 . \qquad [7.37]$$

From equation [7.29] we find that

$$Z_{in} = \frac{1}{b^2}\left[\frac{\sin\left(\frac{\pi L}{a}\right)\sin(kh)}{k\cos[k(L+h)]}\right]^2 \left[Z_0 \sin^2(\gamma_i \ell) + jZ_0 \frac{1}{2}\sin(2\gamma_i \ell)\right]$$

$$+ \frac{1}{I_{in}^2}\sum_{i\neq 0}\left(\int_s \bar{J}_s \bullet \hat{e}_i ds\right)^2 \frac{Z_i}{2} . \qquad [7.38]$$

To utilize [7.38] we must evaluate the variables that comprise the equation. Since we are considering a frequency range in which the dominant mode is propagating

$$\gamma_0 = j\beta_0 = jk\sqrt{1-\left(\frac{f_{c0}}{f}\right)^2} ,$$

where, assuming free space to be the dielectric filling the waveguide, the wavenumber k is given by

$$k = \omega\sqrt{\varepsilon_o \mu_o} .$$

The cutoff frequency of a rectangular waveguide is given by:

$$f_c = \frac{1}{2\sqrt{\varepsilon_o \mu_o}}\sqrt{\left(\frac{m}{a}\right)^2 + \left(\frac{n}{b}\right)^2} ,$$

which for the dominant mode (TE_{10}, i.e. m = 1, n = 0) is simplified to reveal that

$$f_{c0} = \frac{1}{2a\sqrt{\varepsilon_o \mu_o}} .$$

The characteristic wave impedance of the dominant mode when $f > f_{c0}$ is:

$$Z_0 = \frac{\eta}{\sqrt{1-\left(\frac{f_{c0}}{f}\right)^2}} ,$$

where η is the characteristic wave impedance in free space $\eta = \sqrt{\mu_o/\varepsilon_o} \approx 377\ \Omega$.

For the evanescent modes (ie. $f < f_{ci}$),

$$\gamma_i = \alpha_i = k_{ci}\sqrt{1-\left(\frac{f}{f_{ci}}\right)^2}$$

where the cutoff wavenumber, k_c, is given by

$$k_{ci} = 2\pi f_{ci}\sqrt{\varepsilon_o \mu_o} \ .$$

The characteristic wave impedance of the i^{th} mode (again evanescent as $f < f_{ci}$) may be expressed as follows:

$$Z_i = j\frac{\eta}{\sqrt{\left(\frac{f_{ci}}{f}\right)^2 - 1}} \ .$$

We now plot, in Figure 7.11, the input resistance and input reactance of the coax-to-waveguide transition as a function of loop distance to the backshort (i.e. ℓ is varied while keeping all other geometrical parameters constant). The chosen frequency is 94 GHz which is within single-mode frequency range of the waveguide. The chosen parameters are as follows, a = 2540 μm, b = 800 μm, and L = 1270 μm (i.e. L = a/2). *It is important to note that the results in Figure 7.11 are arrived at considering only dominant mode propagation.* Having completed a "first-order" look at the input impedance of the coax-to-waveguide transition as a function of the distance of the loop to the backshort, we turn to full-wave analysis using HFSS to corroborate our results.

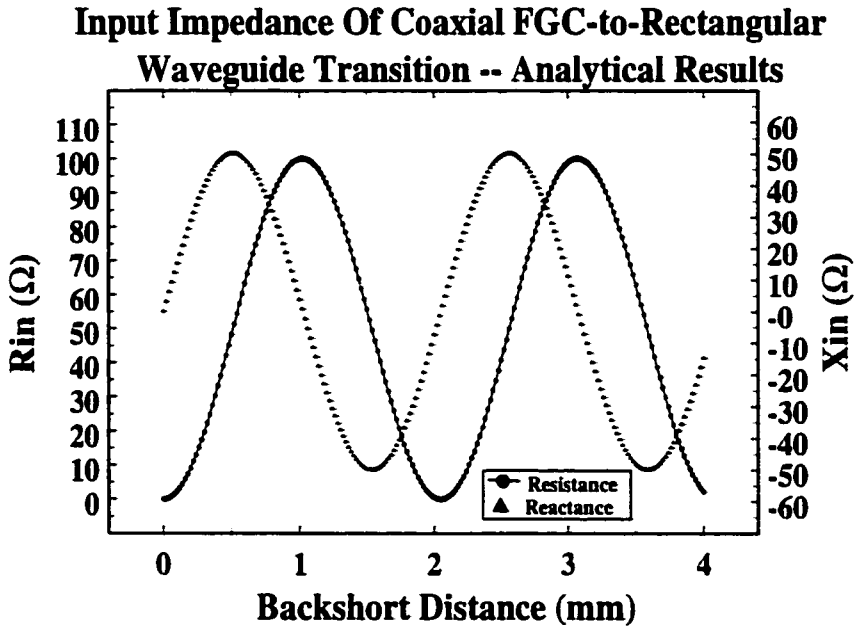

Figure 7.11: The predicted input resistance of the coax-to-waveguide feed versus loop distance from the backshort for an assumed cosinusoidal current distribution. Only the dominant mode is considered.

7.2.3: Simulated Results – Coaxial FGC-to-Rectangular Waveguide Transition

Full wave simulations of the coaxial FGC-to-waveguide transition (see Figures 7.4 and 7.5 for details) were accomplished with HFSS. The loop is extended through the narrow wall as in Figure 5.7 to a distance of a/2. A plot of the cross-section is given in Figure 7.12 below.

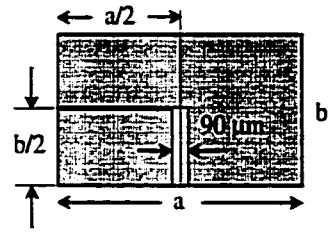

Figure 7.12: Axial view of probe used for the full-wave results given in Figure 7.13.

Figures 7.13 and 7.14 are plots of the input resistance and reactance at 94 GHz versus probe distance to the backshort (i.e. "ℓ" in Figure 7.6) respectively. Included in the plots are the analytical results of Figure 7.11. The full-wave results in these plots were constructed by simulating the s-parameters of the structure for each "ℓ" (from ~0.5 mm to 4 mm in steps of 0.1 mm), deembedding along the FGC line to the "feed point," and using the magnitude and phase of the deembedded reflection coefficient, Γ_{in}, in the following equations:

$$R_{in} = Z_o \frac{1-\left(\mathrm{Re}[\Gamma_{in}]\right)^2-\left(\mathrm{Imag}[\Gamma_{in}]\right)^2}{\left(1-\left(\mathrm{Re}[\Gamma_{in}]\right)\right)^2+\left(\mathrm{Imag}[\Gamma_{in}]\right)^2}$$

and,

$$X_{in} = Z_o \frac{2\mathrm{Imag}[\Gamma_{in}]}{\left(1-\left(\mathrm{Re}[\Gamma_{in}]\right)\right)^2+\left(\mathrm{Imag}[\Gamma_{in}]\right)^2}.$$

These equations may be obtained by algebraic manipulation of the following relation in which Z_o refers to the impedance of the feed line:

$$Z_{in} = Z_o \frac{1+\Gamma}{1-\Gamma}.$$

Figures 7.13 and 7.14 demonstrate rather good qualitative agreement between the full-wave results and those obtained with our simplified analytical model based on the stationary form of the input impedance. Quantitatively, there exists a maximum error of ~10% between the simulated and analytical results for the input resistance and ~60% for the input reactance. It is quite interesting to note that there is a vertical shift in the reactance curves between the HFSS results and those of the analytical model. While the analytical results are centered at zero, the HFSS results are centered at approximately j14

Ω. This difference between the HFSS simulations and the analytical model are perhaps most visually understood by viewing the "reactive offset" in the Smith chart of Figure 7.15. Factors such as the simplified current assumption and the neglecting of both evanescent modes in the guide (and thus their contribution to the reactive component of the input impedance) and the parasitics that exist at the feed location, contribute to the differences between the analytical model and full-wave simulation. While the above analysis is helpful in obtaining a better understanding of the operation of the magnetically coupled transition, full-wave simulation is necessary for obtaining precise matching and will be used throughout the remainder of this chapter.

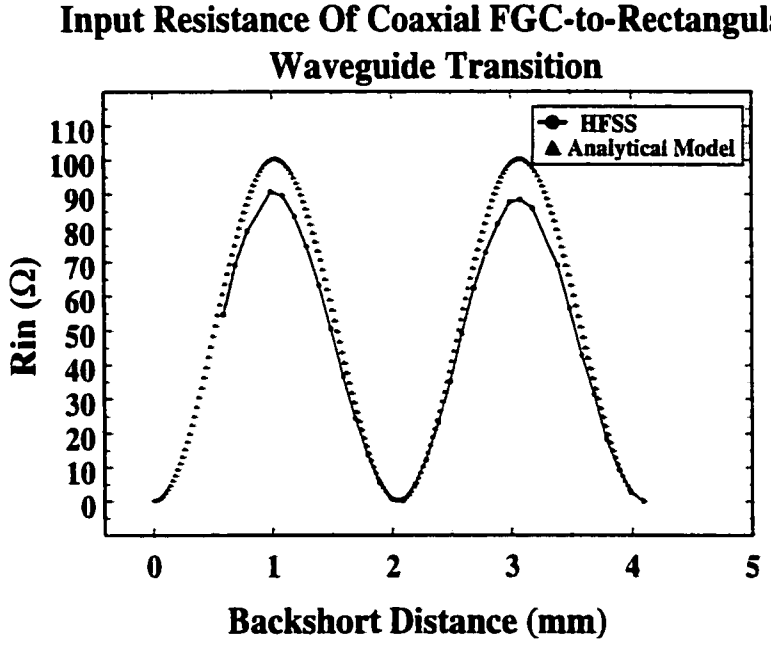

Figure 7.13: A comparison of the simulated (HFSS) and analytical results for the input resistance of the coaxial FGC-to-rectangular waveguide transition.

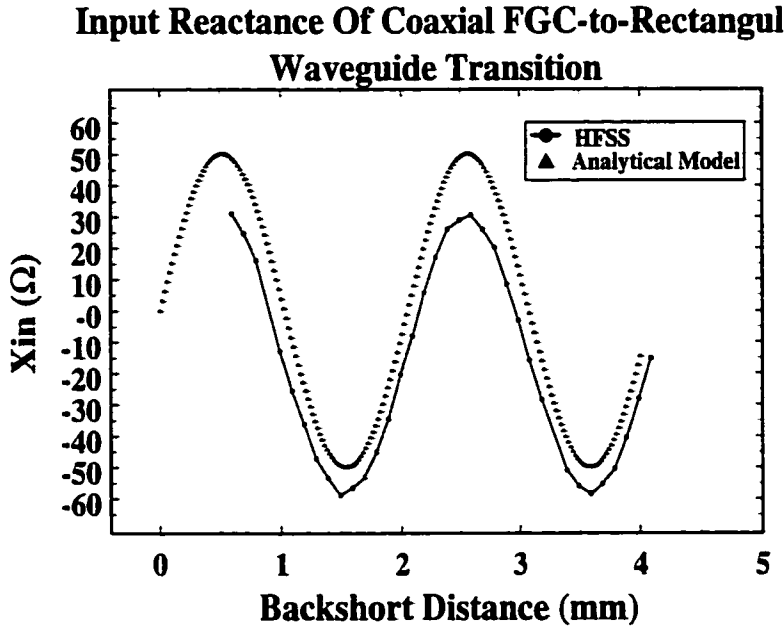

Figure 7.14: A comparison of the simulated (HFSS) and analytical results for the input reactance of the coaxial FGC-to-rectangular waveguide transition.

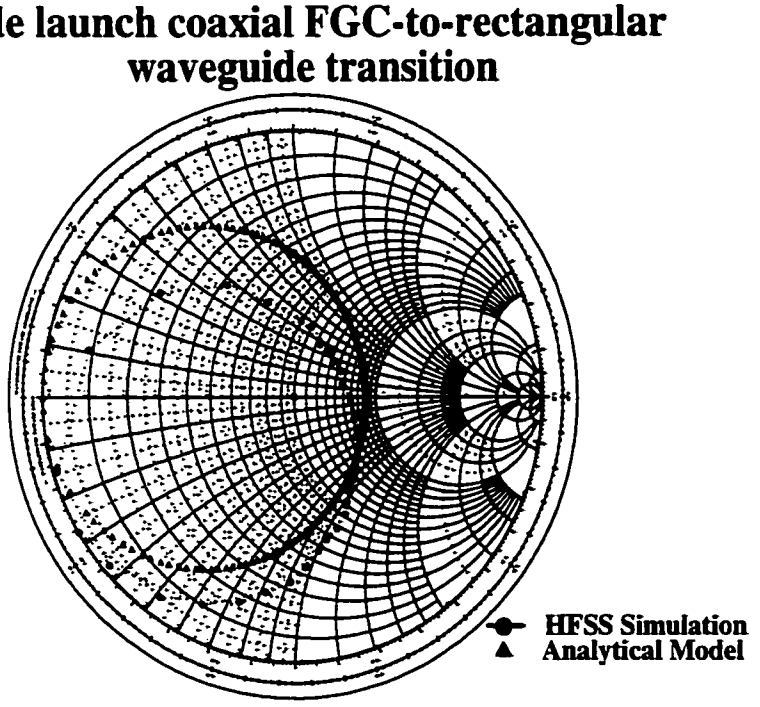

Figure 7.15: Smith chart revealing the "reactive offset" of the analytical model as evidenced by the relative rotation of the two impedance circles.

7.2.4: Magnetic Coupling to A Micromachined Waveguide

As a means to determine the fabrication complexities and to develop a fabrication protocol for constructing the magnetically coupled FGC line-to-micromachined waveguide transition, the end-launch structure of Figure 7.3 was considered first. It was determined that the undercutting phenomenon that occurs during anisotropic etching of convex corners in (001) silicon restricts the minimum ledge width that can be obtained while maintaining 90° corners. Using <010> compensation (see section 3.1.1), the minimum ledge thickness is $\sim 4\,(\text{etch depth})/\sqrt{2}$. This would make the ledge nearly as wide as a standard waveguide and thus is undesirable. Since corner compensation is not an issue in the side-launch structure of Figure 7.16 (also shown in Figure 7.2), the depicted architecture was studied.

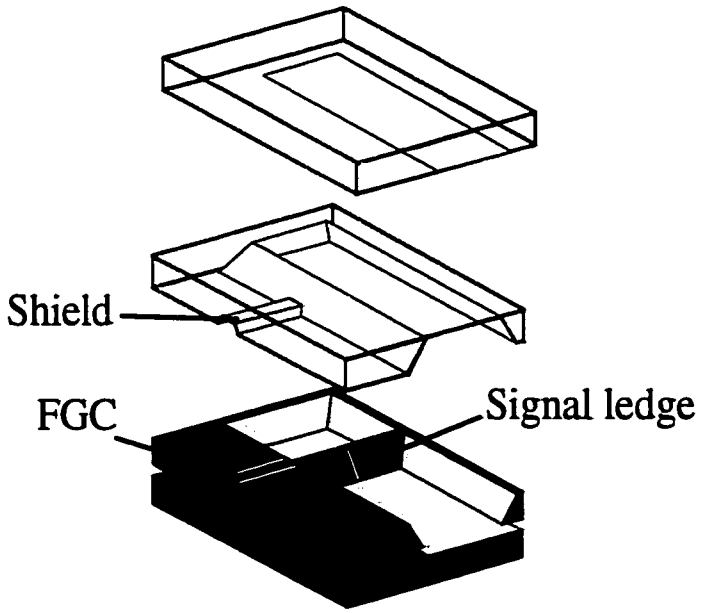

Figure 7.16: "Exploded" view of the originally proposed side-launch transition.

The micromachined side-launch architecture differs in two key ways from the ideal side launch structure studied in the analytical portion of this chapter. First, the feed line

in the micromachined version is not perfectly shielded, having only a capping shield. Second, in the idealized structure there is no need for the signal ledge that protrudes into the micromachined waveguide.

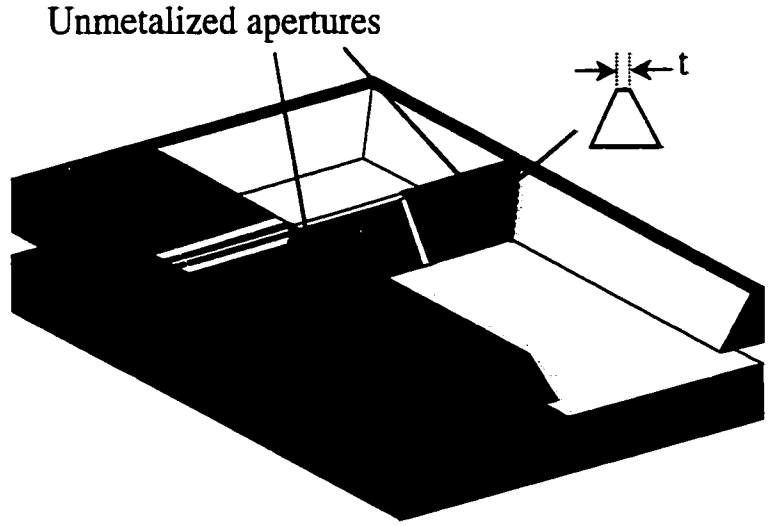

Figure 7.17: A portion of the micromachined side-launch transition illustrating the apertures that cannot be metalized.

An extensive HFSS study was devoted toward developing a suitable transition based on the realizable geometry. As it turns out, the two triangular apertures where the signal ledge meets the waveguide walls allow the signal to be coupled out of the guide and into the substrate. These triangular regions are pointed out more clearly in Figure 7.17.

Full wave simulations were run on the silicon micromachined hexagonal waveguide to determine the extent to which radiation from the slots played in the demise of the transition. Cases were run assuming an aperture with t = 50 μm which made the aperture base 616 μm (a W-band waveguide was modeled; a = 2260 μm, b = 800 μm c = 283 μm – see Figure 6.1). The waveguide was fed at its two ends with the dominant TE mode.

It was found that the unmetalized section of the waveguide caused only a small degree of loss (waveguide insertion loss of –0.029 dB at 94 GHz) when the ledge that causes

them in the realized version were not included. By including the ledge as well as the unmetalized apertures, the simulated insertion loss was –1.15 dB – an unacceptable amount. In light of the difficulties presented above, the magnetically coupled transition was abandoned and an E-plane transition was developed.

7.3: Electric Field Coupling

7.3.1: Micromachined Probe, Conventionally Machined Waveguide Version

An FGC line-to-rectangular waveguide transition has been demonstrated by Tentzeris [85] and converted to a fully micromachined version in this study. A sketch of the initial structure used to convert to the fully micromachined version may be found in Figure 7.18. In this figure, a micromachined piece of silicon is placed in the E-plane of a conventionally machined rectangular waveguide. An FGC transmission line and patch are printed on the piece of silicon with the patch aligned with the E-field of the waveguide's dominant mode. A back-to-back transition of this structure was demonstrated at K-band [89] with the measured results presented in Figure 7.19.

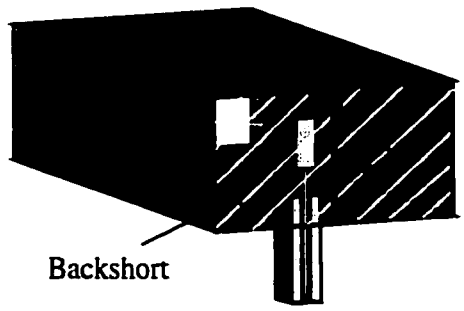

Figure 7.18: Sketch of the excitation of a rectangular waveguide with a silicon micromachined probe.

Measurement of the back-to-back transition was performed using an HP 8510C network analyzer and a pair of HP Q281A coaxial waveguide adapters. The return loss is better than –10 dB across the entire waveguide band, with the majority of the band exhibiting better than –20 dB performance. The insertion loss presented in the figure is that calculated after de-embedding both the loss of the coaxial adapters and that of the FGC line itself. The de-embedded loss of the FGC line was measured through an on-wafer calibration protocol using *Multical* [58]. Further simulation, not shown here, indicate that simple scaling can be used to produce similar transitions for operation in higher-frequency bands. As mentioned previously however, conventional machining of metal waveguides and their fixtures for circuit operation at higher frequencies becomes increasing difficult and thus costly. For this reason, a silicon micromachined waveguide / FGC line combination was developed.

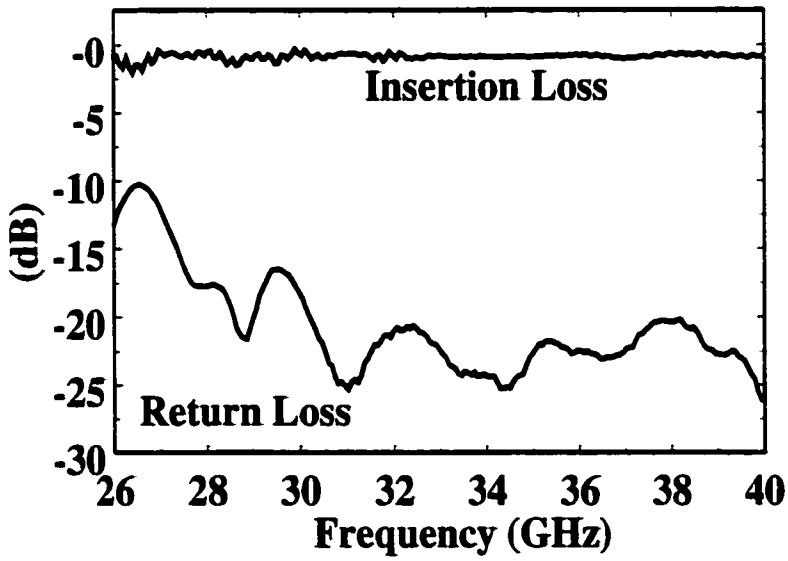

Figure 7.19: Measured results [89] of a back-to-back FGC line-to-rectangular waveguide transition. The FGC line and patch were printed on micromachined silicon and the waveguide conventionally machined.

7.3.2: Fully Micromachined Transition

A schematic diagram of the proposed transition from an FGC line to a silicon diamond waveguide is given in Figure 7.20. As demonstrated in Chapter 6, the waveguide is formed in a "split-block" manner by combining two silicon wafers, each which has been anisotropically etched to the depth of a/2. The top wafer is suggested in outline in the figure. An additional groove has been etched into the bottom half of the guide, with the groove serving to support a probe; a similar groove in the top wafer is etched to act as a shield for the probe. Wet anisotropic etching of the two additional grooves would be problematic due to the severe undercutting that occurs at convex corner during such etching [90] – thus compromising the dimensional accuracy of a wet-etched structure. Instead, DRIE was used to etch the additional grooves.

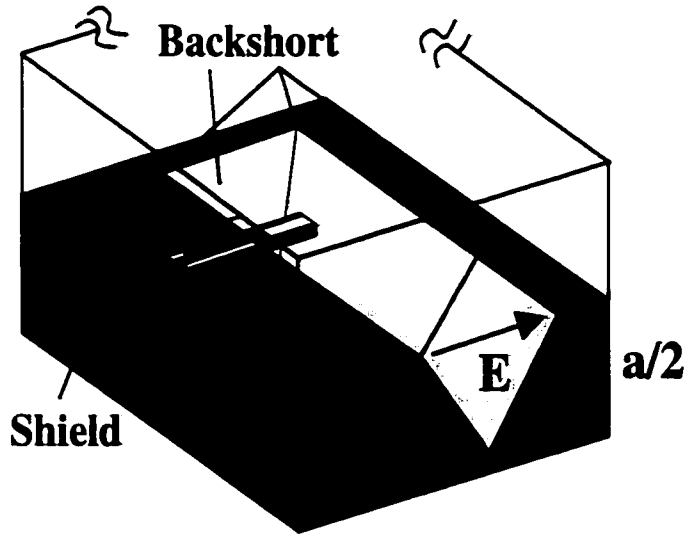

Figure 7.20: Sketch of a fully micromachined FGC-to-waveguide transition.

As conceived in the figure, the probe is rotated by 90° with respect to its position as depicted in Figure 7.18. Figure 7.21 shows this rotation more clearly. Full-wave simulation results have revealed that such a probe rotation, when made with a transition

to a rectangular guide, though requiring different matching parameters, nevertheless allows for operation across the full band of the waveguide. The 90° rotated configuration is preferred from a fabrication standpoint in the fully micromachined version.

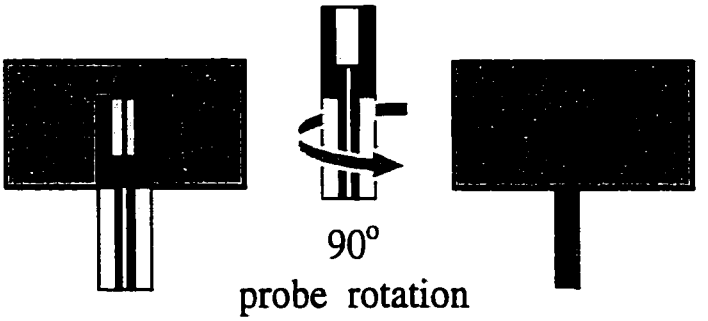

Figure 7.21: Illustration showing the 90° rotation of the probe for implementation of the fully micromachined transition.

Full-wave simulation results of the rotated transition to the silicon diamond waveguide are given in Figure 7.22, with the relevant dimensions of the simulated transition structure given in Figure 7.23. A single transition is found to exhibit a −15dB bandwidth of ~ 12.5 % and a −10 dB bandwidth greater than 20%. The bandwidth of the transition is considerably less than that with a rectangular waveguide and is attributed to the variation in waveguide impedance as explained below.

The dimensions of the standard rectangular waveguide (b = a/2) are chosen to establish a 2:1 frequency range of single-mode operation. The single-mode bandwidth of the silicon diamond guide is significantly less, being only approximately 1.33:1 as discussed in chapter 6. The advantages of a larger single-mode bandwidth for the rectangular guide are manifested in at least two ways.

The impedance of a given mode in a waveguide becomes purely real at cutoff and decreases with increasing frequency in the case of the dominant TE mode, approaching a value of the characteristic impedance of the medium that fills the guide. By operating a

waveguide well above its cutoff frequency, a nearly constant value of impedance is obtained. Since the single-mode bandwidth of the diamond waveguide is substantially less than that of its rectangular counterpart, we expect a greater variation of impedance as we cannot operate too far from its dominant mode cutoff frequency lest we overmode the guide. In fact, while the impedance of the appropriate rectangular waveguide varies only by a factor of 1.1 from 90-100 GHz, that of the silicon diamond counterpart varies by approximately a factor of 2.1.

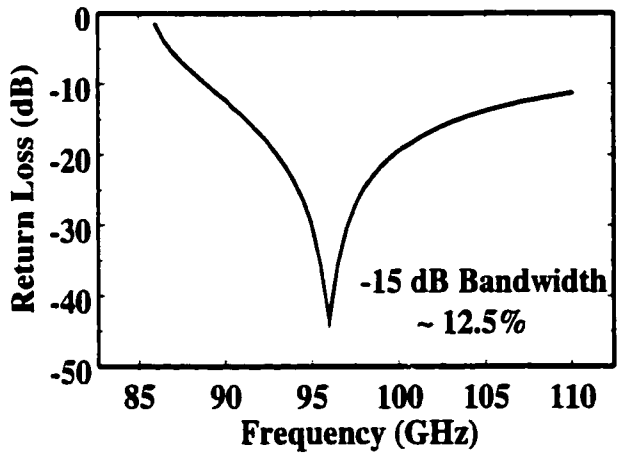

Figure 7.22: Simulation results of a single FGC-to-silicon diamond waveguide transition.

Operating a waveguide well above cutoff offers reduced loss as well. Not surprisingly then, the loss of the silicon diamond waveguide as determined with HFSS was found to be somewhat larger that that of a rectangular waveguide. In the simulation, a gold metalization of several skin depths was assumed and the loss of the diamond waveguide found to be a factor of 1.6 (in dB per guided wavelength) above that of the rectangular waveguide at 110 GHz. A means to increase the bandwidth of the silicon diamond waveguide through use of a fin-line, and thus improve its attenuation and single-mode

characteristics, is described in [82]. Regardless, the FGC-to-Si diamond waveguide transition should be suitable for applications that require bandwidths on the order of 10%.

Fabrication Details

To investigate the possibilities of the FGC-to-silicon diamond waveguide E-plane transition, a back-to-back structure consisting of input and output FGC probes feeding a single diamond waveguide was fabricated. The starting material for the top and bottom halves of the waveguide was (001)-oriented high resistivity (> 1kΩ-cm) silicon wafers. Since the waveguides and the transition were designed for operation within W-band (i.e. 75-110 GHz), the *a* dimension of the waveguide (see Figure 7.20) was chosen to be that of a conventional WR-10, specifically 2.54 mm. To realize the waveguide in the split-block method suggested in Figure 7.20, and to provide adequate mechanical stability of the etched structure, a wafer thickness of 2 mm was chosen. A thermal oxide approximately 8000 Å thick was grown on the bare wafers to serve as a masking layer.

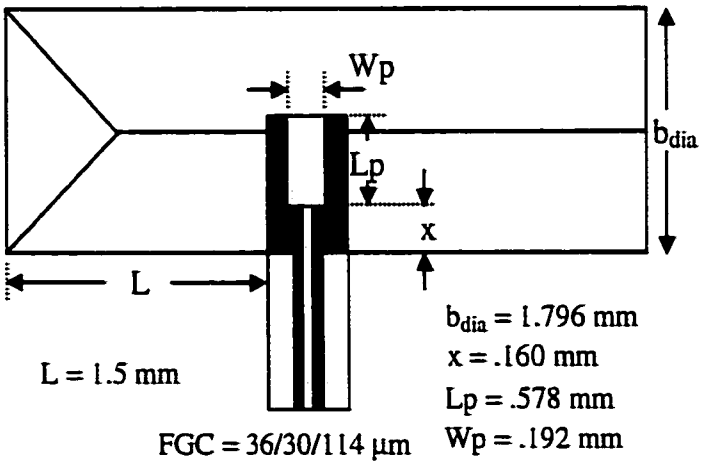

Figure 7.23: Dimensions of the modeled transition.

Rectangular apertures for subsequent anisotropic etching of the waveguide halves were opened in the oxide via standard photolithography and chemical etching using buffered hydrofluoric acid. The remaining oxide then served as a masking layer for wet anisotropic etching of the waveguide groove using 25% tetramethyl ammonium hydroxide (TMAH). TMAH was chosen due to the etchant's ability to provide extremely smooth sidewalls. Unfortunately, the (100)/(111) selectivity is not as great with TMAH as it is with other wet anisotropic etchants such as potassium hydroxide and thus mask undercutting had to be taken into account. The etch rate was approximately 20 μm/hour and the (100)/(111) selectivity taken to be 10/1. After wet anisotropic etching, the oxide mask was stripped.

Photoresist was then used as a masking layer for etching of both the cradles (i.e. additional groove on the bottom wafer) used to hold the micromachined probes and the transmission line shields (etched on the top wafer). Applying photoresist to micromachined structures via typical wafer spinning is a troublesome proposition in that the applied resist is not uniform. A non-uniform resist coating leads to difficulty in properly resolving features photolithographically and to providing adequate protection to underlying layers where photoresist is to serve as an etch mask. A means to employ electrodeposition of photoresist was discussed extensively in Chapter 4 and largely mitigates the problems encountered in resist spinning on micromachined structures. In future iterations of the work presented here we intend to introduce the electrodeposited resist into our fabrication process, but have for the present have used conventional wafer spinning to apply photoresist. Roughly 7 μm of resist served as the etch mask for deep reactive ion etching (DRIE).

The DRIE system used is a Surface Technology Systems (STS) tool that employs a time-multiplexed process to etch silicon (see section 3.1.2). The process utilized in this study consisted of a 7 second passivation step using C_4F_8 and a 13 second etch step using SF_6 which yielded profiles approximately 5° from vertical. The etch rate, which depends upon the exposed area and pattern dimensions, was approximately 6 μm/min for the structures developed here and thus etching a depth of 100 microns required approximately 17 minutes of cycling through the passivation and etching steps.

After deep etching, the protective resist layer was removed using acetone and the wafer cleaned in a "Piranha" etch consisting of a 1:1.2 mixture of 30% hydrogen peroxide and sulfuric acid for 10 minutes. The wafer was then coated with a sputtered bilayer of 750 Å of titanium which served as an adhesion layer, followed by a 1.6 μm thick layer of gold. A scanning electron micrograph of the micromachined structure (prior to metalization) is given in Figure 7.24.

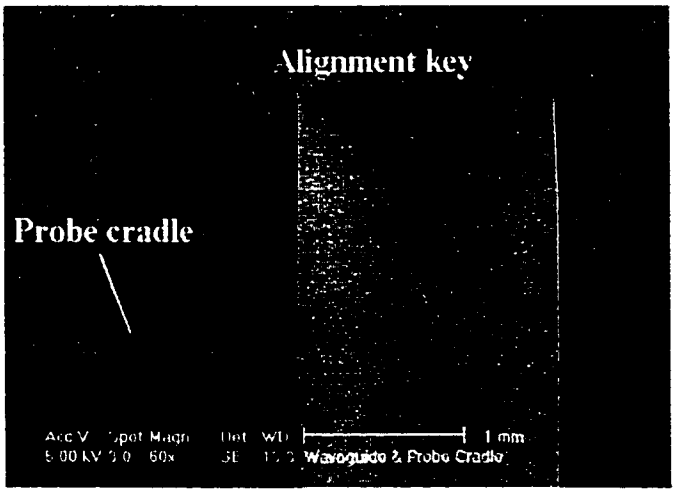

Figure 7.24: Scanning electron micrograph of the bottom half of the micromachined waveguide in plan view.

It is interesting to note that the alignment key was not entirely etched as a small silicon island exists in one corner of the key. This small island is due to incomplete removal of the photoresist mask prior to deep etching and is evidence of the potential difficulties arising from spinning resist on micromachined surfaces. Another deleterious effect of wafer spinning of the resist is evident in the thin etched groove that surrounds the waveguide. The resist tends to be quite thin on the immediate edge of a micromachined cavity or groove, a problem that is exacerbated by reflow occuring during resist softbaking. To solve these problems, electrodepositable may be used.

The FGC probes used in the fully micromachined module were fabricated using 100 μm thick high-resistivity (ρ>2000 Ω-cm) bare silicon wafers. The metalization pattern was formed on the top surface using a trilayer of chromium (500 Å), gold (0.9 μm), and Ti (500 Å) in a standard lift-off process. The etching pattern was formed on the frontside of the wafer and properly registered to the top metalization. The patterned wafer was then mounted on a carrier wafer and micromachined using the STS system until the 100 μm wafer was etched entirely through. The probes were then released in acetone and thoroughly cleaned with hot PRS-2000. The Ti layer was finally etched, thus completing probe fabrication. A schematic drawing of an etched FGC probe is given in Figure 7.25.

Arm-like appendages were developed on the probes (the probe cradles on the lower waveguide wafer had the identical arms) to ensure that the probes would not shift when placed in the probe cradle. Finally Figure 7.26 displays a photomicrograph of a probe that has been inserted into the bottom half of a waveguide. Again, incomplete etching of the alignment key is evident. The pits visible in the lower left-hand corner of the micrograph were wet etched in TMAH and were introduced to accommodate NIST

traceable glass microspheres. Similar pits were etched in the top half of the guide thus allowing simple alignment of the top and bottom halves of the waveguide.

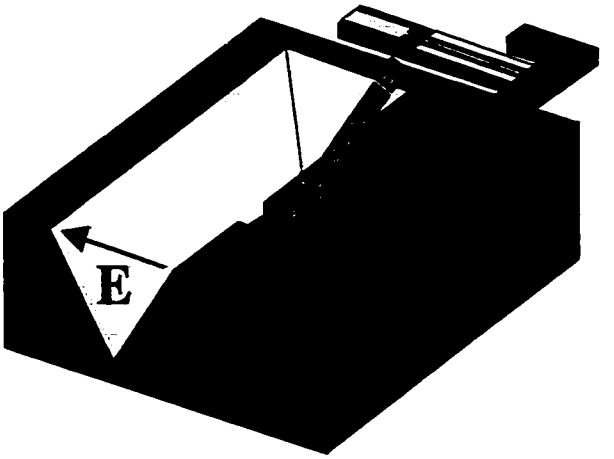

Figure 7.25: Schematic diagram of an etched FGC probe and probe cradle.

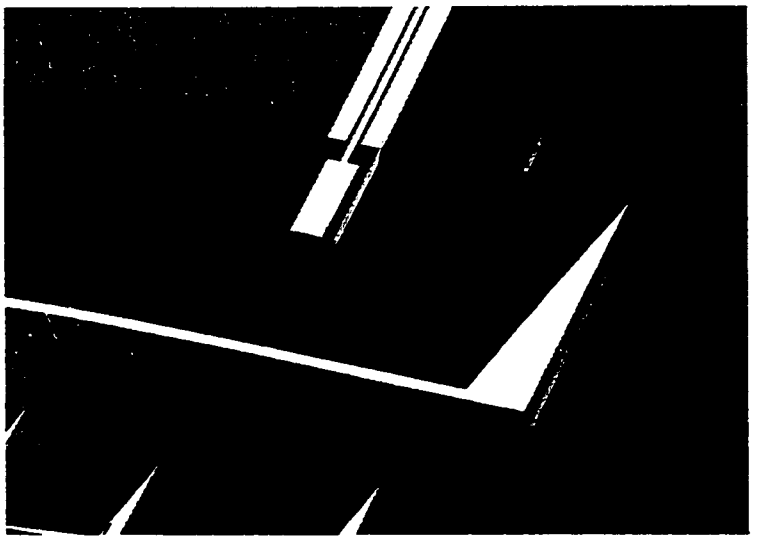

Figure 7.26: A scanning electron micrograph of the bottom half of the micromachined waveguide with an FGC probe inserted into its cradle.

Measured Results

A back-to-back transition consisting of input and output FGC lines was measured in W-band using an HP 8510C vector network analyzer and a set of ground-signal-ground

model 120 GGB Picoprobes. On-wafer calibration was achieved through the use of a TRL protocol. The simulated and measured results of a back-to-back transition are given in Figure 7.27.

The results of Figure 7.27 have been de-embedded to the mouth of the waveguide. The assumed loss due to propagation in the waveguide has been removed from the measured data. This was done by simulating the waveguide in HFSS using an assumed metal conductivity of 5×10^6 $(\Omega\text{-m})^{-1}$ (see chapter 6). The simulation results shown in Figure 7.27 are for the lossless case.

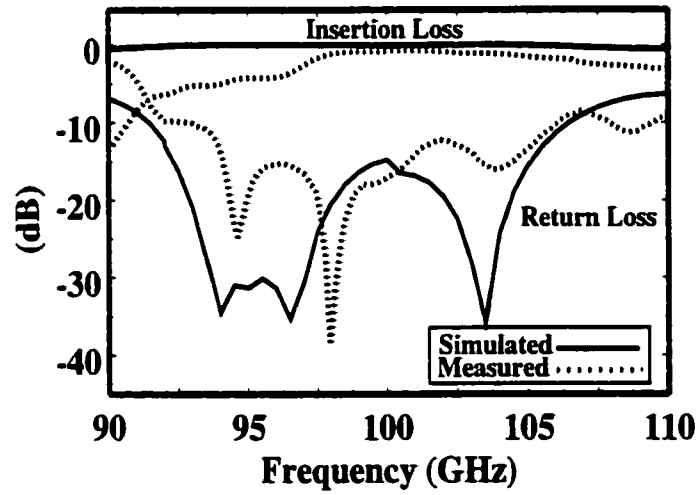

Figure 7.27: Simulated and measured results of a back-to-back FGC-to-Si micromachined waveguide transition.

The fact that the structure's transmission characteristic does not increase as rapidly as the simulation predicts is due at least in part to the fact that the fabricated waveguide was slightly smaller than designed, thus moving the waveguide's cutoff frequency somewhat higher. Most likely the greatest cause of the difference between measurement and simulation rests in the fact that the halves of the measured structure were clipped together

and not bonded. Modeling of the structure with imperfect bonding is rather difficult as precise knowledge of the location and size of gaps between the wafers is unknown. Several comments with regard to the performance of the transition are nevertheless in order.

The −10dB bandwidth of the back-to-back transition is approximately 13%, roughly what is expected. Between 98 and 102 GHz, the transition performs reasonably well with a measured insertion loss per transition less than 0.45 dB. It is believed that the performance of the transition will be significantly improved with elimination of such imperfections as the thin etched groove that surrounds the guide and through use of thermo-compression bonding of the waveguide halves.

7.4: Conclusions

A theoretical model of a transmission line-to-waveguide transition was investigated for the case of side-launching magnetic coupling. Due to the added complexities that realizable geometries present, full-wave simulation was found necessary to develop efficient transitions. Development of a suitable side-launching magnetic-coupled micromachined waveguide transition was hindered by substrate coupling through apertures inherent in the waveguide structure. For this reason an E-plane scheme was investigated. The initial fabricated design exhibited an insertion loss of less than 0.45 dB from 98 to 102 GHz. Bonding of the waveguide halves is expected to markedly improve the performance of the transition.

The use of micromachining for THz systems has been investigated for nearly a decade; a thorough review of these efforts is found in [91]. At the time of this writing however, the author knows of only one example of a fully micomachined waveguide

transition other than that presented herein. In that work [92], a 585 GHz Schottky mixer is demonstrated using micromachined silicon and SU-8. The performance of the micromachined version was found to be equivalent to that obtained through conventional machining of the waveguide block.

CHAPTER 8

SUMMARY AND RECOMMENDATIONS FOR FUTURE WORK

8.1: Summary

Silicon micromachining has been investigated in both the development a of novel 3D packaging technology and in demonstrating 0.1 THz waveguides and waveguide transitions. Electrophoretic deposition using PEPR 2400 was demonstrated to be an enabling technology for simultaneously patterning features on the various facets of micromachined silicon. Using this technique, a multilevel transition characterized by an average loss of only 0.08 dB per transition was demonstrated up to 40 GHz. A deep reactive ion etched three-via transition has been proposed with initial simulation results suggesting that such a structure could challenge existing three-via micromachined structures and allow for simpler fabrication.

Diamond shaped hollow waveguides that evolve naturally from the {111} sidewalls of anisotropically etched silicon have been demonstrated at W-band frequencies with a measured loss of 0.135 dB/λ_g at 110 GHz. As measured, the performance of the waveguide was not limited by its inherent characteristics, but rather by imperfect interconnection to the input and output feeds. WR-3 waveguides have been fabricated using deep reactive ion etching, but have not as yet been measured due to the lack of a suitable testing facility at Michigan.

A fully micromachined transition from an FGC line to a silicon diamond waveguide was developed at W-band. A loss of less than 0.45 dB per transition from 98-102 GHz (0.25 dB at 100 GHz) was demonstrated. It is anticipated that the performance of the transition will be significantly improved in terms of operation bandwidth (a bandwidth of greater than 10% is expected) through use of thermo-compression bonding.

8.2: Recommendations for Future Work

8.2.1: Micromachined Packaging and Electrodeposition of Photoresist

While the results demonstrated herein are promising with regards to the development of efficient packaging structures, several caveats are in order. Improvement in the developed process of electrophoretic deposition of PEPR 2400 photoresist and subsequent photolithographic patterning and metalization is necessary. Initial results of the liftoff process developed in this investigation were quite successful. With aging of the resist and with subsequent batches of resist, the process window has drifted somewhat. Even the yield over a single wafer is presently not acceptable for industrial applications. It is felt by the author that another investigation of this technique is warranted.

Several skin depths of circuit metal is often sought in the development of microwave circuits and thus metal layer thickness can become substantial at k-band and below. In such cases, a 1 μm thick lift-off process is not ideal. Rather, a metal plating technique in which metal thickness on the order of 3 μm could be readily established would be preferred. The author found that adhesion between the electrodeposited resist and metal seed layer to be problematic. This finding was corroborated by a representative at

Shipley, the manufacturer of PEPR 2400. It seems then that some novel means to improve adhesion of PEPR 2400 is required. Could this be realized with a copper seed layer or through different deposition conditions? Would the resist be more stable in alternate metal plating baths? These are questions that could be investigated.

Even if a robust electrodepositable technique could be established, diffraction will ultimately limit the ability to resolve tiny features at the depths of micromachined cavities using contact printing. PEPR 2400 may have an immediate impact on secondary etching of micromachined structures in which the photoresist could be used as an etch mask. Thus electrodeposition of resist and subsequent deep reactive ion etching could prove to be a powerful combination in developing structures defined by multiple etching steps. Such a combination could be used in the waveguide transition architecture as described in chapter 7. Various "photonic bandgap" may be realized through such a technique as well.

8.2.2: Terahertz Waveguides and Transitions

The development of hollow waveguides in silicon seems an ideal solution to the development of low loss, low cost signal transmission at THz frequencies. Surface roughness of waveguide walls is a significant issue and should be addressed for applications at these frequencies. While traditional anisotropic wet etching yields smooth sidewalls, geometries are limited. In many systems, specifically those in which only straight sections of waveguide are needed, this may not be a problem. In circuitry in which waveguide bends are necessary, techniques such as deep reactive ion etching and laser milling may be necessary. The use of thermal oxidation should be investigated to

reduce the surface roughness of waveguide walls etched through one of the later techniques.

While silicon may prove to be an ideal solution to the development of passive structures at THz frequencies, compound semiconductors such a GaAs are required for active circuitry. Thus the effective combination of passive support and signal distribution with active circuitry is paramount to a successful system. This is a tremendous challenge due to the small wavelength at these frequencies. While the silicon probe was demonstrated to be effective at 100 GHz and may perhaps be pushed to the edge of the submillimeter-wave range, other solutions may be necessary at true THz frequencies. Organic polymer membranes or thinned quartz may be appropriate alternatives.

8.2.3: Silicon Micromachined Power Combining Modules

The development of compact power sources at THz frequencies will require the use of power combining techniques to generate significant power levels. As mentioned in Chapter 1, the state-of-the-art Gunn diodes are capable of producing approximately 1 mW at the edge of the submillimeter range (300 GHz). Diode based multipliers may be used to extend the frequency range of such sources, with efficiency being a critical concern.

A possible power combining architecture using the waveguides and transitions investigated in this dissertation is suggested in Figure 8.1. As conceived in the figure, the module consists of a 2D array of integrated diamond waveguides and horns. Each waveguide is fed with a Gunn diode/frequency multiplier combination through an E-plane transition. A DC network provides the required bias to the individual sources. In such a manner a large number of solid-state devices could be orchestrated using spatial

power combining in free space. Since the module should be limited by the performance of the active and not the passive elements, improvement in the performance of the waveguide transition is needed before moving forward with such a concept.

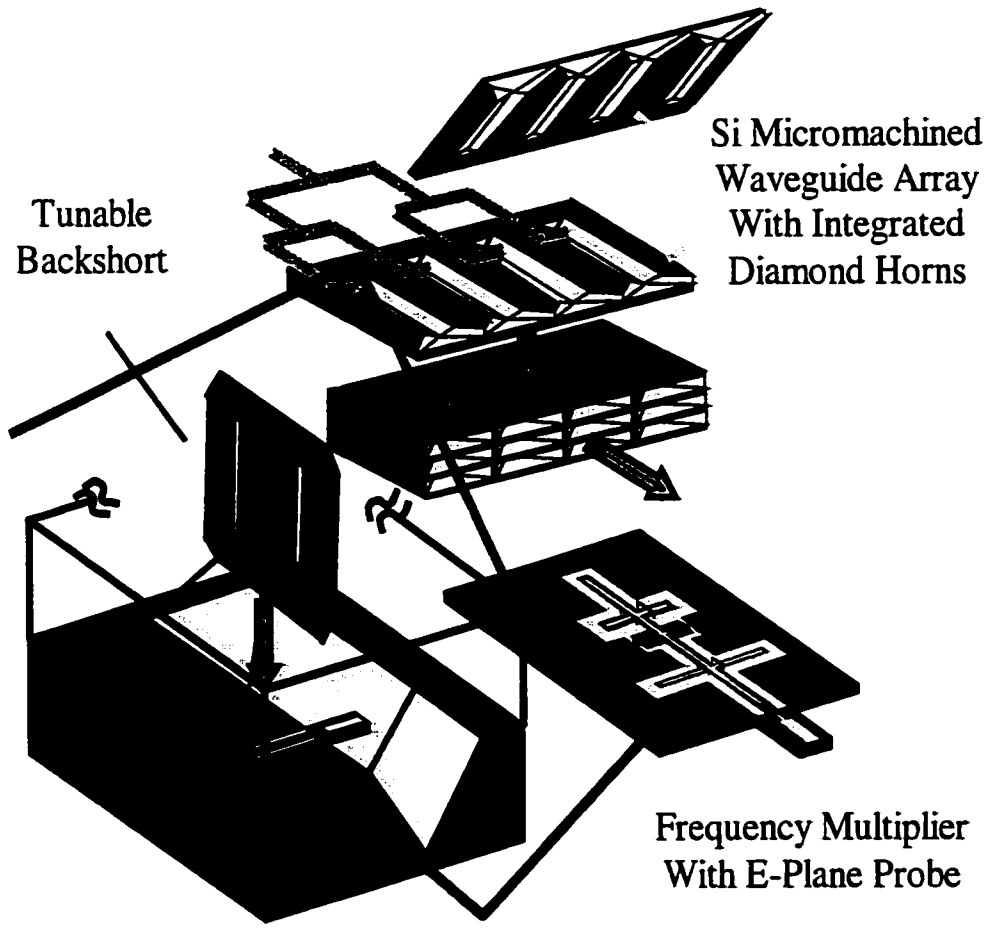

Figure 8.1: A potential silicon micromachined THz power combining module.

APPENDICES

APPENDIX A

DEEP REACTIVE ION ETCHING PROCESS PARAMETERS

A.1 Introduction

A standard "Thru Wafer" recipe was used for all deep reactive ion etching discussed in this dissertation. The user has control of a variety of parameters to adjust etch rate, selectivity and etch profile. The parameters listed below yielded an etch profile ~ 5° from vertical and an etch rate on the order of 5 μm/minute (depending on etching area).

A.2 Process Parameters

- Pump Down Time: 20 seconds
- Gas Stabilization: 30 seconds
- Process Time: user input
- Pumpout Time: 30 seconds
- Order of Etching: passivation first
- Etch Time: 13 seconds
- Passivation Time: 7 seconds
- APC Mode: Manual
- APC Setting: 67%
- Base Pressure: 0.2 mT
- Pressure Trip: 94 mT
- C_4F_8: Flow = 85 sscm; Tolerance = 50 %
- SF_6: Flow = 160 sscm; Tolerance = 50 %
- O_2: Flow = 0 sscm; Tolerance = 5 %
- Ar: Flow = 0 sscm: Tolerance = 5%
- RF Etch Power: 250 W
- Matching: Auto: Match Load = 50 %, Match Tune = 50 %
- Coil Generator: Etch = 800 V, Passivation = 600 V; Tolerance = 50%

APPENDIX B

FABRICATION PROCEDURES

B.1: Introduction

This appendix provides process flow details for fabrication of the various structures detailed in this dissertation. In Section B.2, the process parameters for the various resists used in this work are given. Section B.3 lists two wafer cleaning procedures and B.4 the general anisotropic etching procedure. Section B.5 details the fabrication procedure for realizing the micromachined E-Plane probes described in chapter 7. Section B.6 gives an accounting of the fabrication steps for realizing a waveguide half for use in an FGC-to-micromachined waveguide transition. The simple diamond waveguides of chapter 6 were fabricated in the same manner excepting the deep etching steps.

B.2: Resist Recipes

HMDS Adhesion Promoter

- Spin Speed: Same as for given resist
- Spin Time: 30 seconds

1827

- Spin HMDS as above if on non-metallized surface

- Spin Speed: 3.5 krpm (maximum ramp)
- Spin Time: 30 seconds
- Soft Bake: 105°C hotplate for 1 minute 15 seconds

  (3 minutes for 2 mm thick substrate)
- Exposure: 11 seconds at 20 mW/cm^2
- Develop in DI:351 concentrate (5:1) for 45 seconds
- Hard Bake: 130°C hotplate for 2 minutes

4620

- Spin HMDS as above if on non-metalized surface
- Spin Speed: 4 krpm (maximum ramp)
- Spin Time: 30 seconds
- Soft Bake: 105°C hotplate for 2.5 minutes

  (3 minutes for 2 mm thick substrate)
- Exposure: 30 seconds at 20 mW/cm^2
- Develop in DI:MF 351 concentrate (5:1) for 2 minutes

Resist Thickness ~ 7 μm

5214 (For Metal Liftoff – Image Reversal Process)

- Spin HMDS as above if on non-metalized surface
- Spin Speed: 2.5 krpm
- Spin Time: 30 seconds
- Soft Bake: 105°C hotplate for 1 minute
- Exposure: 4 seconds at 20 mW/cm^2

- Reversal Bake: 130°C hotplate for 1 minute
- Flood Expose: 90 seconds at 20 mW/cm^2

- Develop in AZ327 for 50 seconds

Good for 1 μm metal liftoff

B.3 Wafer Cleaning

"Piranha" Clean

- Pour 1:1.2 mixture of hydrogen peroxide and sulfuric acid (make certain to add sulfuric acid to hydrogen peroxide and not vice versa)
- Immerse sample in solution for 10 minutes
- Rinse in DI for at least 2 minutes

Solvent Clean

- Immerse sample in acetone for 2 minutes
- Immerse sample in isopropyl alcohol (IPA) for 2 minutes
- Dry using an N2 gun

B.4 Anisotropic Etching With TMAH

Thermal oxide was used as a mask in wet anisotropic etching of silicon. The selectivity ratio of silicon-to-silicon dioxide the TMAH is extremely large. The author has comfortably etched more than 1 millimeter deep into silicon in TMAH using an oxide mask only 8000 Å thick.

- Spin HMDS
- Spin 1827 @ 3.5 krpm (maximum ramp) for 30 seconds
- Soft Bake: 105°C hotplate for 1 minute 15 seconds

• Exposure: 11 seconds at 20 mW/cm^2

• Develop in DI:351 concentrate (5:1) for 45 seconds

• Rinse in DI for 2 minutes

• Hard Bake: 130°C hotplate for 2 minutes

• Spin 1827 on backside @ 3.5 krpm (maximum ramp) for 30 seconds

• Soft Bake: 105°C hotplate for 2 minutes propped on glass slides so pattern on front side is not damaged

• Hard Bake: 130°C hotplate for 2 minutes propped on glass slides

• Etch oxide in BHF (etch rate ~ 900 Å/minute)

• Rinse in DI for 2 minutes

• Remove resist in Acetone – 1 minute

• IPA rinse for 1 minute

• BHF dip for 10 seconds

• Rinse in DI for 2 minutes and transport sample immersed in DI

• Remove sample from DI and immediately place in TMAH

• Etch conditions: 25 wt.% TMAH @ 80°C

• When etching finished, rinse thoroughly in DI

B.5 Probe Fabrication with Frontside Metalization

Starting Material: ¼ of a 4" diameter bare silicon wafer

- Thickness = 100 μm
- Resistivity > 2000 Ωcm
- Double side polished

1) Wafer Mounting #1

A) Spin 1827 on 3"x 2" glass slide @ 3.5 krpm for 30 seconds

B) Place wafer on slide

C) Bake resist on 80°C hotplate for 2 minutes, then on 130°C hotplate for 2 minutes

2) Metalization

A) Spin HMDS @ 2.5 krpm for 30 seconds

B) Spin 5214 @ 2.5 krpm for 30 seconds

C) Bake resist on 105°C hotplate for 1 minute 15 seconds

D) Expose at 20 mW/cm^2 for 4.5 seconds

E) Reversal bake on 130°C hotplate for 1 minute

F) Flood exposure at 20 mW/cm^2 for 90 seconds

G) Develop in AZ327 for 50 seconds

H) Metal Evaporation: Cr/Au/Ti (500 Å / 9000 Å / 500 Å)

I) Liftoff and wafer detachment from slide: soak in acetone overnight, apply heat if necessary

NOTE *On mask pattern, leave a 4 μm gap between any metalization and area to be etched to protect Au from being etched.*

3) Wafer Mounting #2

A) Spin 1827 on ¼ wafer piece, 400 μm thick @ 3.5 krpm for 30 seconds

B) Place 100 μm wafer, metal side up, on 400 μm wafer

D) Bake resist on 80°C hotplate for 2 minutes then on 130°C hotplate for 2 minutes

4) Patterning of Deep Etch Mask

A) Spin HMDS @ 4.0 krpm for 30 seconds

B) Spin 4620 @ 4.0 krpm for 30 seconds

C) Bake resist on 105°C hotplate for 2.5 minutes

D) Align and expose at 20 mW/cm^2 for 30 seconds

E) Develop in 351:DI (1:5) for 2 minutes

5) Wafer Mounting #3

A) Spin HMDS on full 4" diameter wafer (400 μm thick with thermal oxide) @ 4.0 krpm for 30 seconds

B) Spin 4620 @ 4.0 krpm for 30 seconds

C) Place 100 μm / 400 μm ¼ wafer assembly on full 4" wafer

D) Bake resist at 110°C in oven for 40 minutes

6) Deep Etch and Probe Release

Use thru wafer recipe found in Appendix A.2. Etch rate depends rather strongly on pattern to be etched. Etch rates from ~ 2.6 to 6 μm/minute have been measured. Release in Acetone. Etch Ti layer to expose Au for probing.

B.6 Waveguide Fabrication

Starting Material: ¼ of a 4" diameter Silicon wafer

- Thickness = 2000 μm
- Resistivity > 2000 Ωcm
- Double side polished
- Thermal oxide ~ 8000 Å

1) Etching of Waveguides

A) Spin HMDS

B) Spin 1827 @ 3.5 krpm (maximum ramp) for 30 seconds

C) Soft Bake on 105°C hotplate for 2 minutes

D) Exposure: 11 seconds at 20 mW/cm^2

E) Develop in DI:351 concentrate (5:1) for 45 seconds

F) Rinse in DI for 2 minutes

G) Hard Bake: 130°C hotplate for 2 minutes

H) Spin 1827 on backside @ 3.5 krpm (maximum ramp) for 30 seconds

I) Soft Bake: 105°C hotplate for 2 minutes propped on glass slides so pattern on front side is not damaged

J) Hard Bake: 130°C hotplate for 2 minutes propped on glass slides

K) Etch oxide in buffered hydrofluoric acid (BHF): etch rate ~ 900 Å/minute

L) Rinse in DI for 2 minutes

M) Remove resist in Acetone – 1 minute

N) IPA rinse for 1 minute, N_2 dry

O) BHF dip for 10 seconds

P) Rinse in DI for 2 minutes and keep sample immersed in DI

Q) Remove sample from DI and immediately place in TMAH

R) Etch conditions: 25 wt.% TMAH @ 80°C

S) When etching finished, rinse thoroughly in DI

2) Etching of Probe Cradle (or shield)

A) Spin HMDS 4 krpm for 30 seconds

B) Spin 4260 4 krpm for 30 seconds

C) Resist bake 105°C hotplate for 3 minutes

D) Exposure: 20 mW/cm^2 for 30 seconds

E) Development DI:351 (5:1) for 2 minutes

F) Wafer Mounting: Spin HMDS on full 4" diameter wafer (400 μm thick with thermal oxide on both sides) @ 4.0 krpm for 30 seconds

G) Spin 4620 @ 4.0 krpm for 30 seconds and place 2mm thick ¼ wafer piece on full 4" wafer

H) Resist bake at 110°C in oven for 40 minutes

I) Use thru wafer recipe found in A.2. Release in acetone.

3) Dicing of waveguides

A) Spindle speed: 5.0 krpm (Norton representative suggests 3.0 krpm)

B) Cutting speed: 40 mils/second

C) Maximum depth per pass: 3 mils (Norton representative suggests 10 mils)

D) Height = 2 mils

E) Thickness = 84 mils

4) Metalization of waveguides

A) Piranha clean etched wafers (See section B.3)

B) Sputter 500Å Ti and 1.1 μm of Au

5) Assembly of waveguide

A) Insert probes into cradles of bottom wafer

B) Insert glass spheres into alignment pits

C) Align top wafer manually

D) Bond using EV- bonder: 22 N/cm2 @ 350°C for 30 minutes

APPENDIX C

SCHEMATIC DIAGRAM OF OXIDATION BOAT

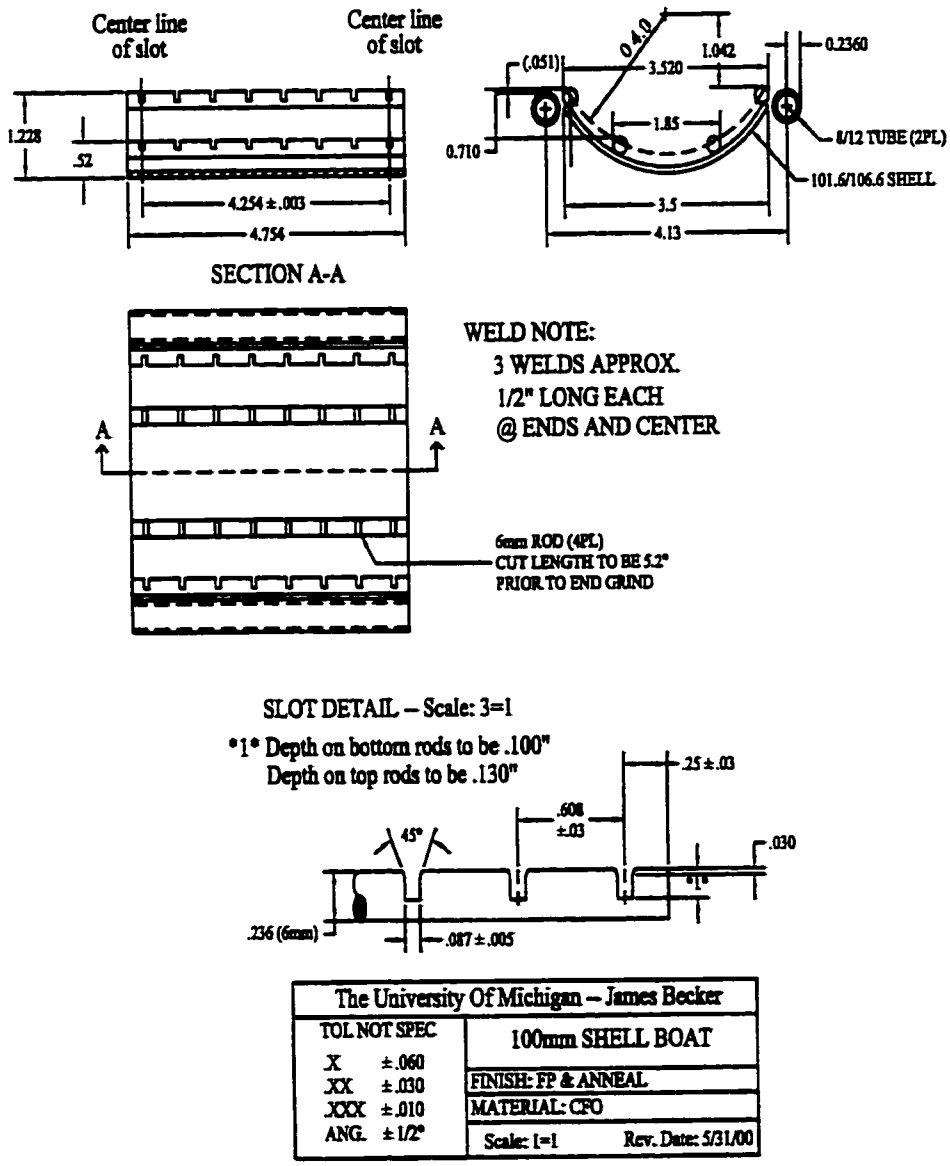

Figure C.1: Schematic diagram of oxidation boat designed to accommodate 2mm thick silicon.

APPENDIX D

OPERATION INSTRUCTIONS FOR ELECTRODEPOSITION SETUP

(1) Fill appropriate beaker with a 1:1 mixture of PEPR 2400 photoresist and deionized water. Introduce a stirring rod.

- Fill with 1:1 mixture to 1200 ml total for a 2000 ml beaker.
- Fill with 1:1 mixture to 1800 ml for the rectangular beaker.

(2) Set stirrer to 200 rpm.

(3) Cover with polypropylene cover and insert cathode(s) using the appropriate sized tube connectors. The yellow and black leads from the power supply are for the cathodes. If but one cathode is used (i.e. a single-sided deposition) connect yellow and black leads together.

(4) Set plate temperature to 52°C for the 2000 ml beaker or to 64°C for the rectangular beaker. Wait for approximately 2-3 hours for the mixture to come to the operating temperature of 30°C. Verify operating temperature with hotplate probe and readjust hotplate temperature if necessary. Be careful not to significantly overheat the mixture lest excessive solvent is driven off.

(5) From Windows operating system, select "HP VEE 3.0" and then "HPVEE."

(6) Select File → open → EPDFINAL(.VEE)

(7) Plug HP6035A power supply into designated outlet (outlet in room 1403 EECS).

(8) Turn on power supply.

(9) Press and hold "OVP" to verify that overprotection is set to 359 V. To adjust voltage overprotection level consult HP6035A instruction manual.

(10) Reset power supply as follows. (Note: Resetting the supply is necessary to ensure that the desired voltage is supplied by the HP6035A during actual runs.)

- Select "run" from the deposition program window.
- Input desired voltage and hit "OK"
- Input deposition time and hit "OK"
- Once deposition has started and a voltage is registering on the power supply hit "STOP" and then "RESET."

****Always verify that the power supply is registering zero volts before proceeding****

(11) Introduce sample by dipping once in the solution, pulling it out momentarily, and then reintroducing. Such a dipping procedure is intended to foster wetting.

(12) Press "LCL" on HP6035A ("Current" light should illuminate).

(13) Hold "Display Setting" on HP6035A and rotate knob to maximum desired current (maximum value is 5.12 A).

(14) Run deposition

- Select "run" from the deposition program window.
- Input desired voltage and hit "OK."
- Input deposition time and hit "OK."

- The power supply will provide the desired voltage for the proscribed time and then will bring the voltage back to zero.

- After deposition hit "AUTOSCALE" from the deposition window. The current profile will then be properly displayed. The current profile is saved under: c:\vee_user\myfile. Column one of the file is the deposition time in seconds and column two the current in amperes. The file will be replaced each time the program is run.

****Always verify that the power supply is registering zero volts before proceeding****

(15) Remove sample and rinse in a 500 ml beaker filled with deionized water.

(16) Rinse in second 500 ml beaker filled with deionized water and dry using the N_2 gun.

Return to "press LCL" step (step 12) for further depositions.

APPENDIX E

ON THE INTERCONNECTION OF RECTANGULAR AND DIAMOND WAVEGUIDES

E.1 Introduction

Various methods were considered as means to measure the attenuation in the diamond waveguide. Time gating was ruled out due to the lack of sufficient bandwidth to make such a measurement meaningful. A TRL-type protocol in which a thru, a short and delays would be fabricated in diamond waveguide was also considered, but shelved in favor of attempting a simple mismatched connection. In section E.2, an examination of extracting the propagation constant of a transmission line in such a cascaded connection is presented.

E.2 Extraction of Line Parameters

Cascaded Waveguide Connection

A photograph of the test setup is given in Figure E.1 along with a transmission line representation of the setup. The setup consists of a series connection of spans of waveguide, with a section of silicon diamond waveguide connected at both ends with sections of WR-10. Such a series of cascaded two-ports may be analyzed with the aid of

[ABCD] matricies as the overall [ABCD] for the system is a simple multiplication of the individual matricies. The resulting cascade equations become surprisingly complex and so two alternate means of developing the required equations for line parameter extraction are pursued.

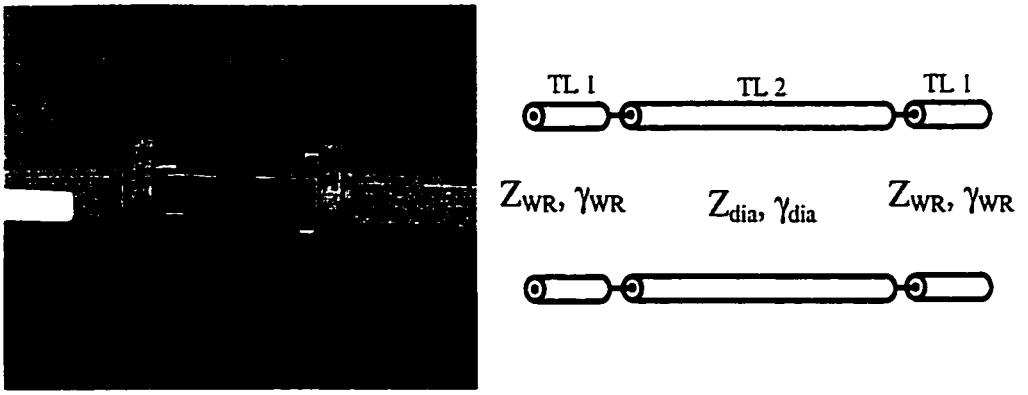

Figure E.1: Connection of silicon diamond waveguide to the test ports and a first-order transmission line representation of the setup.

Multiple Reflection Method

We may consider the cascaded transmission line problem as similar to many optical transmission/reflection problems. A schematic diagram given in Figure E.2 that will aid in an analysis along these lines.

We assume that a wave propagating in medium 1 is incident at the interface between medium 1 and medium 2. A portion of this signal (A) is immediately reflected if there is an impedance mismatch between the two media, and a portion transmitted into medium 2 (unless medium 2 is a totally reflecting surface). This signal (B) propagates in medium 2 suffering attenuation in accord with the attenuation constant of the medium. Once the signal reaches the second interface it is partially reflected back toward the first interface and partially transmitted into medium 3 (assumed to have the same properties as medium 1 thus mimicing our experimental setup). The process continues indefinitely with the

signal strength of the propagating wave ever dwindling. Expressions for the signal at locations A through K are given below.

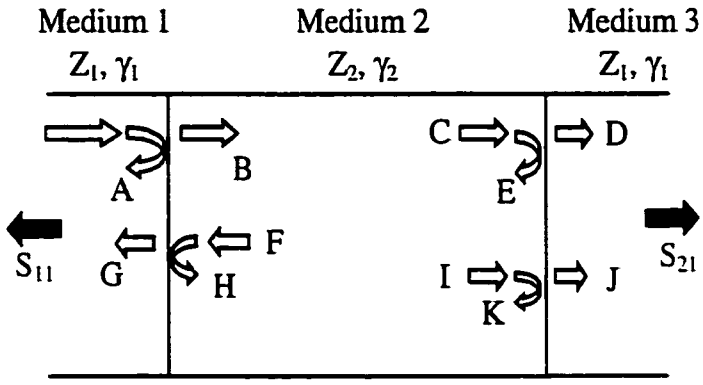

Figure E.2: Schematic representation of the mulitple reflections in a simple three medium connection.

$$A = \Gamma_1$$

$$B = 1 - \Gamma_1$$

$$C = (1 - \Gamma_1)e^{-\gamma_2 \ell_2}$$

$$D = (1 - \Gamma_1)(1 - \Gamma_2)e^{-\gamma_2 \ell_2}$$

$$E = (1 - \Gamma_1)\Gamma_2 e^{-\gamma_2 \ell_2}$$

$$F = (1 - \Gamma_1)\Gamma_2 e^{-2\gamma_2 \ell_2}$$

$$G = (1 - \Gamma_1)(1 - \Gamma_2)\Gamma_2 e^{-2\gamma_2 \ell_2}$$

$$H = (1 - \Gamma_1)\Gamma_2^2 e^{-2\gamma_2 \ell_2}$$

$$I = (1 - \Gamma_1)\Gamma_2^2 e^{-3\gamma_2 \ell_2}$$

$$J = (1 - \Gamma_1)(1 - \Gamma_2)\Gamma_2^2 e^{-3\gamma_2 \ell_2}$$

$$K = (1 - \Gamma_1)\Gamma_2^3 e^{-3\gamma_2 \ell_2}$$

Recalling that medium 1 and medium 3 are composed of the same material, the two reflection coefficients are given by

$$\Gamma_1 = \frac{Z_2 - Z_1}{Z_2 + Z_1}$$

$$\Gamma_2 = \frac{Z_1 - Z_2}{Z_1 + Z_2}$$

It should also be mentioned that reflection coefficient 1 corresponds to the case of a wave incident on the medium 1 / medium 2 interface looking from medium 1, and reflection coefficient 2 corresponds to the case of a wave incident on the interface looking from medium 2. In light of these definitions we may understand that Γ_1 will only occur once in our equations corresponding to the initial reflection. The overall reflection coefficient looking from medium 1 is the sum of an infinite number of terms, a few of which are given below.

$$S_{11} = \Gamma_1 + (1-\Gamma_1)(1-\Gamma_2)\Gamma_2 e^{-2\gamma_2 \ell_2} + (1-\Gamma_1)(1-\Gamma_2)\Gamma_2^3 e^{-4\gamma_2 \ell_2} + \bullet\bullet\bullet$$

We can rewrite this in terms of the following infinite sum:

$$S_{11} = \Gamma_1 + (1-\Gamma_1)(1-\Gamma_2)\sum_{n=0}^{\infty} \Gamma_2^{2n+1} e^{-2(n+1)\gamma_2 \ell_2}$$

or,

$$S_{11} = \Gamma_1 + (1-\Gamma_1)(1-\Gamma_2)\Gamma_2 e^{-2\gamma_2 \ell_2} \sum_{n=0}^{\infty} \Gamma_2^{2n} e^{-2n\gamma_2 \ell_2}$$

We may use the following identity to remove the summation from the above equation:

$$\sum_{n=0}^{\infty} s^n = \frac{1}{1-s}$$

Doing so, we are left with the following expression for the overall reflection coefficient of the system:

$$S_{11} = \Gamma_1 + (1-\Gamma_1)(1-\Gamma_2)\Gamma_2 \frac{e^{-2\gamma_2\ell_2}}{1-\Gamma_2^2 e^{-2\gamma_2\ell_2}}.$$

Algebraic manipulation leads us to the more compact form given below, namely,

$$S_{11} = \frac{\Gamma_1 + \Gamma_2 e^{-2\gamma_2\ell_2}}{1-\Gamma_2^2 e^{-2\gamma_2\ell_2}}.$$

An expression for S_{21} may be derived in a similar manner as follows:

$$S_{21} = (1-\Gamma_1)(1-\Gamma_2)e^{-\gamma_2\ell_2} + (1-\Gamma_1)(1-\Gamma_2)\Gamma_2^2 e^{-3\gamma_2\ell_2} + (1-\Gamma_1)(1-\Gamma_2)\Gamma_2^4 e^{-5\gamma_2\ell_2} + \bullet\bullet\bullet.$$

$$S_{21} = (1-\Gamma_1)(1-\Gamma_2)\sum_{n=0}^{\infty}\Gamma_2^{2n} e^{-(2n+1)\gamma_2\ell_2}.$$

$$S_{21} = (1-\Gamma_1)(1-\Gamma_2)e^{-\gamma_2\ell_2}\sum_{n=0}^{\infty}\Gamma_2^{2n} e^{-2n\gamma_2\ell_2}.$$

and finally,

$$S_{21} = (1-\Gamma_1)(1-\Gamma_2)\frac{e^{-\gamma_2\ell_2}}{1-\Gamma_2^2 e^{-2\gamma_2\ell_2}} = (1+\Gamma_1\Gamma_2)\frac{e^{-\gamma_2\ell_2}}{1-\Gamma_2^2 e^{-2\gamma_2\ell_2}}$$

Since $\Gamma_1=-\Gamma_2$, we have.

$$S_{11} = \frac{\Gamma_1 + \Gamma_2 e^{-2\gamma_2\ell_2}}{1-\Gamma_2^2 e^{-2\gamma_2\ell_2}} = \frac{\Gamma_2\left(e^{-2\gamma_2\ell_2}-1\right)}{1-\Gamma_2^2 e^{-2\gamma_2\ell_2}}$$

and

$$S_{21} = (1+\Gamma_1\Gamma_2)\frac{e^{-\gamma_2\ell_2}}{1-\Gamma_2^2 e^{-2\gamma_2\ell_2}} = \left(1-\Gamma_2^2\right)\frac{e^{-\gamma_2\ell_2}}{1-\Gamma_2^2 e^{-2\gamma_2\ell_2}}.$$

Letting $\Gamma_2 = A+jB$, we find:

$$S_{11} = \frac{(A+jB)\left(e^{-2(\alpha_2+j\beta_2)\ell_2} - 1\right)}{1-(A+jB)^2 e^{-2(\alpha_2+j\beta_2)\ell_2}} \qquad [E.1]$$

and

$$S_{21} = \left(1-(A+jB)^2\right)\frac{e^{-(\alpha_2+j\beta_2)\ell_2}}{1-(A+jB)^2 e^{-2(\alpha_2+j\beta_2)\ell_2}} \qquad [E.2]$$

Under the case in which medium 2 is lossless the above expressions become:

$$S_{11} = \frac{A\left(e^{-2j\beta_2\ell_2} - 1\right)}{1-A^2 e^{-2j\beta_2\ell_2}}$$

and

$$S_{21} = \left(1-A^2\right)\frac{e^{-j\beta_2\ell_2}}{1-A^2 e^{-2j\beta_2\ell_2}}$$

Total Wave Impedance Method

As an alternate means of deriving the structure's reflection coefficient, we may use the concept of total wave impedance. In such a method the total wave impedance, which is simply the ratio of the total wave voltage to total wave current (i.e. we include both forward and backward waves), is used as a boundary condition when moving from one medium (or transmission line) to the next. Figure E.3 below will aid in the analysis.

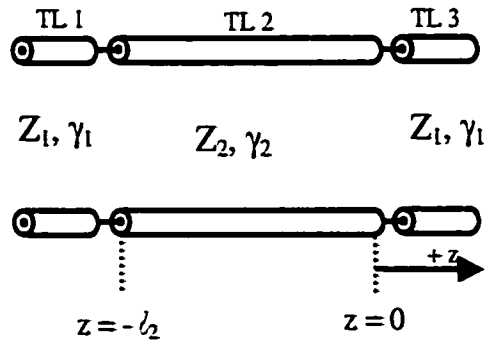

Figure E.3: Schematic of transmission line cascade.

As a first step we determine the total wave impedance at z = 0+. We assume that transmission line 3 (TL 3) is infinitely long and thus there will be no backward travelling wave on this line. This is exactly what is to be expected upon calibration of our experimental setup. Thus on TL 3 the total wave impedance is simply the characteristic impedance of the line. We may invoke continuity of the total wave impedance across the z = 0 boundary. That is,

$$Z_{TOTAL}(z=0^-) = Z_{TOTAL}(z=0^+) = Z_1 .$$

Since we are interested in the reflection on TL 1, we now must travel along TL 2 from z = 0 to z = $-\ell_2$. In doing so, we utilize the wave impedance to generate the reflection coefficient, which is readily transferred along a line. The reflection coefficient at z = 0^- is given by

$$\Gamma(z=0^-) = \frac{Z_{TOTAL}(z=0^-) - Z_2}{Z_{TOTAL}(z=0^-) + Z_2} = \frac{Z_1 - Z_2}{Z_1 + Z_2} .$$

At z = $-\ell_2^+$, the reflection coefficient transfers to

$$\Gamma(z=-\ell_2^+) = \Gamma(z=0^-)e^{-2\gamma_2\ell_2} = \frac{Z_1 - Z_2}{Z_1 + Z_2}e^{-2\gamma_2\ell_2} .$$

We wish to now cross the boundary from TL 2 to TL 1, but to do so we need to convert back to the total wave impedance, which is given by the following equation.

$$Z_{TOTAL}\left(z=-\ell_2^+\right) = Z_2\frac{1+\Gamma(z=-\ell_2{}^+)}{1-\Gamma(z=-\ell_2{}^+)} .$$

Transferring this impedance across the boundary we now have the result that

$$Z_{TOTAL}\left(z=-\ell_2^-\right) = Z_{TOTAL}\left(z=-\ell_2^+\right) = Z_2\frac{1+\Gamma(z=-\ell_2{}^+)}{1-\Gamma(z=-\ell_2{}^+)} .$$

The total reflection coefficient as seen from TL 1 looking in the z-direction is thus

$$S_{11} = \Gamma(z = -\ell_2^-) = \frac{Z_{TOTAL}(z = -\ell_2^-) - Z_1}{Z_{TOTAL}(z = -\ell_2^-) + Z_1}.$$

Substituting for $Z_{TOTAL}(z = -\ell_2^-)$, we find that

$$S_{11} = \Gamma(z = -\ell_2^-) = \frac{Z_2 \dfrac{1 + \Gamma(z = -\ell_2^+)}{1 - \Gamma(z = -\ell_2^+)} - Z_1}{Z_2 \dfrac{1 + \Gamma(z = -\ell_2^+)}{1 - \Gamma(z = -\ell_2^+)} + Z_1},$$

or

$$S_{11} = \Gamma(z = -\ell_2^-) = \frac{Z_2\left(1 + \Gamma(z = -\ell_2^+)\right) - Z_1\left(1 - \Gamma(z = -\ell_2^+)\right)}{Z_2\left(1 + \Gamma(z = -\ell_2^+)\right) + Z_1\left(1 - \Gamma(z = -\ell_2^+)\right)}.$$

In light of the previous section we may write the following:

$$\Gamma(z = -\ell_2^+) = \Gamma(z = 0^-)e^{-2\gamma_2\ell_2} = \frac{Z_1 - Z_2}{Z_1 + Z_2}e^{-2\gamma_2\ell_2} = \Gamma_2 e^{-2\gamma_2\ell_2}.$$

This allows us to write S_{11} as

$$S_{11} = \Gamma(z = -\ell_2^-) = \frac{Z_2\left(1 + \Gamma_2 e^{-2\gamma_2\ell_2}\right) - Z_1\left(1 - \Gamma_2 e^{-2\gamma_2\ell_2}\right)}{Z_2\left(1 + \Gamma_2 e^{-2\gamma_2\ell_2}\right) + Z_1\left(1 - \Gamma_2 e^{-2\gamma_2\ell_2}\right)},$$

or

$$S_{11} = \Gamma(z = -\ell_2^-) = \frac{(Z_2 - Z_1) + \Gamma_2 e^{-2\gamma_2\ell_2}(Z_1 + Z_2)}{(Z_1 + Z_2) - \Gamma_2 e^{-2\gamma_2\ell_2}(Z_1 - Z_2)}$$

Dividing numerator and denominator by (Z_1+Z_2) we continue and find that

$$S_{11} = \Gamma(z = -\ell_2^-) = \frac{\Gamma_1 + \Gamma_2 e^{-2\gamma_2\ell_2}}{1 - \Gamma_2^2 e^{-2\gamma_2\ell_2}}.$$

The above equation is identical to that derived in the previous section.

In measuring the performance of the silicon diamond waveguide, we will of course know the length of the section of guide (ℓ_{SD}). In addition, the impedance of the section of rectangular waveguide (Z_{oWR}) is available in the standard formulas for such structures. This leaves us with two unknowns which are potentially complex numbers, γ_{SD} and Z_{oSD}. We are interested in frequencies at which Z_{oSD} is purely real, that is, we will only consider frequencies above the silicon diamond waveguide's fundamental cutoff frequency. (At these frequencies, the WR-10 sections are also above cutoff.) Equations found in chapter 6 are available for obtaining the impedance of the waveguides under this condition. This leaves us with but one complex variable, γ_{SD}, which can be expressed as

$$\gamma_{SD}(f) = \alpha_{SD}(f) + j\beta_{SD}(f)$$

Thus by measuring the complex return and insertion loss, the propagation constant of the diamond waveguide may be obtained from the four equations that result by breaking equations E.1 and E.2 into real and imaginary components. This was the tact to be taken. In the process of analyzing the first set of measured data it became clear that the simple transmission line model was not sufficient and that reactive elements at the waveguide junctions would need to be considered.

As mentioned in Chapter 6, the flange connection between the diamond waveguide and the feed WR-10 sections was far from perfect due to the lack of sufficient tightening. In such a case, determining the parasitic junction elements (both those inherent at the junction and those due to imperfect connection) would be difficult, the values of which may different in each measurement case. For this reason, the attenuation in the diamond waveguide was determined solely through the insertion loss and thus overestimates the

loss to some degree. (Again, the attenuation values were determined at local minima in the return loss to lessen the effect of neglecting the return loss in the attenuation calculation.) To conclude this look at the diamond waveguide measurement, an example of the inherent reactive elements at a rectangular waveguide/diamond waveguide junction is considered. Specifically, a model of the equivalent circuit of a diamond iris in a rectangular waveguide is given.

Diamond Iris in a Rectangular Waveguide

A sketch of the junction between a rectangular waveguide and diamond waveguide is illustrated in Figure E.4. The actual silicon diamond waveguide sections were formed in a split block manner (cut along waveguide's E-plane) using two 2mm thick wafers. The diamond waveguide blocks were diced to be 6 mm wide. Though not shown in the sketch of Figure E.4, the diamond waveguide and WR-10 were aligned with flange as described in Chapter 6. To investigate the properties of the waveguide junction, a full-wave simulation of an infinitesimally thin diamond iris in a WR-10 was simulated using HFSS and modeled using LIBRA. A sketch of the simulated structure is given in Figure E.5. (A model of the actual junction would include a finite length of diamond waveguide; the iris is a convenient tool for illustration of the existence of reactive elements.)

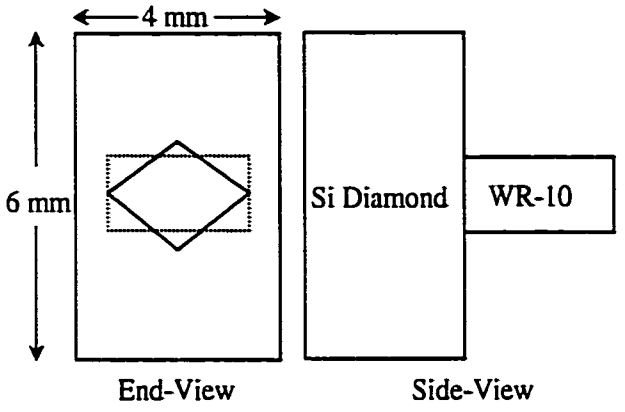

Figure E.4: End and side views of the connection of a section of silicon diamond waveguide and WR-10.

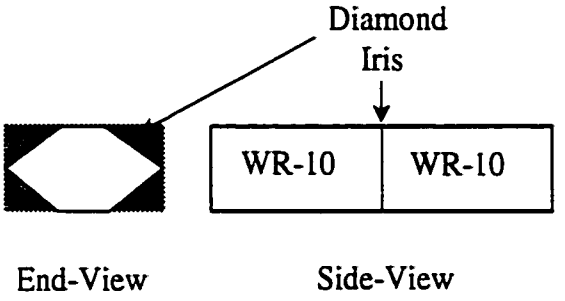

Figure E.5: Schematic diagram of a "diamond iris" in a rectangular waveguide.

Since the iris may be considered to consist of both inductive and capacitive diaphragms, a simple parallel LC was used to model the obstruction. A LIBRA circuit schematic of the equivalent circuit model is given in Figure E.6.

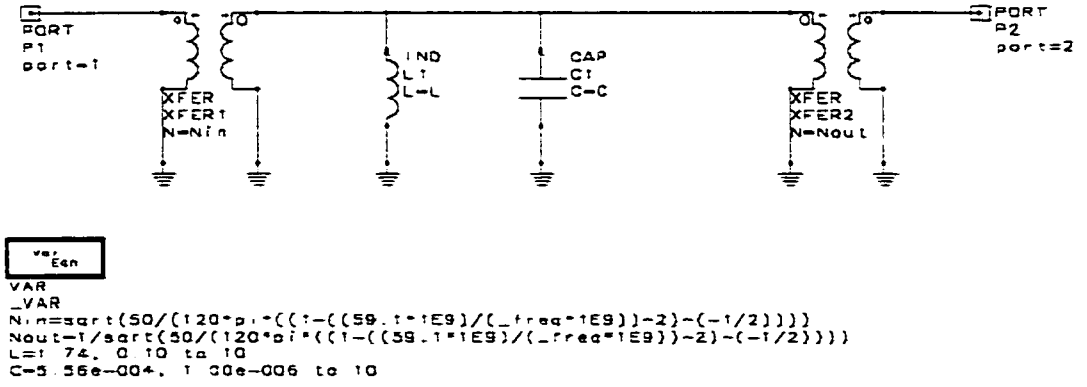

Figure E.6: LIBRA schematic of the equivalent circuit for the waveguide and iris of Figure E.5.

To isolate the behavior of the iris, the simulation results of HFSS were de-embedded from each WR-10 excitation port to the precise location of the iris. To model the structure in LIBRA, the 50Ω ports (P1 and P2 in Figure E.6) were stepped up to the wave impedance of the WR-10 through the input and output transformers (XFER1 and XFER2) by adjusting the turns ratio. The L and C values were then optimized to fit the magnitude and phase of S11 at the extremities of the frequency range (75 and 110 GHz) as per the LIBRA test bench shown in Figure E.7. A LIBRA optimization routine returned values of 1.74 nH and 5.56 x10^{-16} F for the inductor and capacitor respectively.

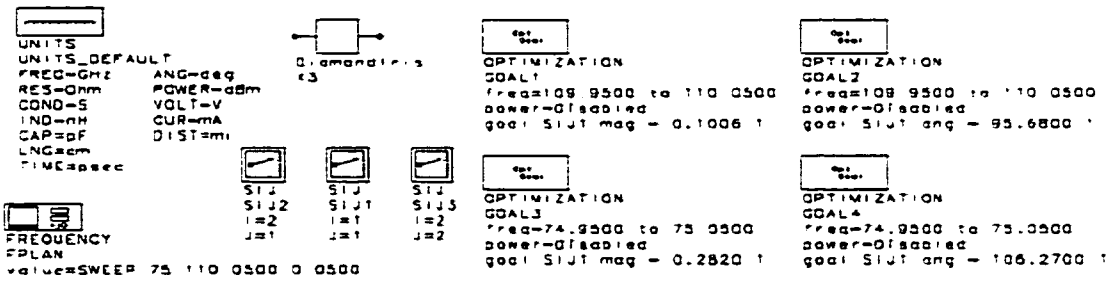

Figure E.7: LIBRA Test Bench for simulation of diamond iris obstruction.

Expressions for a variety of obstructions in rectangular waveguide have been provided by Marcuvitz [91]. Consider Figure E.8 in which an effort is made to cast the diamond iris into equivalent inductive diaphragm that is described in [93]. One means to arrive at an equivalent value for d' is to equate obstruction area. In the case of the inductive diaphragm we have the following.:

$$\text{Diamond Iris Area} = 4\left(\frac{1}{2}x_d y_d\right) = 2x_d y_d \ ,$$

$$\text{Inductive Diaphragm Area} = 2bd',$$

and

$$d' = \frac{x_d y_d}{b}.$$

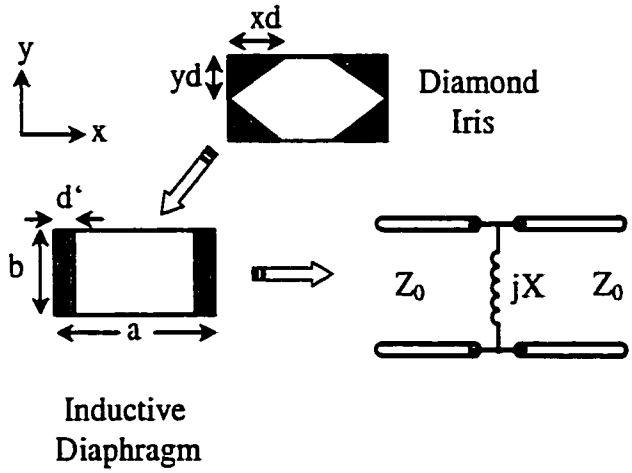

Figure E.8: The diamond iris as an equivalent shunt inductance.

For the case of the diamond iris the effective d' = 449 μm. Equation 1c on page 221 of [93] gives:

$$\frac{jX}{Z_o} \approx \frac{a}{\lambda_g}\cot^2\left(\frac{\pi d'}{a}\right)\left[1+\frac{2}{3}\left(\frac{\pi d'}{\lambda}\right)^2\right].$$

Evaluating this expression yields L = X/ω = 1.77 nH, suggesting that the optimized inductance value is quite reasonable. Now consider Figure E.9 in which the diamond iris is cast into an equivalent capacitive diaphragm. In a similar manner:

$$\text{Diamond Iris Area} = 4\left(\frac{1}{2}x_d y_d\right) = 2x_d y_d,$$

$$\text{Capacitive Diaphragm Area} = 2af',$$

and

$$f' = \frac{x_d y_d}{a} .$$

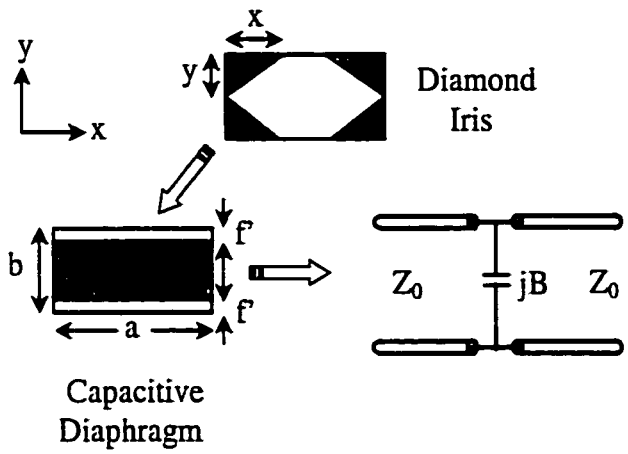

Figure E.9: The diamond iris as an equivalent shunt capacitance.

For the case of the diamond iris, the effective f' = 224.5 μm. Equation 2a on page 218 of [93] gives:

$$\frac{B}{Y_o} = \frac{4b}{\lambda_g}\left[\ln\left(\csc\frac{\pi d}{2b}\right) + \frac{Q_2\cos^2\frac{\pi d}{2b}}{1+Q_2\sin^4\frac{\pi d}{2b}} + \frac{1}{16}\left(\frac{b}{\lambda_g}\right)^2\left(1-3\sin^2\frac{\pi d}{2b}\right)^2\cos^4\frac{\pi d}{2b}\right]$$

where

$$Q_2 = \frac{1}{\sqrt{1-\left(\frac{2b}{n\lambda_g}\right)^2}} - 1 .$$

Evaluating this expression gives C = B/ω = 8.664x10^{-16} F. This value for the shunt capacitance is quite close to the optimized value from LIBRA. One reason that the analytical value is a bit larger than the LIBRA value may rest in the fact that the diamond

iris (for $a_{WR\text{-}10} = a_{silicon\ diamond}$) does not provide shunt capacitance at x = a/2 – the region of maximum electric field. The inductive character of the diamond iris is seemingly unaffected by the iris' shape perhaps due to the fact that magnitude of the magnetic field of the dominant mode does not vary along the y dimension.

A comparison between the HFSS simulation of the diamond iris and the equivalent circuit model of the iris is given in Figure E.10. Excellent agreement between the HFSS simulation results and the LIBRA model exist in both magnitude and phase of the return loss.

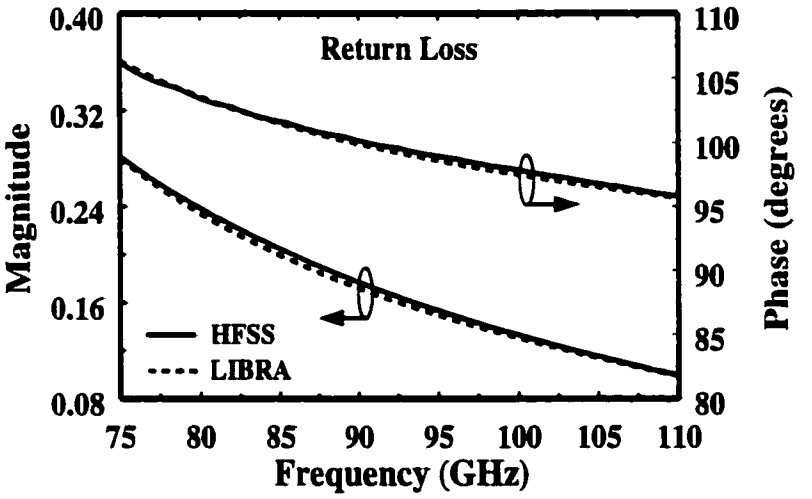

Figure E.10: Simulated magnitude and phase of the return loss of a diamond iris – both HFSS and LIBRA model results shown.

BIBLIOGRAPHY

BIBLIOGRAPHY

Chapter 1

[1] Fawwaz T. Ulaby, "Scanning the Issue, Terahertz Technology," Proceedings of The IEEE, Vol. 80, No. 11, November 1992, pp.1659-1661.

[2] Thomas G. Phillips and Jocelyn Keene, "Submillimeter Astronomy," Proceedings of The IEEE, Vol. 80, No. 11, November 1992, pp.1662-1679.

[3] David M. Pozar, *Microwave Engineering*, Addison-Wesley, Figure 11.52, 1990.

[4] David M. Pozar, *Microwave Engineering*, Addison-Wesley, p.651, 1990.

[5] Youngwoo Kwon, Dimitris Pavlidis, Timothy L. Brock and Dwight C. Streit, "A D-Band Monolithic Fundamental Oscillator Using InP-Based HEMT's," IEEE Transactions on Microwave Theory and Techniques, Vol. 41, No. 12, December 1993, pp. 2336-2344.

[6] H. Eisele, "Two-terminal devices as fundamental solid-state terahertz oscillators," in Terahertz Spectroscopy and Applications II, SPIE Proceedings Vol. 3828, 1999, pp.70-80.

[7] James P. Becker, Yongshik Lee, Jack R. East and Linda P.B. Katehi, "Silicon Micromachined Power Combining Module," DARPA THz Solid State Sources review.

[8] Rashaunda Monique Henderson, *Silicon-Based Micromachined Packaging Techniques For High-Frequency Applications*, Ph.D. thesis, University of Michigan, Ann Arbor, MI. 1999.

[9] Katherine Juliet Herrick, *W-Band Three-Dimensional Integrated Circuits Utilizing Silicon Micromachining*, Ph.D. thesis, University of Michigan, Ann Arbor, MI. 2000.

Chapter 2

[10] B. Senitzky and A.A. Olinier, "Introduction: Submillimeter Waves – A Transition Region," in Proceedings of the Symposium On Submillimeter Waves, Jerome Fox, editor, Polytechnic Press, 1971.

[11] William R. McGrath, Christopher Walker, Markus Yap and Yu-Chong Tai, "Silicon Micromachined Waveguides for Millimeter-Wave and Submillimeter-Wave Frequencies," IEEE Microwave and Guided Wave Letters, Vol. 3, No. 3, March 1993, pp. 61-63. NOTE value of 0.12 dB/cm is estimated from Figure 2b of the above reference whereas the value of 0.024 dB/λg is given in the body of the reference.

[12] The values of the attenuation in dB per cm were taken from table 2.1 of reference [8] and represent the best reported values. The attenuation expressed in dB/λg were calculated from the data in the table using the quoted values of the effective dielectric constant.

[13] Thomas M. Weller, Linda P.B. Katehi, and Gabriel M. Rebeiz, "High Performance Microshield Line Components," IEEE Transactions on Microwave Theory and Techniques, Vol. 43, No. 3, March 1995, pp. 534-543.

[14] The value of 0.25 dB/λg was determined using Figures 5 and 6 found in reference 13.

[15] Heng-Ju Cheng, John F. Whitaker, Thomas M. Weller and Linda P.B. Katehi, "Terahertz-Bandwidth Characteristics of Coplanar Transmission Lines on Low Permittivity Substrates," IEEE Transactions on Microwave Theory and Techniques, Vol. 42, No. 12, December 1994, pp. 2399-2406.

[16] Djafar K. Mynbaev and Lowell L. Scheiner, *Fiber-Optic Communications Technology*, Prentice-Hall, Upper Saddle River, NJ, Table 5.1 p. 165 (2001).

[17] Shiban K. Koul, *Millimeter Wave Optical Dielectric Integrated Guides and Circuits*, John Wiley and Sons, Inc., New York, p.3 (1997).

[18] Linda P.B. Katehi, "Novel Transmission Lines for the Submillimeter-Wave Region," Proceedings of the IEEE, Vol. 80, No. 11 November 1992, pp.1771-1787.

[19] Y. Tateno, H. Takahashi, T. Igarashi, and J. Fukaya, "A 150 W E-mode GaAs Power FET with 35% PAE for W-CDMA Base Station," Proceedings MTT Symposium, 1999, pp. 1087-1090.

[20] Kenneth J. Russel, "Microwave Power Combining Techniques," IEEE Transactions on Microwave Theory and Techniques, Vol. 27, No. 5, May 1979, pp. 472-478.

[21] S.P. Marsh, "Power Splitting and Combining Techniques On MMICS," The GEC Journal of Technology, Vol. 15, No.1, 1998, pp. 2-9.

[22] Kai Chang and Cheng Sun, "Millimeter-Wave Power-Combining Techniques," IEEE Transactions on Microwave Theory and Techniques, Vol. 31, No. 2, February 1983, pp. 91-107.

[23] James C. Wiltse and James W. Mink, "Quasi-Optical Power Combining of Solid-State Sources," Microwave Journal, February 1992, pp. 144-156.

[24] Paul D. Coleman, "Reminiscences on Selected Millenium Highlights in the Quest for Tunable Terahertz-Submillimeter Wave Oscillators," IEEE Journal of Selected Topics In Quantum Electronics," Vol. 6, No. 6, Nov/Dec 2000, pp.1000-1007.

[25] Gordon Chin, "Optically Pumped Submillimeter Laser Heterodyne Receivers: Astrophysical Observations and Recent Technical Developments," Proceedings of the IEEE, Vol. 80, No. 11, Nov. 1992, pp.1788-1799.

[26] Raymond Blundell and Cheuk-Yu Edward Tong, "Submillimeter Receivers for Radio Astronomy," Proceedings of the IEEE, Vol. 80, No. 11, Nov. 1992, pp.1702-1720.

[27] Gabriel M. Rebeiz, "Millimeter-Wave and Terahertz Integrated Circuit Antennas," Proceedings of the IEEE, Vol. 80, No. 11, Nov. 1992, pp.1748-1770.

[28] Thomas W. Crowe et al., "GaAs Devices and Circuits for Terahertz Applications," Infrared Physics and Technology 40 (1999), pp. 175-189.

[29] "Electro-Forming and Fabrication of Precision Waveguide Components," Catalog No. 8 from Custom Microwave.

[30] John A. Wright et al. "Integrated Silicon Micromachined Waveguide Circuits for Submillimeter Wave Applications," 6th International Symposium on Space Terahertz Technology, (1995) 387-396.

[31] C. E. Collins et al., "Technique for Micro-Machining Millimetrewave Rectangular Waveguide," Electronics Letters, Vol 34, No. 10, May 1998.

[32] C.E. Collins et al., "A New Micro-Machined Millimeter-Wave and Terahertz Snap-Together Rectangular Waveguide Technology," IEEE Microwave and Guided Wave Letters, Vol. 9, No. 2 February 1999, pp. 63-65.

[33] S.W. Moon et al., "Terahertz Waveguide Components Fabricated Using a 3D X-Ray Microfabrication Technique," Vol. 32, No. 19, Electronics Letters, Sept. 1996.

[34] I.C.E. Turcu et al., "X-ray Micro- and Nanofabrication Using a Laser-Plasma Source at 1nm Wavelength," Journal of Vacuum Science and Technology B, Vol. 15, N0. 6 November/December 1997, pp. 2495-2502.

[35] S. Lucyszyn, Q.H. Wang and I.D. Robertson, "0.1 THz Rectangular Waveguide on GaAs Semi-insulating Substrate," Electronics Letters, Vol 31, No. 9, April 1995.

Chapter 3

[36] Ted J. Hubbard and Erik K. Antonsson, "Emergent Faces in Crystal Etching," Journal of Microelectromechanical Systems, Vol. 3, No. 1, March 1994, pp. 19-27.

[37] Nim H. Tea et al., "Hybrid Postprocessing Etching for CMOS-Compatible MEMS," Journal of Micoelectromechanical Systems, Vol. 6, No. 4, December 1997, pp. 363-372.

[38] Stephan Linder, Chip Stacks For Memory Applications, PhD Dissertation, Physical Electronics Laboratory, ETH Zurich (Diss. ETH 11347), 1996.

[39] Les M. Landsberger, Sasan Naseh, Mojtaba Kahrizi and Makarand Paranjape, "On Hillocks Generated During Anisotropic Etching of Si in TMAH," Journal of Micoelectromechanical Systems, Vol. 5, No. 2, June 1996, pp. 106-116.

[40] Osamu Tabata, "pH-controlled etchants for silicon micromachining," Sensors and Actuators A 53, 1996, pp.335-339.

[41] Osamu Tabata et al., "Anisotropic etching of silicon in TMAH solutions," Sensors and Actuators A 34, 1992, pp. 51-57.

[42] A. Merlos, M. Acero, M.H. Bao, J. Bausells and J. Esteve, "TMAH/IPA anisotropic etching characteristics," Sensors and Actuators A 37-38, 1993, pp. 737-743.

[43] U. Schnakenberg, W. Benecke and P. Lange, "TMAHW Etchants for Silicon Micromachining," IEEE publication #91CH2817-5/91/0000-0815, 1991, pp. 815-818

[44] Xian-Ping Wu and Wen H. Ko, "Compensating Corner Undercutting In Anisotropic Etching of (100) Silicon," Sensors and Actuators, Vol. 18, 1989, pp. 207-215.

[45] B. Puers and W. Sansen, "Compensation Structures for Convex Corner Micromachining in Silicon," Sensors and Actuators, A21-A23, 1990. pp. 1036-1041.

[46] H.L. Offereins, K. Kühl and H. Sandmaier, "Methods for the Fabrication of Convex Corners in Anisotropic Etching of (100) Silicon in Aqueous KOH," Sensors and Actuators A, 25-27, 1991, pp. 9-13.

[47] Qingxin Zhang, Litian Liu and Zhijian Li, "A new approach to convx corner compensation for anisotropic etching of (100) Si in KOH," Sensors and Actuators A 56, 1996, pp. 251-254.

[48] R.A. Buser and N.F. de Rooij, "Monolithisches Kraftsensorfeld," VDI Berichte Nr. 667, Sensoren, Technologien und Anwendung, 1988, pp. 115-118.

[49] Arturo A. Ayón, "Time Multiplexed Deep Etching," Sensors, August 2000.

[50] Rough Surfaces, 2nd edition, Tom R. Thomas, Imperial College Press, London, 1999, p. 11.

[51] DEKTAK3 Surface Profile Measurement System, Installation, Operation and Maintenance Manual Revision 1.05, Sloan Technology – Veeco Instruments ("DEKTAK" is a registered trademark of Veeco Instruments Inc.)

[52] Calculus and Analytical Geometry, 2nd edition, C.H. Edwards and David E. Penney, Prentice-Hall, Inc., Englewood Cliffs, New Jersey, pp 679.

[53] Ansoft High Frequency Structure Simulator version 7.0.04, Ansoft Corporation, Four Station Square Suite 200, Pittsburgh, PA 15219-1119.

[54] IE3D Version 8.0, Zeland Software, Inc.

[55] Ansoft MAXWELL 2D, Ansoft Corporation, Four Station Square Suite 200, Pittsburgh, PA 15219-1119.

[56] LIBRA Series IV, HP Eesof.

[57] Roger B. Marks, "A Multiline Method of Network Analyzer Calibration," IEEE Transactions On Microwave Theory and Techniques, Vol. 39, No. 7, 1991, pp. 1205-1215.

[58] Program MultiCal, De-embedding Software, National Institute of Standards and Technology.

Chapter 4

[59] "Electrophoretic Deposition Process," US Patent 4592816, June 3, 1986.

[60] Partho Sarkar and Patrick S. Nicholson, "Electrophoretic Deposition (EPD): Mechanisms, Kinetics, and Application to Ceramics," J. Am. Ceram. Soc., Vol. 79 (8) pp. 1987-2002 (1996).

[61] D.A. Vidusek, "Electrophoretic Photoresist Technology: An Image of the Future – Today," Circuit World, Vol. 15 (2) pp. 6-10 (1989).

[62] David Merricks, "Control Of Negative Working Electrodepositable (ED) Photoresist Baths," The Journal (A Shipley Co. publication) pp. 10-15 (Winter 1995).

[63] *Microvias For Low Cost, High Density Interconnects*, John H. Lau and S.W. Rickey Lee, McGraw-Hill, New York, 2001.

[64] Steve Gold, "Looking at a Japanese Start-Up: A-Net," www.circuitree.com, Sept 2000.

[65] PEPR 2400 Brochure, Shipley Company, Inc.

[66] Omni Circuits PEPR 2400 Process Manual (rev. 1)

[67] P. Kersten, S. Bouwstra and J.W. Peterson, "Photolithography on Micromachined 3D Surfaces Using Electrodeposited Photoresists," Sensors and Actuators A 51 pp. 51-54 (1995).

[68] S. Linder et al.. "Photolithography In Anisotropically Etched Grooves," IEEE Proceedings of the 9th International Workshop on Micro Electro Mechanical Systems, An Investigation of Micro Structures, Sensors, Actuators, Machines and Systems, pp. 38-43 (1996).

[69] S. Linder, Personal Communication

[70] Frank T. Hartley et al., "X-ray Exposures of Electro-Deposited Photoresist for Conformal Lithography On Corrugated Surfaces," SPIE Vol. 3331 pp. 555-558 (1998).

[71] Jill Steeper, Shipley Printed Circuit Products, Private Communication.

[72] Matthias Heschel and Siebe Bouwstra, "Conformal Coating By Photoresist Of Sharp Corners Of Anisotropically Etched Through-Holes in Silicon," Sensors and Actuators A 70 pp. 75-80 (1998).

[73] *ULSI Technology*, Chapter 6: Lithography, C.Y. Chang and S.M. Sze editors, McGraw-Hill, New York, 1996.

[74] Yao Cheng et al., "Wall Profile of Thick Photoresist Generated via Contact Printing," IEEE Journal of Microelectromechanical Systems, Vol. 8, No. 1, March 1999, pp. 18- 26.

Chapter 5

[75] Nirod K. Das and Henry L. Bertoni editors, *Directions fot the Next Generation of MMIC Devices and Systems*, Plenum Press, New York (1997).

[76] Kurt E. Peterson, "Silicon as a Mechanical Material," Proc. Of the IEEE, Vol. 70 (5), pp. 420-457 (1982).

[77] Michael Pecht, editor, *Handbook of Electronic Package Design*, Marcel Dekker, Inc. New York (1991).

[78] Nadim Malif, *An Introduction to Microelectromechanical Systems Engineering*, Artech House. 2000.

[79] K.J. Herrick et al.,"Micromachined Technology in the Development of Three-Dimensional Circuits," IEEE Trans. Microwave Theory Tech., Vol. 46 (11), pp. 1832-1844 (1998).

[80] Alexandros Margomenos, Dimitrios Peroulis, James P. Becker, and Linda P.B. Katehi, "Silicon Micromachined Interconnects for On-wafer Packaging of MEMS Devices," Silicon Monolithic Integrated Circuits in RF Systems, Conference Digest, Ann Arbor, MI (2001).

Chapter 6

[81] Jamal S. Izadian and Shahin M. Izadian, *Microwave Transition Design*, Artech House, Norwood MA, 1988.

[82] Bassem A. Shenouda, L. Wilson Peasron and James E. Harris, "Etched-Silicon Micromachined W-Band Waveguides and Horn Antennas," IEEE Trans. Microwave Theory Tech., Vol. 49 (4), pp. 724-727 (2001).

[83] T. Weller, Micromachined High Frequency Transmission Lines on Thin Dielectric Membranes, PhD thesis, University Of Michigan, Ann Arbor, MI, 1995.

[84] S. Robertson, Micromachined W-Band Circuits, PhD thesis, University of Michigan, Ann Arbor, MI, 1997.

Chapter 7

[85] E. Tentzeris et al., "FDTD Characterization of Waveguide Probe Structures," IEEE Transactions On Microwave Theory and Techniques, Vol. 446, pp. 1452-1460 (1998).

[86] George E. Ponchak and Rainee N. Simons, "A New Rectangular Waveguide to Coplanar Waveguide Transition, "IEEE MTT-S Digest, pp. 491-492 (1990).

[87] Roger F. Harrington, *Time-Harmonica Electromagnetic Fields*, McGraw-Hill, Inc., New York, 1961.

[88] S.A. Schelkunoff, *Electromagnetic Waves*, D. Van Nostrand Company, Inc. New York (1943).

[89] James P. Becker, Yongshik Lee, Jack R. East and Linda P.B. Katehi, "A Fully Packaged Finite-Ground Coplanar Line-To-Micromachined Waveguide Transition," IEEE 9th Topical Meeting on Electrical Performance of Electronic Packaging (Cat. No.# 00TH8524), pp. 273-276.

[90] James P. Becker and Linda P.B. Katehi, "Toward a Novel Planar Circuit Compatible Silicon Micromachined Waveguide," in Proc. IEEE 8th Topical Meeting on Electrical Performance of Electronic Packaging, Oct.1999, IEEE # 99TH8412, pp. 221-224.

[91] Victor M. Lubecke, Koji Mizuno and Gabriel Rebeiz, "Micromachining For Terahertz Applications," IEEE Transactions on Microwave Theory and techniques, Vol. 46, No. 11, November 1998, pp.1821-1831.

[92] K. Hui et al., "A Micromachined 585 GHz Schottky Mixer," IEEE Microwave and Guided Wave Letters, Vol. 10, No. 9, September 2000, pp. 374-376.

Appendix E

[93] Nathan Marcuvitz, *Waveguide Handbook*, P. Peregrinus on behalf of the IEEE, 1986.